SHOCK EXCITED 1720 MHz MASERS

by

Aletha de Witt

submitted in fulfillment of the requirements
for the degree of

MASTER OF SCIENCE

in the subject

ASTRONOMY

at the

UNIVERSITY OF SOUTH AFRICA

SUPERVISOR: PROF D P SMITS

December 2005

I declare that ***Shock Excited 1720 MHz Masers*** *is my own work and that all the sources that I have used or quoted have been indicated and acknowledged by means of complete references.*

Signed:

Date:

Acknowledgements

I am indebted to my supervisor Prof D. P. Smits for the guidance and encouragement he gave me during the course of this study and the preparation of this thesis.

Thanks are also due to the National Astrophysics and Space Science Programme (NASSP) for granting me the opportunity to do this study.

It is also a pleasure for me express thanks to my husband Alex, our daughters, Andri and Joey for their support and inspiration during the course of this study.

Finally my deepest appreciation to my Lord who gave me the courage and will to complete this study.

This study is dedicated to my parents in law, Arina and Alex

Summary

1720 MHz OH masers have been detected towards a number of supernova remnants (SNRs) at the shock interface where the SNR slams into the interstellar medium. Models indicate that these masers are shock excited and can only be produced under tight constraints of the physical conditions. In particular, the masers can only form behind a C-type shock. Jets from newly-formed stars plow into the surrounding gas, creating nebulous regions known as Herbig Haro (HH) objects. Signatures of C-type shocks have been found in many HH objects. If conditions behind the shock fronts of HH objects are able to support 1720 MHz OH masers they would be a usefull diagnostic tool for star formation. A survey toward HH objects detected a number of 1720 MHz OH lines in emission, but future observations with arrays are required to confirm the presence of masers.

KEYWORDS: clouds — Herbig Haro objects — jets and outflows — masers — mass loss — molecules — pre-main sequence — shock waves — star formation — supernova remnants

Contents

List of Figures

List of Tables

Abbreviations and Acronyms

AIPS	Astronomical Information Processing System
ALMA	Atacama Large Millimeter Array
AU	Astronomical Unit
CLASS	Continuum and Line Analysis Suite of Software
CND	circumnuclear disk
DEC	declination
FIR	far-IR
FUOr	FU Orionis
FUV	far-UV
GBT	Greenbank Telescope
HH	Herbig Haro
HST	Hubble Space Telescope
IR	infrared
ISM	interstellar medium
KAT	Karoo Array Telescope
K-H	Kelvin-Helmholtz

LMC	Large Magellanic Cloud
LSR	local standard of rest
mas	milli-arcsecond
MERLIN	Multi-Element Radio-Linked Interferometer
mG	milliGauss
MM	mixed morphology
NIR	near-IR
NRAO	National Radio Astronomy Observatory
RA	right ascension
SALT	South African Large Telescope
S/N	signal to noise
SNR	supernova remnant
UV	ultraviolet
VLA	Very Large Array
VLBI	Very Long Baseline Interferometer

Chapter 1

Introduction

The earliest stages in the evolution of stars are not yet well understood, mainly because the process of star formation occurs deeply embedded within dusty molecular clouds that obscure optical and sometimes even infrared (IR) observations. Star formation is accompanied by accretion via circumstellar disks and envelopes, as well as the ejection of mass via outflows. Where the overlying extinction is low enough to permit optical observations, bow shaped structures called Herbig Haro (HH) objects have been observed in the vicinity of these young stars (protostars), sometimes as isolated entities and sometimes as a collimated chain of knots called HH jets. The emission line properties of these HH objects imply that the gas is excited by shock waves (Schwartz 1975, 1978). Therefore, HH objects are either the locations of impact between protostellar outflows and their surrounding environments or internal shocks within collimated outflows where faster material ejected by the protostar catches up with slower moving material ejected earlier. HH objects are the visible manifestations of protostellar outflows and these shocks

transfer momentum and energy into the surrounding medium. HH objects are typically found near low-mass, low-luminosity sources and show a bewildering variety in morphology, excitation conditions and velocity fields. Since the discovery of atomic emission lines at optical wavelengths in HH objects (Herbig 1950, 1951) they have been observed at different wavelengths, in particular in the IR (Beckwith et al. 1978). It is believed that the molecular outflows consists of ambient gas that has been entrained by the highly collimated HH jets (Rodríguez 1989). Both these HH flows and the molecular flows are indicators of embedded young stars. However, the mechanisms responsible for the ejection and collimation of the HH jets and the interaction between these jets and the molecular components are not yet well understood.

The study of HH flows provide for the analysis of shock structures, hydrodynamics in collimated outflows and of their interaction with the surrounding medium. The shock physics can reveal important information about the outflow physics and history. Protostellar outflows form an integral part of the star formation process and the study and analysis of these outflows provide important, but indirect insights into the nature of the accretion and mass loss processes that control the formation of stars. The modelling of HH objects has not always been successful in interpreting the observed emission line ratios and more efforts will have to be made to reproduce the kinematical properties, line ratios and morphologies for different HH objects. However, modelling of those HH objects that show bow shaped spatial structure have been successful in explaining many of the observed features. It has been shown for many of these HH objects that the shock formed by this interaction is a J-type, but on the wings of the bow shock conditions exist that show signatures of C-type shocks.

HH objects are not the only examples in the Universe of where C-type shocks occur. Lockett, Gauthier & Elitzur (1999) suggested that shock-excited 1720 MHz OH masers could be used to identify the presence of C-type shocks formed at the interface between the blast wave of an expanding supernova remnant (SNR) and the surrounding medium. 1720 MHz OH masers have been found in about 10 % of the sample of SNRs searched. These OH lines are distinguished from their ionized hydrogen (H II) region counterparts in having emission only at 1720 MHz and wider line widths. Modelling of the 1720 MHz OH masers indicates that they can only form in a restricted set of conditions: the masers require a gas density of $n \sim 10^5$ cm^{-3}, OH column densities of $N_{OH} \sim 10^{16} - 10^{17}$cm^{-2} and a gas temperature of $T = 50 - 125$ K (Lockett et al. 1999). These masers can only be produced in the gas behind a C-type shock (Lockett et al. 1999) irradiated by the X-ray flux from the SNR interior (Wardle 1999). Observational studies of these masers and the regions surrounding them have revealed a number of characteristic properties and show that the current model predictions are in good agreement with the observational results.

No systematic blind searches of the Galaxy for 1720 OH masers have been done so far and many sources could be undetected. The shocks in HH objects have a wide range of physical conditions, and hence it is possible that some of these objects could support shock-excited 1720 MHz OH masers. The detection of 1720 MHz OH masers toward HH objects will allow for measurements of the kinematical distance and systemic velocity of the masing gas and will show the exact location of the on-going shock. Proper motions measurements of the masers could be used to map the motion of the surrounding gas and the masers would allow for a measurement of the strength of the magnetic field through Zeeman splitting. Modelling of these masers in SNRs

have shown that they form under tight constraints and give information of the physical conditions of both the shocked and the unshocked gas as well as the properties of the shock. A determination of the properties of HH objects will help to constrain the dynamics and physics of both the outflows and the star forming environments. By comparing the models and the observations of the regions surrounding these masers in HH objects and SNRs may lead to new insights in both fields of research, may clear up some controversies that exists around the current models and may ultimately explain some of the observed discrepancy from the models in both research fields.

The aim of this study has been to determine whether conditions can exist behind the shocks of HH objects to support the production of 1720 MHz OH masers. A literature study has been done on both maser emitting SNRs and HH objects and found that the physical and spectroscopic properties of these regions often show remarkable similarities. Modelling shows that 1720 MHz OH masers can only be produced behind C-type shocks and models of many HH objects indicate the presence of C-type shocks. These similarities initiated a survey for 1720 MHz OH masers toward a sample of HH objects using single dish radio telescopes. The survey detected emission lines toward a number of HH objects with line withs comparable to those observed in SNRs. However, to confirm that these are masers, their small spot size will need to be resolved with arrays.

This dissertation is laid out as follows.
Chapter 2 provides an overview of maser physics as well as the quantum mechanics of the OH molecule and the energy levels that result from its structure.

Chapter 3 is a literature review of the discovery and modelling of 1720 MHz

OH masers toward SNRs. Models show that 1720 MHz OH masers are produced in the molecular gas behind the shock front of a SNR-molecular cloud interaction where the masers are collisionally pumped. The masers can only form under tight constraints of the physical conditions.

Chapter 4 reviews the literature of the observational properties of the 1720 MHz OH masers in SNRs and the regions surrounding them. These observations are in general agreement with those predicted by models, although, as discussed, some discrepancies from the models are observed.

Chapter 5 provides a review of the general properties of HH flows, observations done towards these regions at various wavelengths as well as an overview of the modelling of the shocks. When compared to the maser emitting SNRs, many HH objects show similar spectra and models indicate the existence of C-type shocks.

In Chapter 6 the details of an observing campaign towards HH objects is discussed.

Chapter 7 gives a conclusion and future work is discussed.

Chapter 2

Maser Theory and OH Ground State Masers

2.1 Maser Theory

The word maser is an acronym for "**M**icrowave **A**mplification by **S**timulated **E**mission of **R**adiation". Maser action describes a mechanism (stimulated emission) by which centimetric radiation (microwave) is amplified. The maser was the principle precursor of the laser which amplifies radiation at visible wavelengths. The first maser was built in 1951 by Charles Townes and papers about masers were published in 1954 as a result of investigations carried out simultaneously and independently by Charles Townes and co-workers at Columbia University in New York and by Drs. Basov and Prochorof at the Lebedev Institute in Moscow. All three received the Nobel Prize in 1964 for their contributions to physics.

Masers in astronomical environments occur naturally and are usually associated with rotational transitions in molecules. The first interstellar molecule to be detected at radio frequencies was OH (Weinreib et al. 1963), and it was also the first to be detected as a maser in space (Weaver et al. 1965). Since their discovery these emissions have provided useful diagnostic information about the molecular gas where they occur, and have become very important astronomical tools in the exploration of the Universe. This thesis focuses on OH masers that occur in warm molecular gas behind cosmic shocks.

2.1.1 Einstein's Coefficients and Stimulated Emission

The relationship between emission and absorption of radiation by matter was first discovered by Einstein. Einstein considered the simple case in which radiation interacts with an atomic system with two energy levels E_2 and E_1, where $E_2 > E_1$. E_2 is the excited state with N_2 the number of atoms in the excited state, and E_1 is the ground state with N_1 the number of atoms in the ground state, as illustrated in Figure 2.1 (a). Einstein identified three processes by which radiation interacts with matter:

Spontaneous Emission An atom in the excited state (E_2) can spontaneously decay to the ground state (E_1), without the presence of any radiation field, and will emit a photon of energy equal to the energy difference between the two levels ($\Delta E = E_2 - E_1 = h\nu_0$) as illustrated in Figure 2.1 (b). Atoms in the excited state will decay at a rate proportional to the number of atoms in the excited state (N_2). The photon will be emitted in a random direction and there will be no phase relationship between photons emitted from a group of excited

atoms. In other words, radiation produced by spontaneous emission does not propagate in the same direction. In the absence of other processes, the number of atoms in the excited state at time t, is given by $N_2(t) = N_2(0)\exp(-t/\tau_{21})$, where $N_2(0)$ is the number of excited atoms at time $t = 0$, and τ_{21} is the lifetime of the transition between the two states. The Einstein A-coefficient is defined by $A_{21} = 1/\tau_{21}$, which is the transition probability per unit time for spontaneous emission.

Absorption This occurs in the presence of photons passing through a group of atoms, where the quantum energy of the photons, $h\nu_0$, matches the energy gap between the ground state (E_1) and the excited state (E_2) of the atoms. There is a possibility of these photons being absorbed by atoms which are in the ground-state (E_1), causing them to make a transition to the excited state (E_2) as illustrated in Figure 2.1 (c). The probability of a photon being absorbed is proportional to the intensity of the radiation at frequency ν_0, and also to the number of atoms in the ground state N_1. The Einstein B-coefficient is defined as the proportionality constant, B_{12}, where $N_1 B_{12}\bar{J}$ is the transition probability per unit time for absorption, and $\bar{J}$ is the mean intensity.

Stimulated Emission Einstein found that another process that was proportional to $\bar{J}$ and caused emission of a photon was necessary to derive Planck's law. If an atom is in an excited state (E_2), then a photon with energy $h\nu_0 = E_2 - E_1$, can stimulate a transition to the ground state, producing a second photon of energy $h\nu_0$. The original photon is not absorbed by the atom, and the result is the emission of two photons of the same frequency propagating in the same direction (see Figure 2.1 (d)). The rate at which stimulated emission occurs is proportional

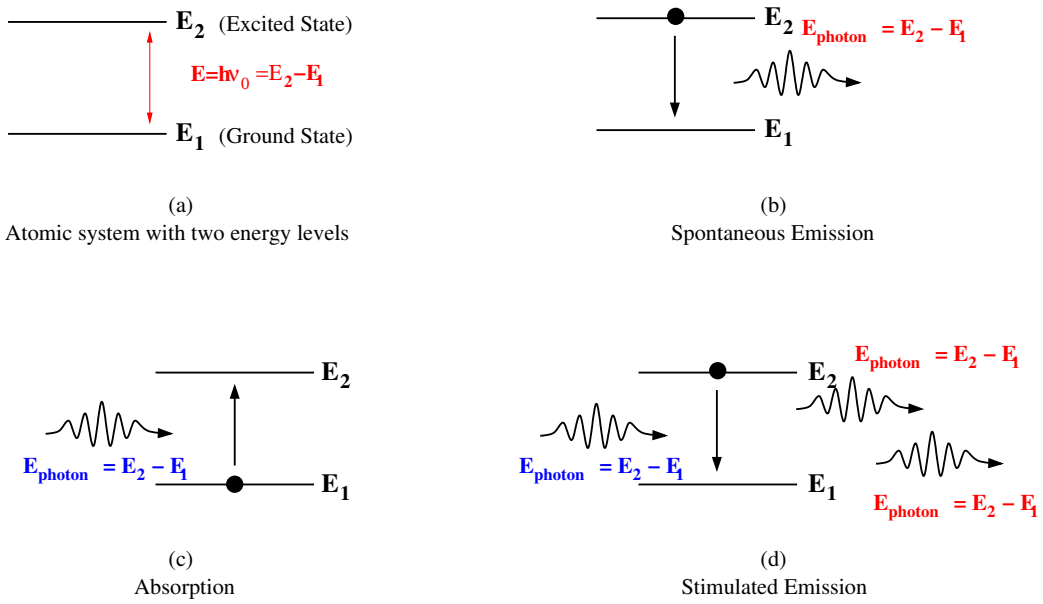

Figure 2.1: The interaction of radiation with an atomic system.

to the number of atoms N_2 in the excited state, and the intensity of the radiation at frequency ν_0. The critical detail of stimulated emission is that the induced photon has the same frequency and direction of propagation as the inducing photon. B_{21} is a Einstein B-coefficient, where $N_2 B_{21} \bar{J}$ is the transition probability per unit time for stimulated emission.

Einstein showed that the relations between the A- and B-coefficients are given by:

$$g_1 B_{12} = g_2 B_{21} \tag{2.1}$$

$$A_{21} = \frac{2h\nu^3}{c^2} B_{21} \ , \tag{2.2}$$

where g_1 and g_2 are statistical weights of level 1 and level 2 of an atomic system. Eq. 2.1 and 2.2 connect the atomic properties A_{21}, B_{21} and B_{12} and have no dependence on temperature T.

Stimulated emission is proportional to the intensity of the radiation and only affects the photons along the given beam, similar to the process of absorption. Therefore, stimulated emission is treated as a negative absorption, and its effect is included through the absorption coefficient. The emission coefficient j_ν and the absorption coefficient corrected for stimulated emission α_ν are given by the following relations in terms of the Einstein A- and B-coefficients:

$$\begin{aligned} j_\nu &= \frac{h\nu_0}{4\pi} N_2 A_{21} \phi(\nu) \\ \alpha_\nu &= \frac{h\nu_0}{4\pi} \phi(\nu)(N_1 B_{12} - N_2 B_{21}) \ . \end{aligned}$$

$\phi(\nu)$ is the line profile function, which for simplicity has been taken to be equal for absorption and emission. The line profile function describes the relative effectiveness of frequencies in the neighborhood of ν_0 for causing transitions. In operational terms, stimulated emission and absorption always occur together and cannot be disentangled. If we consider all of the atoms being in the excited state, a photon at frequency ν_0 stimulates emission from an atom in the excited state, so that there are now two photons of wavelength ν_0. These photons stimulate emission from the next two atoms which are also in the excited state, resulting in four photons at frequency ν_0. This process continues and results in the amplification of radiation at frequency ν_0.

2.1.2 Population Inversion

For a system in thermodynamic equilibrium the populations N_i of the levels obey the Boltzmann distribution:

$$\frac{N_j g_i}{N_i g_j} = \exp\left(\frac{-(E_j - E_i)}{kT}\right) \ .$$

In most gases strict thermodynamic equilibrium does not occur.

Because $E_j > E_i$, it follows from the Boltzmann distribution that

$$\frac{N_j g_i}{N_i g_j} = \exp\left(\frac{-h\nu}{kT}\right) < 1 \ ,$$

so that

$$\frac{N_i}{g_i} > \frac{N_j}{g_j} \ .$$

This is the normal state of the system and we say that these are normal populations. Even when material is out of thermal equilibrium, this relation is usually satisfied. The conditions in space are in many cases far from any type of equilibrium. Regions of gas are often in the process of being heated, cooled, expanded or compressed, and are subject to chemical reactions and non-uniform radiation fields. This results in the level populations deviating from the Boltzmann distribution. It is possible to put enough atoms in the upper state so that

$$\frac{N_i}{g_i} < \frac{N_j}{g_j} \ .$$

In this case the higher energy level E_j is overpopulated relative to the lower energy level E_i; this condition is called a population inversion. To produce a population inversion it is clear that the system cannot be in thermodynamic equilibrium.

2.1.3 Maser Emission

The interaction of radiation with matter (absorption, spontaneous emission and stimulated emission), as described in the previous section are all active during the operation of a maser. Atoms or molecules that absorb radiation will end up in the excited state. Decays via the process of spontaneous emission will release photons in any random direction. These photons can either be re-absorbed or can cause stimulated emission, releasing another photon propagating in the same direction. When more stimulated emissions than absorptions occur between two levels, there is a nett increase in the number of photons at a particular frequency. This amplification requires that the upper level be over-populated relative to the lower level. In other words, a population inversion is required and needs to be maintained for a maser to operate. When this occurs, photons originating from spontaneous emission or from background sources will be amplified by stimulated emission and this can lead to the production of an intense, tightly collimated beam of photons at the frequency of the transition. This amplification of radiation is limited only by the rate at which the inversion can be maintained by the processes responsible for the supply of molecules in the upper state.

In astronomical environments the population inversion of molecules can be achieved under natural conditions, creating compact spectral line sources that are observable at radio wavelengths. The process by which a population inversion is achieved and maintained is called pumping. The three main methods of pumping are by radiative processes, collisional processes, and chemical processes, or by combinations of these processes (Wright 2001). The relevance of each process may depend on the environment; in particular, the density and ambient radiation flux, cloud geometry and internal cloud

velocity fields are very important in the formation of masers. Purely radiative processes can lead to population inversions if radiative rates are high compared to collisional rates (e.g. when molecular densities are low), and if transitions have widely varying optical thicknesses. Collisional processes can lead to population inversions if different transitions have different cross-sections. In regions of high density, collisions will tend to quench population inversions by re-thermalizing the populations. Chemical and photochemical processes can produce population inversions by creating molecules in an excited state from which radiative decay is slow (metastable state), and collisional de-excitation is slow because of low densities.

It is clear that one of the characteristics of masers is the requirement for a mechanism to pump and maintain the gas in a state of inverted populations. Masers also require a long pathlength of velocity coherent gas to exist. It can be shown that the maser process can lead to exponential growth along the length of the cloud. Exponential growth cannot continue indefinitely. Because the masing action reduces the population of molecules in the excited state, when the radiation intensity becomes large, it affects the population inversion. When this occurs, the maser is said to be saturated. Masers can only grow linearly in a saturated region. Astronomical masers can achieve brightness temperatures of $T_B \sim 10^{10}-10^{15}$ K, where $kT_B = \frac{1}{2}\frac{c}{\nu}^2 I_\nu$. Although the brightness temperature gives a useful comparison between masers, maser emission is non-thermal, and therefore maser brightness is in no way an indication of the physical temperature of the environment in which the maser is occurring.

2.1.4 Masers as Astronomical Tools

Molecules that produce strong masers are OH, H_2O, SiO and CH_3OH; weak masers from NH_3, H_2CO and HCN have been observed. Masers are likely to be found wherever warm molecular gas exists in space. They have been detected in diverse places such as star forming regions, envelopes of evolved stars, SNRs, protoplanetary nebulae, comets and as megamasers in the cores of active galactic nuclei. Masers are extremely useful probes for us in our exploration of the Universe and have become a very important astronomical tool, especially as they tend to exist in those regions of the Universe that are hidden from us in the optical radiation range.

The observed line widths of astronomical masers are typically $\Delta v \sim 0.2$ km s^{-1}, which means that the radial velocity of the masing gas can be measured to great accuracy. Doppler shifts of maser lines can be used to determine kinematic distances to the objects in which they occur. In this way they have been used to estimate the distance to the center of the Galaxy (Reid & Moran 1988). They can also be used to trace the bulk movement of gas clouds (Habing et al. 1983). Because of beaming due to unsaturated growth, astronomical masers can have sizes of a few hundred Astronomical Units (AU). These dimensions translate into spot sizes of milli-arcseconds (mas) and hence are unresolved on the longest interferometer baselines. The positions of maser spots can be determined accurately using Very Long Baseline Interferometer (VLBI) techniques. By measuring the positions at different epochs, their proper motions can be determined, and this allows one to map the motion of expanding shells of gas around Mira-type variables (Humphreys 1999) and the expansion of star-forming regions such as W3(OH) (Braun & Strom 1986a; Wright 2001).

Zeemann splitting of ground-state OH masers occur in magnetic fields of milliGauss (mG) strengths and can be used to measure the magnetic fields in otherwise unobservable regions. The Galactic magnetic field has been mapped (Reid & Siverstein 1990) and the magnetic energy density of magnetic fields in star-forming regions has been found to be comparable to the kinetic energy density.

By modelling masers, limits can be set on the physical conditions of the environment in which they occur. Specifically ground-state 1720 MHz OH masers formed at the shock interface between SNRs and molecular clouds in the interstellar medium (ISM) have tight constraints on the physical conditions. It is this characteristic that most of this thesis will deal with: the emission of masers from shock excited gas behind a SNR-molecular cloud interaction and possibly also in HH objects, which is the shock front where high velocity jets from low-mass protostars interact with the ISM.

2.2 The OH Molecule and its Energy Levels

2.2.1 Angular Momentum in Molecules

Molecules have much more complexity than single atoms. Since the electrons in a molecule move very much faster than the nuclei, a good approximation is that the nuclei can be assumed stationary whilst the electronic motions are considered. This is called the Born-Oppenheimer Approximation. In a molecule the complete rotational symmetry about the nucleus, as in atoms, is lost and apart from having electronic energies with discrete levels similar to those in atoms, they can also possess rotational energy (bod-

ily motion about a center of mass) and vibrational energy (due to periodic displacement of nuclei from their equilibrium positions). The electronic, rotational and vibrational energy levels of molecules are also quantized, and in the Born-Oppenheimer Approximation the combined rotational, vibrational and electronic energy is taken as the sum of the individual energies, i.e. $E_{total} = E_{rot} + E_{vib} + E_{elec}$.

Electrons in a molecule have both orbital and spin angular momentum, but when electrons are paired, both of these quantities cancel out. The OH molecule has one unpaired electron, so that the total orbital angular momentum, **L**, and the total spin angular momentum **S** of the valence electron are both non-zero. In contrast to an atom, a diatomic molecule like OH has an internally defined direction in the form of the molecular (or internuclear) axis. In an atom the force on the electron is central and the angular momentum is conserved. However, electrons posses orbital angular momentum **L**, and spin angular momentum **S**. The projections of the angular momenta **L** and **S**, onto the internuclear axis are constant and well defined (quantized). The quantum number describing this projection, m_l corresponds to the direction of the precession, and for symmetric reasons this does not make any difference in a diatomic molecule. A molecular orbital is designated by the value of λ, and the atomic orbital used to construct it, where $\lambda = |m_l|$. In a molecule the quantum numbers λ of the molecular orbitals are added to form a resultant quantum number Λ. States with $\Lambda = 0, 1, 2, \ldots$ are designated by $\Sigma, \Pi, \Delta, \ldots$. The magnetic moment of the orbital motion (which is aligned with the nuclear axis) and of spin ($S = \frac{1}{2}$), with projection onto the nuclear axis Σ of the electron interact and cause the spin of the electron to be orientated so that the magnetic moment of the spin is also aligned along the internuclear axis. This is called spin-orbit coupling.

There are four sources of angular momentum in a diatomic molecule: the spin of the electrons, **S**, their orbital angular momenta, **L**, the rotation of the nuclei about their center of mass, **N** and the nuclear spin, **I**. In general, a diatomic molecule will have a component of electronic orbital angular momentum about the internuclear axis equal to $\Lambda\hbar$, where Λ is an integer. $\Lambda = |m_l|$, and electronic spin angular momentum $\Sigma\hbar$ where Σ is an integer or half integer. The angular momentum of the complete molecule is the resultant of all these components, combined according to the rules of quantum mechanics.

2.2.2 Hund's Case for OH

For OH the coupling is done in terms of Hund's case (a), where the magnetic field generated by the molecular rotation is not large, and **L** and **S** are both coupled to the molecular axis in the presence of rotation. The total orbital angular momentum of the nuclei and electrons can take any of the values $(\Lambda + N)\hbar$, where $\Lambda = 1$ is the electronic ground state and $N = 0, 1, 2, \ldots$ is the rotational quantum number. As mentioned before, the one unpaired electron sitting in a 2p orbital in the oxygen atom ensures that the electronic angular momentum in the OH molecule is not zero, and thus the ground-state of OH, $\Lambda = 1$, is a Π state. The total angular momentum, orbital plus spin, is $J\hbar$, where J can take the values $\Lambda + N \pm \Sigma$. The single unpaired electron in OH has $\Sigma = \frac{1}{2}$, and hence two sequences are formed, depending on whether the positive or negative sign is taken. In OH, the states with the positive sign for Σ have the lower energies. The rotational states of the lowest vibrational and electronic state are labeled $^2\Pi$, the superscript indicating that there are two sequences. The sequence is shown by the least value of J as a subscript,

usually with the actual value of J added, e.g.

$$^2\Pi_{3/2}\ J = 3/2 \quad \text{or} \quad ^2\Pi_{3/2}\ J = 5/2\ .$$

Both the Born-Oppenheimer approximation, which allows us to separate the electronic, vibration and rotation components of the molecule, and the Hund's case (a) coupling, which specifies how the angular momentum components are added together, are only correct to a certain order. In a more careful quantum mechanical treatment of OH, there is a term that depends on the sign of L_x and L_y (L_z is the projection of $\mathbf{L}$ on the internuclear axis associated with Λ). This effect is known as lambda doubling, and leads to a separation of each J level into two components, the effect being larger for faster rotation. Each state in the ladder is now a doublet, approximately symmetric about the unperturbed level. This is essentially a result of violation of the Born-Oppenheimer Approximation, and the two levels of the lambda doublet are actually different electronic states. The two states of the lambda doublet are of opposite symmetry or parity. The parity of the levels is indicated in Figure 2.2 by the + and − signs.

2.2.3 The Hyperfine Interaction in OH

The hydrogen nucleus (a proton) has non-zero spin angular momentum $\mathbf{I}$, and to obtain the total molecular angular momentum this has to be taken into account. The total molecular angular momentum is labelled by the quantum number $\mathbf{F}$, which is the vector sum of $\mathbf{J}$ and the spin quantum number, $\mathbf{I}$, of the proton, i.e.

$$\mathbf{F} = \mathbf{J} \pm \mathbf{I}\ ,$$

State	Energy above ground state cm^{-1}	Transition in quartet ($F_{initial} \rightarrow F_{final}$	Frequency of transition MHz	Equilibrium relative line strength
$^2\Pi_{3/2}$ $J = 3/2$	0	$2 \rightarrow 1$	1612	1
		$1 \rightarrow 1$	1665	5
		$2 \rightarrow 2$	1667	9
		$1 \rightarrow 2$	1720	1
$^2\Pi_{3/2}$ $J = 5/2$	84	$3 \rightarrow 2$	6017	1
		$2 \rightarrow 2$	6031	14
		$3 \rightarrow 3$	6035	20
		$2 \rightarrow 3$	6049	1
$^2\Pi_{1/2}$ $J = 1/2$	126	$1 \rightarrow 0$	4660	1
		$1 \rightarrow 1$	4751	2
		$0 \rightarrow 0$	Forbidden	Forbidden
		$0 \rightarrow 1$	4766	1
$^2\Pi_{1/2}$ $J = 3/2$	188	$2 \rightarrow 1$	7749	1
		$1 \rightarrow 1$	7761	5
		$2 \rightarrow 2$	7820	9
		$1 \rightarrow 2$	7832	1
$^2\Pi_{3/2}$ $J = 7/2$	202	$4 \rightarrow 3$	13434	1
		$3 \rightarrow 3$	13435	27
		$4 \rightarrow 4$	13441	35
		$3 \rightarrow 4$	23442	1

Table 2.1: Details of the lower rotational transitions of OH (From: Wright (2001))

where $\mathbf{I} = \frac{1}{2}$, and each level of the lambda doublet is split into two levels, of values $J + \frac{1}{2}$ and $J - \frac{1}{2}$. The interaction between the spins of the valence electron and proton is known as the hyperfine interaction. Because of lambda doubling and the hyperfine interaction, each **J** state is split into four levels, with the difference in energy of the hyperfine states in the ground-state equivalent to radiation of 53 MHz. The full set of energy levels of the OH molecule in the electronic and vibrational ground-state is shown in Figure 2.2, and the details of the lower rotational levels of OH in Table 2.1.

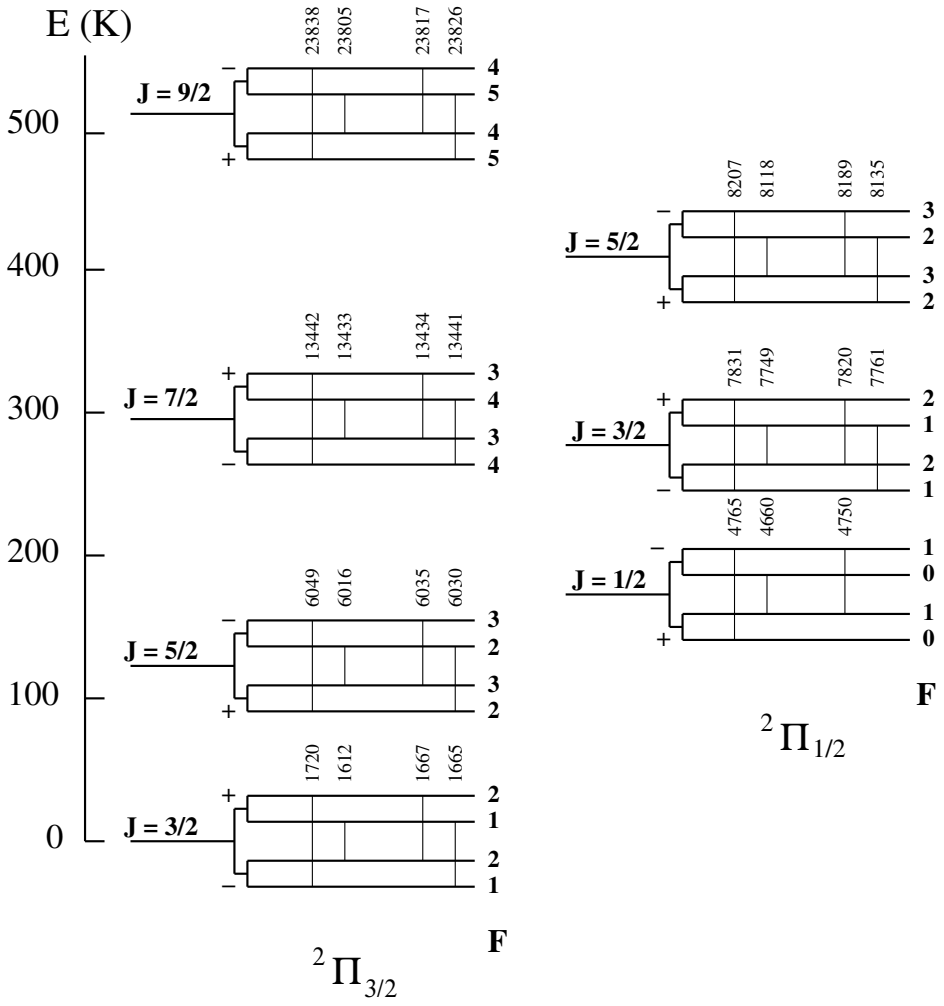

Figure 2.2: The lowest rotational energy levels of OH. Lambda doubling, hyperfine splitting and the allowed transitions in each rotational level are indicated. The numbers written vertically are the frequencies in MHz of the transitions indicated beneath each number.

2.2.4 Magnetic Fields and the Zeeman Effect

Molecules with unpaired electrons and hence non-zero electronic momentum (such as OH) have paramagnetic properties. In a magnetic field B of the order of a few mG, the energy of a level with total quantum number F

becomes

$$E_F = E_0 + B\mu_B g_F m_F \ ,$$

where E_0 is the energy in zero field, and $\mu_B = e\hbar/2mc$ is the Bohr magneton. Each molecular level F contains $2F+1$ magnetic sub-states, labeled m_F. In the absence of a magnetic field all of these sub-levels are degenerate, but an external magnetic field lifts the degeneracy. The factor g_F is the Landé Factor — a coefficient characteristic of the state, which can be calculated from the various quantum numbers that make up the total molecular angular momentum:

$$g_F = g_J \frac{F(F+1) + J(J+1) - I(I+1)}{2F(F+1)} \ .$$

The factor g_J has been measured by Radford (1961) for the $^2\Pi_{3/2}$ state of OH to be 0.935 for the upper levels of the lambda-doublet, and 0.936 for the lower levels. Transitions between the magnetic components in the presence of a magnetic field therefore produce a number of lines at similar frequencies known as Zeeman components (see Figure 2.3). The ground state of OH, which will be investigated in this work, has values of F of just 1 and 2. Linear polarization is produced by $\Delta m_F = 0$ transitions while right and left circular polarization by $\Delta m_F = +1$ and $\Delta m_F = -1$ transitions respectively.

2.2.5 Selection Rules in OH

The selection rules for electric dipole transitions are: $\Delta F = 0 \pm 1$ but $F = 0 \rightarrow F = 0$ is forbidden; $\Delta J = \pm 1$. The transitions for which $\Delta F = 0$ are called main-lines, while those with $\Delta F = \pm 1$ are called satellite lines. The ground-state main-lines have frequencies of 1665 and 1667 MHz, and the satellite-lines produce lines of 1612 and 1720 MHz. The energy splittings are

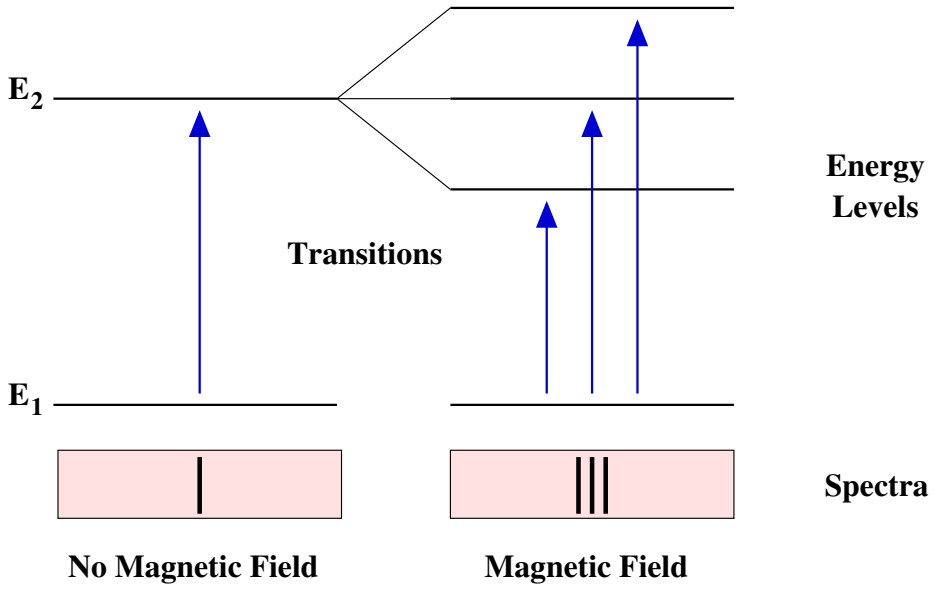

Figure 2.3: The Zeeman effect: In the presence of a magnetic field a single F level in the OH molecule splits into $2F + 1$ magnetic sub-levels.

such that the rotational transitions within a vibrational level occur in the far-IR (FIR) and mid-IR (MIR), while transitions within a rotational level are at microwave frequencies.

2.3 OH Ground-State Masers

Astronomical masers occur naturally and are observed in all four of the transitions within the ground rotational state (18cm transitions) of the OH molecule at 1612, 1665, 1667 and 1720 MHz. OH is unique amongst strong maser molecules because of the Zeeman effect of the hyperfine structure. 1612 MHz OH masers occur in circumstellar shells of evolved stars. Main line masers (1665, 1667 MHz) have been found in more than 250 star-forming regions. In about 10% of these sources 1612 and/or 1720 MHz masers have also

been discovered. Masers in star-forming regions are believed to be pumped by a FIR radiation field. OH masers are also present in protoplanetary nebulae and have been detected in comets. 1667 MHz and 1665 MHz masers are produced in IR luminous galaxies.

1720 MHz OH masers have been detected towards SNRs, and appear to occur in the warm molecular gas behind the shock front of an SNR-molecular cloud interaction where the masers are collisionally pumped. The 1720 MHz masers toward SNRs occur alone, with the other ground state transitions of the OH molecule in absorption. In the next chapter we look in more detail at the 1720 MHz OH masers associated with SNR-molecular cloud interactions.

Chapter 3

Discovery and Theory of OH Masers in SNRs

A supernova occurs when a massive star exhausts the nuclear fuel in its core and erupts in a violent explosion in which the hot gas expands into the ISM. A SNR is the remains of the outer layers of a star that has been blown into space by such an explosion, together with swept-up interstellar material. A shock front is formed at the interface between a SNR and the ISM that it is expanding into. 1720 MHz OH masers have been found in a selected number of SNRs and are believed to be associated with the shocked gas. The properties of these 1720 MHz OH masers differ from those found in H II regions. Modeling of these regions (Elitzur 1976; Lockett et al. 1999; Wardle 1999), has shown that 1720 MHz OH masers can be produced in the post-shocked gas, but are subject to tight constraints on the physical conditions. In particular, the masers can only form behind a C-type shock, and hence could be useful signposts of the presence of C-type shocks. This

chapter gives an overview of the theoretical work that has been done on these shock-excited 1720 MHz OH masers since their discovery in SNRs.

3.1 Discovery and Statistics

More than 30 years ago observations of OH ground-state lines toward the SNRs W28 and W44 (Goss 1968; Goss & Robinson 1968; Turner 1969; Robinson, Goss & Manchester 1970) showed 1720 MHz OH emission as narrow lines, detected simultaneously with broad line absorption features at 1612, 1665 and 1667 MHz (see Figure 3.1 for SNR W28). DeNoyer (1979a) observed similar lines toward the SNR IC 443. These OH lines are distinguished from their H II region counterparts in having emission only at 1720 MHz, relatively low degrees of linear and circular polarization, and line widths of about $1-2$ km s^{-1}. This difference in the emission and absorption patterns to that generally found in star-forming regions prompted Goss & Robinson (1968) to suggest that the OH is physically associated with the SNRs. Because the OH in IC 443 has a similar velocity signature and spatial distribution as the neutral hydrogen (H I) gas within the remnant, DeNoyer (1979a) suggested that the OH was part of the shocked cloud within the SNR rather than a chance coincidence along the line-of-sight.

These early observations of the OH ground state lines toward SNRs were of low angular resolution, and hence it was not possible to determine whether the emission was due to thermal or maser processes. However, interferometric observations made by Frail, Goss & Slysh (1994) with the Very Large Array (VLA) towards the SNR W28 showed 26 distinct spots of 1720 MHz OH emission lying along the edge of the radio continuum emission. The high

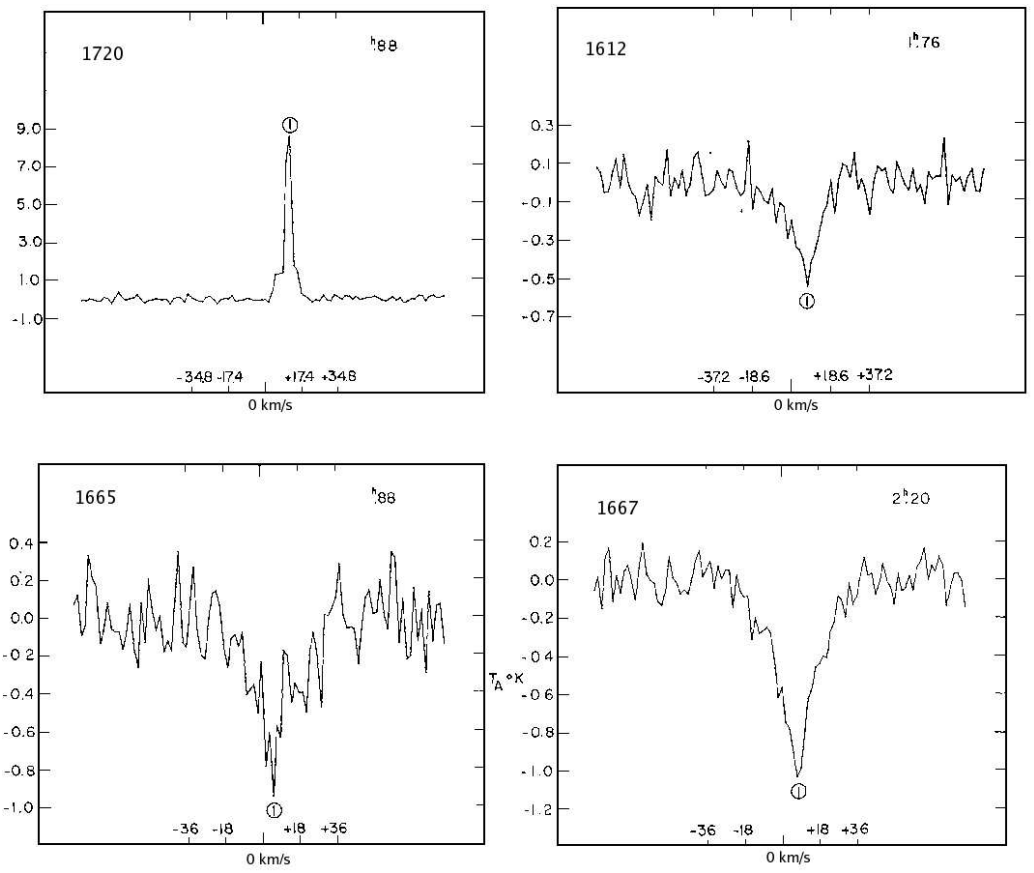

Figure 3.1: SNR W28 OH lines. Top panel: (*left*) 1720 MHz OH narrow line maser emission. (*right*) 1612 MHz OH broad line absorption. Bottom panel: (*left*) 1665 and (*right*) 1667 MHz OH broad line absorption. (From: Goss (1968))

brightness temperature of the spots identified them as masers. Frail et al. (1994) concluded that the location of the maser spots, together with the physical conditions in the SNR and the adjacent molecular cloud, argued for a shock excitation mechanism for the masers. This is consistent with a model for 1720 MHz OH masers developed by Elitzur (1976), who pointed out that these masers could occur in warm molecular gas without the need for a FIR field. In fact, calculations done by Elitzur (1976) showed that radiative pumping mechanisms cannot produce strong 1720 MHz inversions,

and that the only efficient pumping mechanism that can produce 1720 MHz line inversions, unaccompanied by other OH ground state emission, is by collisional excitation.

The discovery of 1720 MHz OH masers associated with the SNR W28 offered the tantalizing prospect of a powerful new diagnostic tool for probing the shock interaction of SNRs with molecular clouds. The results of Frail et al. (1994) initiated sensitive, high resolution studies of the SNRs W28, IC 443 and W44, as well as single dish surveys to search for 1720 MHz OH emission towards known Galactic SNRs (Frail et al. 1996; Green et al. 1997; Koralesky et al. 1998; Yusef-Zadeh et al. 1996; Yusef-Zadeh, Uchida & Roberts 1995; Yusef-Zadeh et al. 1999). To establish which sources had maser emission as opposed to thermal OH emission, the 1720 MHz detections from single dish surveys were investigated further using interferometers. The surveys discovered 1720 MHz OH masers in $\sim 10\%$ of the sample of Galactic SNRs searched (Green 2002). Brogan et al. (2004) carried out a search for masers towards four SNRs in the Large Magellanic Cloud (LMC), detecting two maser spots towards one of the objects. Table 3.1 summarizes the results of all the surveys published up to October 2005.

No. of Galactic SNRs searched	172 ($> 75\%$ of total known)
No. of maser sources found in Galactic SNRs	19 ($\sim 10\%$ of sample searched)
No. of LMC SNRs searched	4
No. of maser sources found towards LMC	1

Table 3.1: Statistics from SNR surveys

3.2 Theory and Modelling

The population of internal states of OH is determined by absorption, stimulated emission, spontaneous emission and excitation and de-excitation by collisions with H_2 molecules (the dominant component of the gas). At low temperatures most OH molecules will populate the four hyperfine levels of the ground-state. Excitation of the OH molecule to higher rotational levels, followed by radiative cascades back to the the ground-state levels will reshuffle the populations among the ground-state hyperfine levels. Elitzur (1976) showed that if the cascades back to the ground-state levels are optically thick, inversion of the satellite lines can occur. When radiative cascades occur from the $^2\Pi_{3/2}$ $J = 5/2$ levels back to the ground-state levels, the populations of the levels giving rise to the 1720 MHz line can be inverted. This occurs because the $F = 2$ levels of the ground-state are connected to both the $F = 2$ and $F = 3$ levels of $^2\Pi_{3/2}$ $J = 5/2$, whereas $F = 1$ levels connect only to $F = 2$ levels. When the cascades are from the $F = 0$ and $F = 1$ states of the $^2\Pi_{1/2}$ $J = 1/2$ levels back to the ground-state levels, the $F = 1$ levels of the ground-state will be overpopulated relative to the $F = 2$ levels, and the populations associated with the 1612 MHz line will be inverted. The 1612 MHz line will dominate whenever the inversions are *a priori* equally likely, since it is easier to overpopulate the sub-levels of an $F = 1$ level, where levels are divided among fewer states, than the sub-levels of an $F = 2$ level. Therefore, in order to invert the 1720 MHz transition it is necessary to excite the $^2\Pi_{3/2}$ $J = 5/2$ levels more than the $^2\Pi_{1/2}$ $J = 1/2$ levels. Because the $^2\Pi_{1/2}$ $J = 1/2$ levels lie at $T \sim 200$ K and the $^2\Pi_{3/2}$ $J = 5/2$ levels at $T = 120$ K (see Figure 2.2), a natural way to achieve this is by collisions at temperatures below 200 K.

The rate of collisional excitation and de-excitation is determined by both the temperature and density of the gas. The 1720 MHz inversion will only occur if the final cascades back to the ground-state are dominated by optically thick decays from the first rotationally excited state. The radiative decay rate depends on the OH column density. As the column density increases the radiative decay rates become smaller because of photon trapping, and the downward collisions begin to dominate. The OH column density should not be so high that decays from the $^2\Pi_{1/2}$ $J = 1/2$ levels become optically thick as the inversion will then switch to the 1612 MHz line. Therefore, the optical depth τ must be greater, but not very much greater than unity.

Using collision rates calculated by Offer, van Hemert & van Dishoeck (1994), Lockett et al. (1999) updated the calculations of the Elitzur (1976) model and performed a detailed study of the pumping requirements for 1720 MHz OH masers associated with SNRs. Detailed pumping calculations were also performed by Pavlakis & Kylafis (1996) using the Offer et al. (1994) rates, and obtained results that are in general agreement with those of Lockett et al. (1999). Plots from the Lockett et al. (1999) model are displayed in Figure 3.2 and Figure 3.3. The graphs illustrate the effect of temperature, density and dust continuum radiation on the maser optical depth as a function of the OH column density. When the temperature decreases the efficiency of the pump decreases. The temperature needs to be $T \leq 200$ K to populate only the first excited state ($^2\Pi_{3/2}$ $J = 5/2$) of the OH molecule. The upper limit on the temperature is also limited by line overlap, which affects the level populations. Line overlap occurs when the frequencies associated with different transitions are sufficiently close together that the photons emitted by one transition can be absorbed by another. The model indicates that the temperatures most likely to produce a 1720 MHz inversion in OH lie between

$T_K \sim 50$ and $T_K \sim 125$ K, with a maximum inversion occurring for $T_K \sim 75$ K.

The Lockett et al. (1999) model requires that the OH column density be of order $N_{OH} \sim 10^{16}$ cm^{-2} so that decays from the first excited state are optically thick, and $N_{OH} \lesssim 10^{17}$ cm^{-2} to ensure that decays from the $^2\Pi_{1/2}$ $J = 1/2$ levels are optically thin. The $^2\Pi_{1/2}$ $J = 1/2$ levels become optically thick only at higher OH column densities. A significant increase in the OH column density would switch the inversion to the 1612 MHz line. Because of this limitation on the OH column density, the 1720 MHz OH maser optical depth is never large. Very low densities are not compatible with realistic maser gains, which require $N_{OH} \gtrsim 4 \times 10^{15}$ cm^{-2} to give $\tau \gtrsim 2$. The model requires H_2 densities in the range $n_{H_2} \sim 10^4 - 10^5$ cm^{-3}. Quenching by collisions occurs at densities above $n_{H_2} \sim 3 \times 10^5$ cm^{-3} .

The Lockett et al. (1999) model shows that dust continuum radiation at a temperature of 50 K has little effect on the maser inversion, but when the dust continuum radiation increases to 100 K, IR re-radiation, even in the presence of only a small amount of dust, will significantly decrease the 1720 MHz inversion. These conditions should not result in the production of other ground-state masers; the 1612 MHz OH masers require a larger OH column density for their production, and the main line masers require high dust temperatures.

From the discussion presented above, it is clear that shock-excited 1720 MHz OH masers can only occur within a limited range of physical conditions. The production of these masers require moderate temperatures ($T = 50 - 125$ K) and densities ($n \sim 10^4 - 10^5$ cm^{-3}) and an OH column density of $N_{OH} \sim 10^{16}$ cm^{-2}.

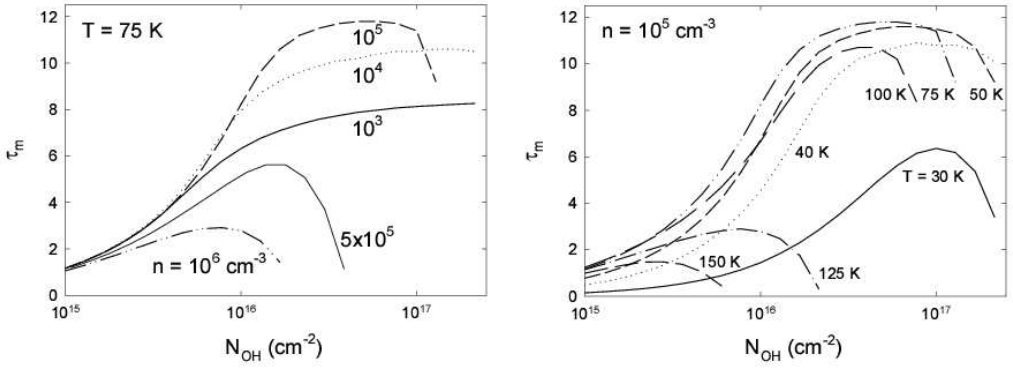

Figure 3.2: Maser optical depth as a function of OH column density for (*left*) various temperatures, at density $n_{H_2} = 10^5$ cm^{-3},(*right*) various densities, at temperature T = 75 K. (From: Lockett et al. (1999))

3.3 Shocks

3.3.1 C- and J-type shocks

Shocks come in two types, either J-type (jump) or C-type (continuous) shocks. A J-type shock is seen as a discontinuous jump in the hydrodynamic flow variables (e.g. Hollenbach 1997; Hollenbach & Mckee 1989a; Smith 1994). The shock front is non-radiative but radiation is emitted after the impulsive heating event. J-type shocks require a medium in which magnetic fields are absent or weak, or where shock speeds are significantly higher than the Alfvén speed [1]. J-type shocks include dissociative shocks with $v_s \gtrsim 30 - 50$ km s^{-1}, or lower velocity shocks with high levels of ionization ($x_{ia} \gg 10^{-6}$). In a J-type shock the neutral and ionised components are coupled and can be regarded as a single fluid.

In a C-type shock the hydrodynamic flow variables of the ions and the neu-

[1]When the gas contains a well coupled magnetic field, disturbances propagate at the bulk Alfvén speed

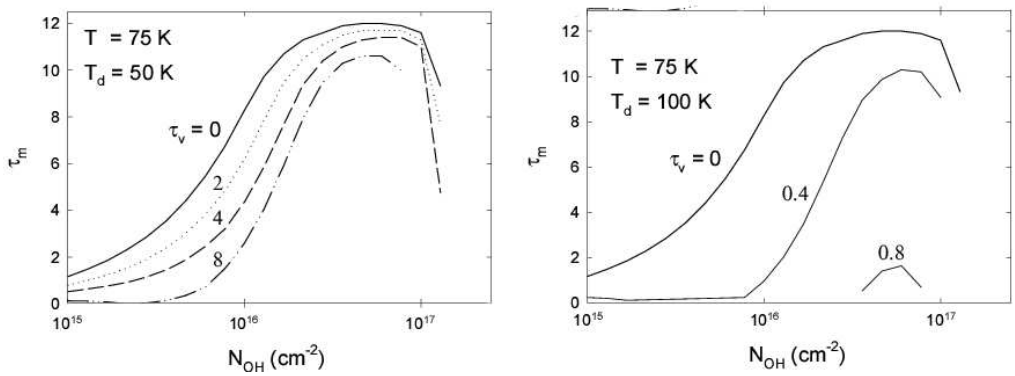

Figure 3.3: Maser optical depth as a function of OH column density for various values of τ_ν. In both panels the gas has a density of $n_{H_2} = 10^5$ cm^{-3} and a temperature of 75 K. The dust temperature is 50 K (*left*) and 100 K (*right*). The plots for $\tau_\nu = 0$ are the same as the corresponding ones in figure 3.2 and are included for reference to show the inversion in the absence of dust. (From: Lockett et al. (1999))

trals change continuously across the shock (e.g. Draine 1980; Hollenbach 1997; Smith 1993). Radiation is emitted as the gas is being heated in the shock front, and nearly the entire flux is produced as IR emission. C-type shocks depend on the presence of a magnetic field and occur at relatively low velocities and low levels of ionization. C-type shocks are generally non-dissociative shocks and occur for $v_s \lesssim 40 - 50$ km s^{-1} if $x_{ia} \lesssim 10^{-6}$. The peak temperature rarely exceeds $\sim 3000 - 5000$ K. In a C-type shock the ions and neutrals are decoupled and are considered as two separate fluids.

In an ionized fluid, the magnetic field is tied to the ions. The ions, in turn, collide with neutral atoms, coupling them to the magnetic field. If the ionization is very low, the neutrals will only encounter an ion very rarely, and so they will not be well-coupled to the field. If the field is strong, it can drag the ions through the neutral gas, a process called "ambipolar diffusion". The ambipolar diffusion mechanism is driven by magnetic field gradients, which are generated by shock compression. When the ion Alfvén velocity is greater

than the shock velocity, compressive magnetic waves can reach the pre-shock gas before the actual (neutral) shock front arrives called a "magnetic precursor". The faster moving ions gradually transfer momentum to the slower moving neutrals and the neutrals are accelerated and heated before the arrival of the neutral J-shock. A systematic decrease in the ionization or the shock velocity or an increase in the magnetic field can eventually lead to the transition from a J-type shock to a C-type shock.

3.3.2 SNR shocks

When a SNR slams into a molecular cloud the material at the shock front is heated to temperatures of $T \sim 1000$ K. As the material streams away from the shock front, it cools and slows down so that the temperature, density and velocity of the medium are unique functions of the distance from the front. The model of Lockett et al. (1999) shows that observable 1720 MHz masers and the physical conditions needed to produce them can only exist behind the shock front of a C-type shock. Since the OH abundance relative to H_2 is probably no more than $n_{OH}/n_{H_2} \sim 10^{-5}$, a lower limit of $N_{H_2} \sim 10^{21}$ cm^{-2} for the H_2 column density of the maser is required; such a column must be produced behind the shock front as the material cools down from $T \sim 125$ K to $T \sim 50$ K (Lockett et al. 1999).

J-shocks can not meet the requirements of these high column densities at low thermal pressures. In a J-type shock the cooling time spent behind the shock front is too short to produce the necessary column density in the specified temperature range. This problem can be overcome only if there is some heating mechanism that can counter the cooling and maintain the required

temperature range for a longer period of time.

Lockett et al. (1999) found that the most efficient method of heating the shocked material was provided by ambipolar diffusion, which occurs when flux freezing breaks down in C-type shocks. Ambipolar diffusion in C-shocks can overcome the rapid cooling and extend the warm region behind the shock front. No such heating mechanism is known for J-type shocks. Lockett et al. (1999) concluded that the conditions necessary for the production of 1720 MHz OH masers requires that the shock must be of C-type with a pre-shock density of $n_{H_2} \sim 10^4$ cm^{-3}, and a shock velocity of $v_s \sim 10 - 50$ km s^{-1}. This is consistent with the detailed C-shock calculations performed by Draine, Roberge & Dalgarno (1983) in their intermediate density model, in which the required conditions are achieved with a pre-shock density of $n = 10^4$ cm^{-3} and a shock velocity of $v_s = 25$ km s^{-1}.

The Lockett et al. (1999) model shows that detectable maser amplification requires a sufficient column of molecules with a small velocity gradient, so that Doppler shifting of the transition frequency does not prevent amplification from occurring along the entire column. Because the largest velocity coherence will be produced in a direction perpendicular to the motion of the shock front, an edge-on geometry (i.e. a shock front moving perpendicular to the line-of-sight of an observer) will favor the detection of masers.

3.4 OH Production

Inactive molecular gas consists mainly of H_2, He, CO and either atomic or diatomic O, with a very low abundance of OH molecules. Although OH is

produced behind a C-type shock by the endothermic reaction

$$O + H_2 \longrightarrow OH + H$$

if $T > 400$ K, it is consumed by the faster, less endothermic reaction

$$OH + H_2 \longrightarrow H_2O + H \ .$$

Thus the shock converts all of the pre-shock oxygen into O_2 and H_2O, rather than OH, suggesting that the OH necessary for the production of 1720 MHz OH masers behind C-type shocks is not directly produced by the shock chemistry (Draine et al. 1983; Hollenbach & Mckee 1989b; Kaufman & Neufeld 1996). The Lockett et al. (1999) model lists the physical conditions needed to create masers, but it fails to explain how the OH itself is produced. The strength of a dissociating ultraviolet (UV) field should be strong enough to produce enough OH, but not so strong as to increase the electron abundance too much, as this would have a significant effect on the structure of the shock (Lockett et al. 1999). In OH masers associated with compact H II regions, a strong far-ultraviolet (FUV) flux from the central, young, massive star photo-dissociates the water molecules to produce enough OH (Elitzur & de Jong 1978; Hartquist & Stenberg 1991; Hartquist et al. 1995). This, however, would not be possible in the case of the SNR masers, since the heating of intervening dust grains by such a FUV flux would produce a strong FIR continuum, which suppresses the inversion of the 1720 MHz line, and inverts the main-line transitions (Wardle, Yusef-Zadeh & Geballe 1999).

The flux of cosmic rays in the ISM is insufficient to produce the necessary abundance of OH for masers, as is a flux of hard X-rays from SNRs (Lock-

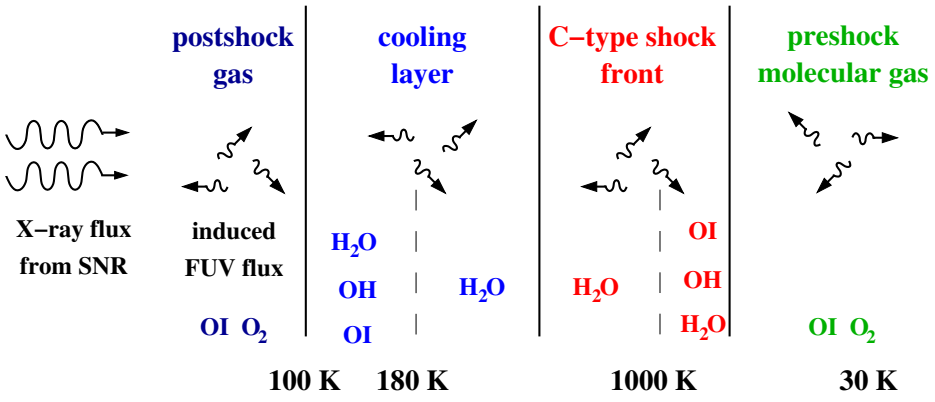

Figure 3.4: A model for the production of OH in molecular clouds associated with SNRs. A C-type shock is driven into a molecular cloud. The X-ray flux from the SNR interior induces a weak secondary FUV flux throughout the cloud. The shock converts atomic and molecular oxygen into water. Once the shocked gas cools, water is subsequently dissociated to OH and then to O I by the secondary UV flux.

ett et al. 1999). However, energetic electrons are produced when material in molecular clouds is ionized by cosmic and X-rays. These electrons collisionally excite H_2 into the Lyman α and Werner bands and the subsequent radiative decay produces a FUV photon capable of dissociating water (Wardle 1999). Wardle (1999) argued that the X-ray spectrum from the hot gas in SNRs is softer than that assumed by Lockett et al. (1999). Because the interaction cross section decreases at high photon energies, a soft spectrum ionizes more material than a hard spectrum. Wardle (1999) concluded that the X-ray flux due to bremsstrahlung from the hot gas inside the SNR can produce a sufficient column of OH behind a C-type shock. An ionization rate of $\zeta = 10^{-16}$ s^{-1}, will convert roughly 10% of the H_2O into OH. Figure 3.4 illustrates the mechanism for the production of OH necessary for the formation of 1720 MHz OH masers associated with SNRs.

The resulting picture is then as follows: A SNR drives a shock front into

a molecular cloud. The expansion is slowed at the clouds location and the remnant is distorted. A reflected shock is driven into the remnant's interior as it runs into the obstacle, as illustrated in Figure 3.5. A C-type shock accelerates, heats and compresses the gas, and combines atomic and diatomic oxygen with hydrogen to produce water. The shocked, water-rich gas cools as it drifts behind the shock front. The entire shock structure is subject to the weak dissociating FUV flux produced by X-rays from the SNR interior. However, the dissociation cannot compete with the rapid reformation of water until the temperature drops below $T = 200$ K, at which point the water is dissociated to OH. Behind the C-type shock, moderate temperatures and densities, and a sufficient column of OH, give rise to 1720 MHz OH masers as shown in Figure 3.6. The model completely rules out the possibility of a J-type shock; only C-type shocks can produce the required conditions for

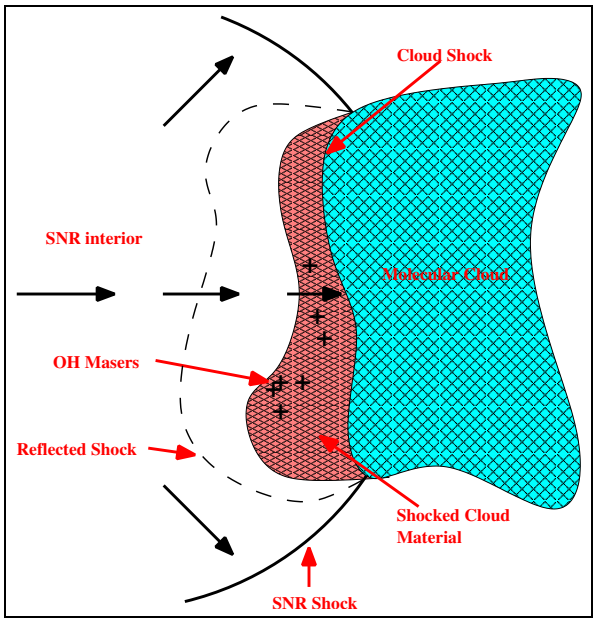

Figure 3.5: A schematic of an expanding SNR interacting with an ISM molecular cloud. Black arrows indicate velocity.

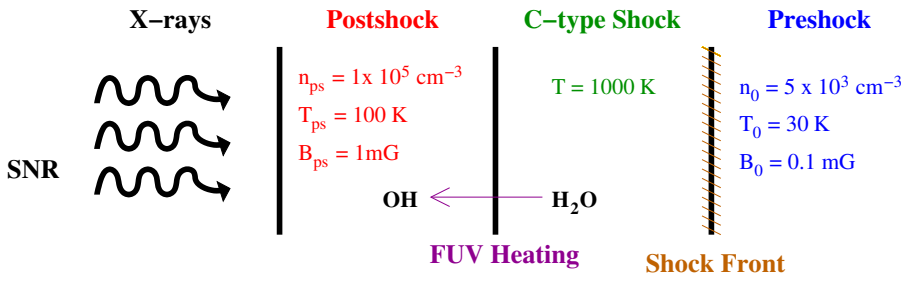

Figure 3.6: Simplified model of a SNR-molecular cloud interaction

the production of the 1720 MHz OH masers. Because of the tight physical conditions required behind the shock, even a C-type shock can be incapable of generating the optimal conditions. Because of the wide margin by which J-type shocks fail to produce the required conditions, the presence of 1720 MHz masers should be an indicator of C-type shocks.

The tight constraints on the production of these masers explain their low detection rate, but also makes them a powerful probe of the regions in which they are formed. Even under optimal pumping conditions, the 1720 MHz maser barely reaches saturation for radiation propagating perpendicular to the line-of-sight. When the optical depth is increased to the point that the amplified maser intensity is at saturation level, the OH column density is already so large that the inversion switches to the 1612 MHz maser (Lockett et al. 1999).

3.5 Implications of the Model

The current models for the production of 1720 MHz OH masers towards SNRs clearly indicate the physical association between these masers and the SNR-molecular cloud interaction. But are these models correct? Demonstrating a physical association between a SNR and a molecular cloud, and finding specific cases of such interactions in our Galaxy has always been difficult. Unrelated gas along the line-of-sight makes it difficult to determine whether a SNR is physically associated with a molecular cloud, or whether they are at different distances and only appear positionally coincident because of a projection effect (Reynoso & Magnum 2000). Although 1720 MHz OH masers are not as common in H II regions as the OH main-line masers (Gaume & Mutel 1987), they do exist, and in some cases they are found without emission from any of the other ground-state OH transitions, as in the case of the H II region S106 (Loushin 1989). Models show that 1720 MHz OH masers towards SNRs are formed under very tight constraints on the physical conditions surrounding these masers. Therefore, the non-detection of masers toward SNRs does not rule out the possibility of an interaction between the SNR and a molecular cloud, only that the conditions might not be favorable for the production of 1720 MHz masers. Koralesky et al. (1998) detected no masers towards the SNR Cas A and G109.1–1.0, both of which show some evidence of an interaction with a molecular cloud (Tatematsu et al. 1990; Keohane, Rudnick & Anderson 1996).

The pumping calculations require that 1720 MHz OH masers towards SNRs should arise under limited ranges of temperature, density and OH column density, and that these conditions do not result in the production of other ground-state masers. The model also requires the absence of a high tem-

perature FIR field. Many SNRs show strong IR continuum radiation that would preferentially invert the levels associated with the main line masers (Lockett et al. 1999). If these constraints on the physical conditions are in agreement with observational results, it would clearly establish that the 1720 MHz masers towards SNRs are indeed produced at the shock interface of a SNR with a molecular cloud (Lockett et al. 1999). The amount of OH produced by the dissociation process should be sufficient to detect thermal OH absorption in the other ground-state transitions of OH provided the background continuum is strong (Wardle 1999). The model also implies the non-detection of 22 GHz water masers in association with the 1720 MHz OH masers (Lockett et al. 1999). Strong water masers are often produced in the molecular gas surrounding H II regions for which 300 K $\leq T \leq$ 600 K and $n_{H_2} \sim 10^9$ cm^{-3} (Hollenbach 1997). Hence, the H_2O column density that is sufficient to produce enough post-shock OH for 1720 MHz OH masers to form, would be too low to produce detectable water masers.

Lockett et al. (1999) found that the largest maser amplification will be in the direction of largest velocity coherence, requiring that detectable masers should only be in that part of the shock that is perpendicular to the line-of-sight. This geometric constraint means that the maser velocity should be close to that of the systemic velocity of the SNR, or the velocity of the unshocked gas of the molecular cloud (Lockett et al. 1999). Therefore, the radial velocities of the masers should be characteristic of the galactic neighborhood of the SNR. If the model is wrong and these 1720 MHz OH masers are indeed not formed behind a C-type shock, but produced in the recombination zone of a J-type shock, the maser velocities might be expected to be displaced from the systemic velocity of the SNR, as is found for H_2O masers (Frail et al. 1996). According to the model, the 1720 MHz masers should be

found in the post-shock gas along the shock interface. Thus, an important signature for establishing whether a particular maser detection is associated with a SNR, is a close agreement in both position and velocity of the 1720 MHz OH masers and the SNR (Koralesky et al. 1998).

Chapter 4

Observational Results of Maser Emitting SNRs

This chapter deals with the observations associated with 1720 MHz OH maser emitting SNRs. Modelling of these masers show that they arise under restrictive conditions behind C-type shocks through the interaction of a SNR with a molecular cloud. When a SNR interacts with the ISM it also produces shocked line emission from ionized gas, atomic gas and molecular gas, as well as FIR emission and radio and X-ray continuum emission. Observational studies of these masers and the regions surrounding them have revealed a number of characteristic properties and show that the current model predictions are in good agreement with the observational results.

4.1 Model Requirements and Observational Results

The tight contraints on the temperature, density and OH column density required by the 1720 MHz OH collisional pump is also well established by observations and a few examples are given below. Observational studies of molecular clouds show that the ambient pre-shock density for SNRs W28, W44 and 3C 391 are consistent with model predictions (Wootten 1977, 1981; Reach & Rho 1998). Post-shock measurements of these three remnants determined temperatures of $T \sim 80$ K, and densities of $n = 10^4 - 10^5$ cm^{-3} (Frail & Mitchell 1998). Frail et al. (1994) found a post-shock OH column density in the range of $N_{OH} = 10^{16} - 10^{17}$ cm^{-2} for the SNR W28. Lazendic et al. (2002) derived OH column densities of $N_{OH} \sim 10^{16}$ cm^{-2} towards W28, G349.2+0.7 and G337.0–0.1. Many molecular observations have verified that the post-shock temperature for the SNR IC 443 is in the range of $T = 33 - 100$ K, and the post-shock density is in the range of $n = 1 - 8 \times 10^5$ cm^{-3} (e.g. Turner et al. 1992; Dickman et al. 1992; van Dishoeck, Jansen & Phillips 1993; Cesarsky et al. 1999; Rho et al. 2001). van Dishoeck et al. (1993) found a post-shock temperature of $T \sim 80$ K, and a post-shock density of $n \sim 10^5$ cm^{-3} for IC 443. Arikawa et al. (1999) determined pre- and post-shock temperatures of $T \lesssim 20$ K and $T \gtrsim 60$ K, and pre- and post-shock densities of $n \lesssim 10^3$ cm^{-3} and $n \gtrsim 10^4$ cm^{-3} for IC 443.

Claussen et al. (1999) conducted observations toward selected regions of the SNRs W28, W44 and IC 443 in a search for water masers, but made no detections except for an unrelated H_2O maser detected towards W44. The detection of 1612 MHz OH emission at the same position and velocity as

the water maser led Claussen et al. (1999) to suggest that this maser is not related to the SNR shock, but is due to a late-type giant or super-giant star along the line-of-sight to W44. An H_2O maser was identified near the center of the SNR Kes 78, coincident with main-line OH maser emission (Koralesky et al. 1998). It is believed that the OH masers are related to an H II region along the line-of-sight. The non-detection of water masers towards 1720 MHz OH maser-emitting SNRs places constraints on the post-shock density of the gas. These constraints are consistent with the limits predicted by the model.

Relatively low dust emission and dust temperatures, consistent with model predictions, are observed towards maser sources. For example, van Dishoeck et al. (1993) determined a dust temperature of $T \sim 45$ K for IC 443, and Reach & Rho (1996) measured a dust temperature of $T = 50$ K for 3C 391. It has been shown that SNRs lying towards the Galactic center (Yusef-Zadeh et al. 1999) are located outside the region of intense IR emission (Mezger, Duschl & Zylka 1996). Brogan et al. (2004) noted a lack of masers in the regions of near-IR (NIR) dust emission toward the SNR N49 in the LMC.

One of the most striking observational discoveries associated with masers in SNRs has been the detection of spatially extended 1720 MHz OH emission associated with compact maser spots. Extended 1720 MHz OH emission has been observed in the five SNRs G359.1–0.5, G357.7+0.3 and G357.7–0.1 and W28 (Yusef-Zadeh et al. 1995, 1999; Yusef-Zadeh, Wardle & Roberts 2003). The extended emission in W28 has line widths of about $1 - 3$ km s^{-1} (Yusef-Zadeh et al. 2003). It is believed that the extended OH features are low gain masers or weak amplification in the OH behind a face-on shock front, as opposed to the edge-on geometry required by maser spots (Yusef-Zadeh et al. 2003). Yusef-Zadeh et al. (2003) suggested two new ways to search for

SNR-molecular cloud interaction sites, even when 1720 MHz OH masers are absent. One method is to look for extended OH with broad line widths in absorption at 1612, 1665 or 1667 MHz. OH absorption is seen toward the SNRs IC 443 (DeNoyer 1979a), G349.2+0.7 (Lazendic et al. 2002), W28 and W44 (Goss 1968; Goss & Robinson 1968; Turner 1969; Robinson et al. 1970; Pastchenko & Slysh 1974). The second method is to search for extended, weak 1720 MHz OH line emission. The extended OH emission does not require the shock to propagate almost perpendicular to the line-of-sight, and therefore should be more generic.

4.2 Intrinsic Properties of Maser Spots

The brightness temperature of the maser spots in W28 were measured to have a lower limit of $T_B > 4 \times 10^5$ K (Frail et al. 1994). Claussen et al. (1997) found brightness temperatures in the range $T_B = 2 \times 10^4 - 10^8$ K for the maser spots in W28, W44 and IC 443. However, due to unresolved maser features around the same velocity, these values may be the lower limits on the true values of the brightness temperature (Claussen et al. 1997).

OH masers in H II regions have sizes of ~ 2 mas and have been observed to be variable (Masheder et al. 1994). Brogan et al. (2000) have shown that since the detection of the OH masers in the SNRs W51C, G349.7+0.2, CTB 37A, CTB 33 and G357.7–0.1 in 1994, there has been no significant change in either the position of the masers or their flux density. Unscattered sizes between 30 mas and 240 mas have been found for the masers in SNRs W28 and W44 (Claussen et al. 1999). Hoffman et al. (2005) found the masers in W28 to have deconvolved sizes between 90 and 350 mas, with compact cores

of 20 mas. The most reliable measure of intrinsic maser size comes from the SNR IC 443 because it lies near the Galactic anti-center (Frail et al. 1994; Claussen et al. 1999). IC 443, located at a nearby distance of 1.5 kpc, is expected to show less than 1 mas of scatter broadening (Lazio & Cordes 1998a,b). Data from Hoffman et al. (2003) shows that the masers towards IC 443 have a core/diffuse morphology with deconvolved sizes in the range $90 - 180$ mas, and compact cores with sizes in the range $15 - 55$ mas.

4.3 Magnetic Field Detections

It has long been known that SNRs possess magnetic fields. In the absence of a magnetic field, a supernova blast wave would heat, compress and fragment the cloud and may ultimately destroy it (Klein, Mckee & Colella 1994). Polarization studies of synchrotron emission produced by the SNR can only determine the direction of the magnetic field in the plane of the sky (e.g. Milne 1990; Dickel, van Breugel & Strom 1991). However, until recently determination of the strength of the magnetic field had to rely on the rather doubtful equipartition approximation. The discovery of 1720 MHz OH masers associated with SNRs has changed this situation in allowing for a measurement of the strength of the magnetic field along the line-of-sight through Zeeman splitting (e.g. Troland & Heiles 1982).

When the observed Zeeman splitting of the 1720 MHz OH line is small compared to the line width, a quantity denoted by B_θ that depends on the total magnetic field strength $\mathbf{B}$ and the angle between the line-of-sight and $\mathbf{B}$ can be determined (Brogan et al. 2000). This method yielded values for B_θ between 0.1 and 4 mG in Sgr A East, W44, W28, G32.8–0.1 and G346.6–0.2

(Yusef-Zadeh et al. 1996; Claussen et al. 1997; Koralesky et al. 1998). Brogan et al. (2000) measured Zeeman splitting towards W51C, G349.7+0.2, CTB 37A, CTB 33 and G357.7+0.1 and found field strengths to range from $B_\theta \sim 0.2 - 2$ mG. These magnetic fields have been calculated from the Zeeman effect in masers using the same formalism that has been developed for thermal radiation. However, stimulated emission is intrinsically different from spontaneous emission or absorption. It is thus possible that the magnetic fields are overestimated and could be reduced by as much as a factor of $\lesssim 5$.

Brogan et al. (2000) shows that the compression of the ambient magnetic field by the SNR shock, as opposed to turbulent amplification (Jun & Norman 1996), is all that is required to produce the magnetic field strengths they observed. Magnetic pressures estimated from the values of B_θ were found to range between $10^{-7} - 10^{-9}$ erg cm^{-3}. This range of magnetic pressures far exceed the pressure in the ISM or even the thermal pressure of the hot gas interior to the remnants and are in very good agreement with the ram pressure expected from C-type radiative shocks (see Brogan et al. (2000) and references therein).

4.4 Characteristics of Shock Excited Gas from SNRs

4.4.1 Radio and X-ray Emission from SNRs

One of the defining primary signatures used to identify SNRs are their integrated radio continuum spectra . The radio emission from SNRs is believed to be synchroton radiation. For some SNRs the central pulsar is the source of both the relativistic particles and the magnetic field (Reynolds & Chevalier 1984), whereas for other SNRs the relativistic particles and the magnetic field come from the ambient ISM. Measurements of the magnetic fields in SNRs (see § 4.3) are an order of magnitude higher than the ambient magnetic field, which requires magnetic field amplification by the SNR shock. The contact discontinuity between the shock front and the shocked medium is unstable and produces a thin shell of turbulence. The turbulence in the shell is believed to be the source of particle acceleration within the shell and magnetic field amplification by turbulent mixing (Chevalier 1982). It is believed that a combination of particle acceleration in the shock front (Bell 1978a,b) and magnetic field amplification as well as particle acceleration behind the shock front (Cowsik & Sarkar 1984; Gull 1973) are responsible for the observed radio brightness from SNR shells. Observational confirmation of the above theoretical ideas of particle acceleration in SNR shocks has been provided by HESS (High Energy Stereoscopic System) telescope results, presented by Aharonian (2004).

The X-ray appearance of a SNR is also believed to be affected by the interaction of the SNR with a molecular cloud or dense atomic gas. Most

X-rays that SNRs emit are thermal emission that comes from hot gas. As a SNR plows through the ISM, it sweeps up ISM material and a reverse shock propagates into the slower moving ejecta. The SNR heats the swept-up and ejecta components to produce X-rays via thermal emission processes (e.g. Hwang, Hughes & Petre 1998). Thermal Bremsstrahlung and Black body radiation provides unpolarized continuum emission. The spectra from these thermal X-rays generally show a characteristic set of recombination lines of highly ionized, heavy metals. In addition X-rays can also appear in the form of synchroton radiation due to particle acceleration and magnetic field amplification in the shock front (e.g. Reynolds 1996). As in the case of the radio continuum emission, the synchroton X-ray emission observed in many SNRs is driven by the rotational energy losses of the central neutron star (e.g. Harrus & Hughes 1996). The synchrotron radiation forms a hard continuum that has no emission lines and are polarized at a $10 - 20\%$ level.

Galactic SNRs are traditionally classified into three broad categories; Shell-type, Crab-like and Plerionic composites, based mainly on their radio morphology (Seward 1985). Rho & Petre (1998) introduced the term mixed morphology (MM) SNRs for a group of SNRs that shows different X-ray and radio morphologies.

Shell-type SNRs are seen as ring-like structures (often incomplete). As a shock wave from a supernova explosion plows through space it produces a big shell of shocked material. Due to limb brightening a ring-like structure can be seen in both X-ray and radio. The Cygnus Loop shown in Figure 4.1 is an example of a Shell-type remnant.

Crab-like/Plerions look more like a blob than a ring, where the X-ray and radio emission comes from the central region. The plerionic

emission is believed to be driven by the rotational energy losses of the central neutron star. However, the blast wave should produce a shell of emission where it interacts with the ISM, but no such shell has been found in either radio (Frail et al. 1995) or X-ray emission (Predehl & Schmitt 1995). It has been suggested that the absence of a shell is due to the SNR expanding into a low density medium (Frail et al. 1995). An example of this type of remnant is the Crab Nebula which is shown in Figure 4.1

Composite Remnants are a cross between the Shell- and Crab-like remnants. They appear Shell-like, Crab-like or both, depending on whether they are observed in the X-ray or radio part of the electromagnetic spectrum.. There are two kinds of composite remnants:

Plerionic composites shows emission from the central region (Crab-like) and in a shell (Shell-like) in both X-ray and the radio. The X-ray spectra of the central region do not have spectral lines whereas the X-ray spectra near the shell do have spectral lines.

Thermal Composites/MM SNRs appear shell-like in the radio waveband (synchrotron radiation). In X-rays, however, they appear Crab-like, but unlike the true Crab-like remnants their X-ray spectra have spectral lines, indicative of hot gas. SNR IC 443, shown in Figure 4.1, is an example of a MM SNR.

Conventional wisdom was that the dominant X-ray emission would be found on the outside rim of the remnant where the forward shock is located. However, MM SNRs are different from other classes in that their dominant X-ray

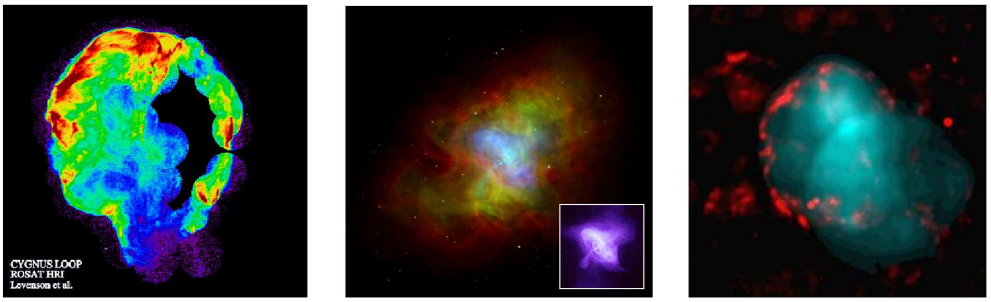

Figure 4.1: (*left*) Cygnus loop as an example of a Shell-type remnant in high resolution X-rays taken with the ROSAT HRI (High Resolution Imager) (Credit: Rosat HRI and Levenson et al.)
(*middle*) The Crab Nebula as an example of a Crab-like remnant shows a composite image with red indicating radio emission, green indicating optical emission and blue indicating X-rays (Credit: *X-rays*: NASA/CXC/ASU/J. Hester et al.; *Optical*: NASA/HST/ASU/J. Hester et al.; *Radio*: VLA/NRAO); included is an X-ray image in which the nebula and the pulsar are clearly visible (Credit: NASA/CXC/SAO)
(*right*) IC 443 as an example of a MM SNR as a composite image with red indicating radio emission and blue indicating X-rays. (Image courtesy of Jonathan Keohane)

emission mechanism is thermal (at a temperature below about 1 keV) despite their X-ray morphological similarity to Crab-like remnants, and their emission arises primarily from swept up interstellar material rather than ejecta (Rho & Petre 1998). Currently there are two models that may account for the observed properties of MM remnants. One model proposes that the X-ray emission is due to gas evaporated from clouds, while the other model proposes that as the shell of an expanding SNR cools and its emission becomes too soft to detect through the absorbing ISM, the X-rays from the hotter interior are still detectable as "fossil" thermal radiation (Rho & Petre 1998). Cox et al. (1999) suggested that both mechanisms work in combination to produce the observed X-ray spectrum. Two common factors about these models is the key role played by thermal conduction and the need for a denser than average ISM near the remnant (Rho & Petre 1998).

It is believed that there is significant overlap between MM SNRs and maser emitting SNRs. Both are thought to arise through the interaction with an adjacent molecular cloud (MM remnants may also arise from the interaction of a SNR with a dense atomic region (Yusef-Zadeh et al. 2003)) and soft thermal X-rays emitted from MM SNRs appear to be a necessary ingredient for enhancing OH behind the shock front (Wardle 1999). It is therefore suggested that all of the maser remnants should display mixed morphology (Yusef-Zadeh et al. 2003).

Yusef-Zadeh et al. (2003) found a strong correlation between maser emitting SNRs and MM remnants. Their analysis shows that there is statistical evidence for an association between these two classes of remnants. They have divided all known 1720 MHz maser emitting SNRs into three broad classes as indicated in column 4 (X-ray class) of Table 4.1. Group 1 have MM counterparts, group 2 show X-ray emission but future observations are required to determine the morphology and spectrum, and group 3 have unknown X-ray properties and have either been unobserved in X-rays or their soft X-ray emission has been absorbed by intervening interstellar gas. However, not all MM remnants as tabulated by Rho & Petre (1998) are maser-emitting. It could be that masers failed to arise in these MM remnants because of the restrictive physical conditions under which these masers form, or the masers could simply be beamed away from the line-of-sight (Yusef-Zadeh et al. 2003).

Yusef-Zadeh et al. (2003) investigated the role of X-ray emission from maser-emitting SNRs by comparing the X-ray induced ionization rate with the theory. The X-ray ionization rate in the gas should be $\zeta \gtrsim 10^{-16}$ s^{-1} to dissociate enough H_2O to produce detectable 1720 MHz OH masers (Wardle 1999). Yusef-Zadeh et al. (2003) measured the X-ray ionization rate at the

edge of maser emitting SNRs whose thermal spectrum and MM have previously been identified (Column 5 of Table 4.1). They conclude that these rates are indeed sufficient to enhance the OH behind a C-type shock and produce detectable 1720 MHz OH masers.

4.4.2 Signatures of Molecular Shocks

For individual SNRs there exists morphological, kinematical and chemical signatures of an interaction with a molecular cloud. Identification of a SNR interacting with a molecular cloud is based on its proximity to the molecular cloud. Morphological signatures also includes the detection of arcs and shells of molecular gas outlining the SNR (where gas has been swept up by the blast wave) and the distorted appearance, indentation or flattening of the SNR shell as traced by the radio continuum emission and local increases in the synchroton emissivity. The velocity of the pre-shock molecular cloud should be in agreement with the systemic velocity of the adjacent SNR. Shock-accelerated H I gas seen at velocities different from those allowed by pure Galactic rotation are indicative of an interaction.

However, the most convincing way of demonstrating the presence of an interaction between a SNR and a molecular cloud is to look for the characteristic line emission from molecules that have been excited by the shock. In recent years the emphasis in the study of such interactions has shifted away from centimeter wavelengths to millimeter and sub-millimeter wavelengths, where the important transitions from shocked molecular species are in abundance (e.g. van Dishoeck et al. 1993; Arikawa et al. 1999). Observational evidence from shock excited molecules indicating a SNR-molecular cloud interaction

can include, millimeter-wave emission lines with line widths much greater than those of cold gas, bright FIR line emission, IR cooling lines from H_2, OH and CO and [O I] tracing regions that are both hot and dense, NIR H_2 emission and also the detection of 1720 MHz OH maser emission. 1720 MHz OH masers should be associated with C-type shocks, and C-type shocks are strong sources of emission in the $1-0$ $S(1)$ line of H_2 at 2.12 μm (Draine et al. 1983; Draine & Roberge 1982; DeNoyer 1983). Signatures to establish whether a 1720 MHz OH maser detection is physically associated with a SNR includes a close agreement in both position and velocity. The masers should be found interior to or along the radio continuum edges of the SNR at the systemic velocity of the SNR and should be unaccompanied by 1612, 1665 and 1667 MHz OH emission. The detection of thermal X-rays associated with MM remnants are also an indication that the SNR is interacting with a dense molecular cloud.

4.4.3 Observational Results for Individual SNRs

All 1720 MHz OH maser emitting SNRs discovered to date (2005 October) are listed in Table 4.1. For each remnant, the number of compact maser spots detected toward the remnant are given, as well as its spectral-type radio structure. The properties of the regions surrounding these masers have been measured through numerous observations. The spatial and kinematical associations of the SNRs with their 1720 MHz OH masers as well as other important observational signatures indicating an interaction are discussed below for individual SNRs.

SNR Name	No. of Masers	Radio Structure[a]	X-rays[b]	ζ ($\times 10^{-16} s^{-1}$)	References[c]
G0.0+0.0(Sgr A East)	9	S	Group 1	3.9	1 & 7,2,3
G1.05-0.1(Sgr D)	1	S	Group 2	2.3	1 & 6,2,3
G1.4–0.1	2	S	Group 3	6.3	1 & 6,2,3
G6.4–0.1(W28)	41	C/S	Group 1	4.5	1,2,3
G16.7+0.1	1	S	Group 2	8.8	1,2,3
G21.8–0.6(Kes 69)	1	S	Group 2	3.6	1,2,3
G31.9–0.0(3C 391)	2	S	Group 1	0.6	1,2,3
G32.8–0.1(Kes 78)	1	S	Group 3		4,2,3
G34.7–0.4(W44)	25	C	Group 1		1,2,3
G49.2–0.7(W51C)	2	S	Group 1		1,2,3
G189.1+3.0(IC 443)	6	C	Group 1		1,2,3
G337.0–0.1(CTB 33)	3	S	Group 3		1,2,3
G337.8–0.1(Kes 41)	1	S	Group 2		4,2,3
G346.6–0.2	5	S	Group 2		4,2,3
G348.5+0.1(CTB 37A)	10	S	Group 3		1,2,3
G349.7+0.2	5	S	Group 2		1,2,3
G357.7–0.1(Tornado Nebula)	1	?	Group 2		1,2,3
G357.7+0.3(Square Nebula)	5	S	Group 2		1 & 6,2,3
G359.1–0.5	6	S	Group 1		1,2,3
N49(LMC)	2	?	Group 2		5,-,5

Table 4.1: Observational properties of all known SNRs with 1720 MHz OH masers

[a]Radio Structure can be either 'S', 'F' or 'C' if the remnant shows a 'shell', 'filled-center' or 'composite' radio continuum structure.

[b]Group1: SNRs with MM counterparts, Group 2: Shows X-ray emission but morphology and spectrum are unknown, Group 3: Unknown X-ray properties.

[c]REFERENCES.—(1) Green et al. (1997), and references therein; (2) Green (2001); (3) Yusef-Zadeh et al. (2003); (4) Koralesky et al. (1998); (5) Brogan et al. (2004); (6) Yusef-Zadeh et al. (1999) (7) Yusef-Zadeh et al. (1999).

Sgr A East Yusef-Zadeh et al. (1996) and Green et al. (1996) discovered 1720 MHz OH masers distributed along the rim of the Sgr A SNR as traced by the radio continuum emission where the acceleration is considered to be perpendicular to the line of sight. Yusef-Zadeh et al. (1996) did not detect any 1665 or 1667 MHz OH emission. Seven of the masers located on the eastern side of the remnant (Sgr A East) show velocities (Yusef-Zadeh et al. 1996; Green et al. 1996) that are consistent with velocity measurements of the molecular gas in the region as seen in H I absorption and CS emission (Serabyn, Lacy & Achtermann 1992; Lasenby, Yusef-Zadeh & Lasenby 1989). The eighth maser spot showed a number of velocity components much higher than those measured for the other seven masers and are located where the western arm of the SNR (Sgr A West) crosses the circumnuclear disk (CND). It is not clear whether this maser is associated with cloud-cloud collisions in the CND or whether it indicates for the first time an interaction of Sgr A West with a molecular cloud (Yusef-Zadeh et al. 1996). Sgr A East has been interpreted by many to be interacting with a giant molecular cloud (Mezger et al. 1989; Zylka, Mezger & Wink 1990; Ho et al. 1991; Lasenby et al. 1989). The high-resolution observations of Yusef-Zadeh et al. (1999) detected two additional masers in Sgr A East and noted a large velocity difference between the masers located to the southwest of the remnant and the maser source in the northwest of the shell that may be the result of a strong tidal shear experienced by the molecular cloud. Wardle et al. (1999) observed H_2 $1-0$ $S(1)$ emission toward Sgr A East and concluded that the observed line intensity is consistent with the expected shock strength.

Sgr D and G1.4–0.1 Sgr D is a bright radio continuum source that con-

sists of an H II region (G1.13–0.10) and a SNR (G1.05–0.15) (Yusef-Zadeh et al. 1999). In their survey for maser emitting SNRs near the Galactic center, Yusef-Zadeh et al. (1999) detected maser emission toward the SNRs G1.05–0.15 and G1.4–0.1. No follow-up observations have been made.

W28 Early single dish observations (Goss 1968; Goss & Robinson 1968; Turner 1969; Robinson et al. 1970) discovered bright, narrow 1720 MHz OH line emission toward the SNR W28, together with broad OH absorption features at 1612, 1665 and 1667 MHz (see Figure 3.1. It has also been shown that this SNR interacts with a molecular cloud (Pastchenko & Slysh 1974; Slysh et al. 1980; Wootten 1981). Pastchenko & Slysh (1974) mapped the 1667 MHz OH absorption line which shows the molecular cloud adjacent to the SNR with the 1720 MHz OH masers in the middle of the molecular cloud in the immediate vicinity of the SNR. The crescent shape of the molecular cloud is suggested to be due to the interaction with the molecular cloud. Slysh et al. (1980) traced the molecular cloud from H_2CO absorption and show that the H_2CO line widths broaden significantly as one moves toward the SNR. Measurements by Wootten (1981) showed significant broadening of the CO line widths where the cloud meets W28. The cloud is warmer than typical CO clouds in the Galaxy, and emission from ^{13}CO and HCO^+ is strongest near W28. DeNoyer (1983) did not find evidence for a shock in the form of abundance enhancements of various species.

Interferometric observations (Frail et al. 1994) of the 1720 MHz OH line towards W28 showed 26 distinct maser spots along the edge of the radio continuum emission, with the strongest masers located at the radio continuum peak. Improved resolution observations by Claussen

et al. (1997) detected 41 individual maser spots behind the leading edge of the SNR W28 and shows that several of the (Frail et al. 1994) maser spots are blended features. The masers in W28 show a large velocity distribution between masers in different regions of the SNR, with small velocity dispersion for masers within individual regions (Claussen et al. 1997). Some of the masers, and the molecular gas associated with them, are blueshifted by ~ 10 km s^{-1} from the systemic velocity of the SNR. As an explanation for this velocity dispersion it has been suggested that this molecular cloud is accelerated toward the line-of-sight (Claussen et al. 1997). It is suggested that the broad range of maser velocities are caused by the interaction of the SNR with more than one molecular cloud (see Claussen et al. (1997) and references therein).

Maps made in the ^{12}CO $J = 3 - 2$ line suggest the compression of the gas by a passing shock, and reveal that the masers are close to but not coincident with the CO peaks (Frail & Mitchell 1998). The CO gas shows a strong correlation to the radio continuum emission, where broad CO line widths indicative of warm, high density shocked gas, are seen along the radio continuum ridges and narrow CO lines, indicative of low density, cold gas associated with the ambient molecular cloud, are seen off the ridges (Frail & Mitchell 1998; Arikawa et al. 1999). A study of these components by Arikawa et al. (1999) revealed a line width of 3 km s^{-1} for the unshocked gas, and a line width of $\gtrsim 20$ km s^{-1} for the broad components, with a maximum reaching 70 km s^{-1}. The intensity of the broad component is stronger in CO $J = 3 - 2$ than in CO $J = 1 - 0$, while the intensity of the narrow component tends to be stronger in CO $J = 1 - 0$ than CO $J = 3 - 2$. The $(J = 3 - 2)/(J = 1 - 0)$ line intensity ratio is $0.4 - 0.7$ in the narrow

component from the unshocked gas, while the ratio is $2.3 - 2.8$ in the broad component from the shocked gas.

Yusef-Zadeh et al. (2003) detected 1667 MHz OH absorption with broad line widths, as well as extended, weak 1720 MHz OH emission with narrow line widths distributed throughout the shocked region of W28. High resolution millimeter (CO, CS and HCO^+) and NIR (H_2 2.12 μm and Fe II fine structure lines) observations of the SNR W28 and W44 reveal extensive shocked molecular gas (Reach, Rho & Jarrett 2005). The NIR observations from both SNRs reveal shocked H_2 emission showing intricate networks of filaments on arcsecond scale, along the bright ridges of the radio continuum shell. The CO $J = 2 - 1$ and the CS $2 - 1$ spectra clearly distinguish between the shocked and pre-shock gas in these SNRs. Reach et al. (2005) concludes that the SNRs W28 and W44 interacts with molecular clouds consisting of a wide range of densities. The different morphologies for these two remnants seen at different wavelengths are explained by the highly nonuniform structure of their respective molecular clouds. The X-ray, Hα and Fe II emission are produced by fast shocks while the H_2 and radio continuum emission are produced by slower shocks into moderate density gas and the CO, CS and HCO^+ emission are produced by even slower shocks into dense cores.

G16.7+0.1 Green et al. (1997) detected a single maser towards the SNR G16.7+0.1 at a velocity of 20 km s^{-1}. Reynoso & Magnum (2000) observed the environments of a number of SNRs in the CO $J = 1 - 0$ transition and found that the G16.7+0.1 SNR is similar to the CTB 37A remnant in being located in a complex region with the CO emission extending over a large velocity range. The observations of Reynoso &

Magnum (2000) allowed them to detect several structures of molecular clouds and more than one site of interaction with the SNR. The maser is superimposed on a CO clump, and lie at the contact region between this clump and the maximum radio continuum emission. This maser and the molecular cloud associated with it does not share the systemic velocity of the SNR. As in the case of W28, that part of the cloud where the maser is located is believed to be accelerated toward the line of sight by the shock, and the masers indicate the velocity of the accelerated gas. The most convincing site for an interaction is suggested by a flat radio continuum rim where the morphology indicates that the expansion is perpendicular to the line-of-sight. However, the single maser in this source is located on the opposite side of the remnant far from the flattened part of the rim. This SNR belongs to a group of SNRs (3C 391, IC 443 and N49) in which the maser emission is displaced from what seems to be the most obvious location for an interaction. It appears that not all transversely shocked dense gas regions lead to the inversion of 1720 MHz OH masers. A possible explanation for the lack of masers in these regions could be the dissociation of OH by high-velocity shocks, but further investigation is required to explain this trend (Reynoso & Magnum 2000).

Kes 69 Green et al. (1997) detected a single 1720 MHz OH maser toward the SNR Kes 69 and found no 1665 or 1667 MHz OH emission around the position of the 1720 MHz maser. It is not clear from the position of this maser whether it is associated with the SNR or the nearby H II region (Green et al. 1997). However, the non-detection of any main-line OH masers (usually associated with H II regions) provides some assurance that the 1720 MHz maser is associated with the SNR. No

follow-up observations have been made.

3C 391 The SNR 3C 391 shows a breakout morphology (Frail et al. 1996) that is thought to occur when a SNR encounters a sudden change in the gas density, as is expected at the edge of a molecular cloud (Tenorio-Tagle, Bodenheimer & Yorke 1985; Arthur & Falle 1991). The radio and X-ray morphologies and the presence of CO (at velocities close to that of the systemic velocity of the SNR) suggests that the SNR is interacting with a molecular cloud (Reynolds & Moffett 1993). Frail et al. (1996) detected two 1720 MHz OH masers toward the SNR 3C 391 as well as extended 1720 MHz OH emission along the north western radio continuum edge. The velocity of the masers agrees well with the H I absorption velocity determined by Radhakrishnan et al. (1972), but is displaced from the velocities of the extended emission. Frail & Mitchell (1998) mapped the ^{12}CO $J = 3 - 2$ line toward the SNR 3C 391 which shows a strong correlation with radio continuum emission. Broadened CO lines, indicative of shocked gas, are seen near the continuum ridges, and narrow lines are seen away from the ridges. The 1720 MHz OH masers are located near, but not coincident with the CO peaks.

Reach & Rho (1999) observed the SNR 3C 391 and its surroundings in the millimeter lines of CO, CS and HCO^+ and detected a giant molecular cloud almost parallel to a ridge of bright radio continuum emission. They found molecular line profiles consisting of a narrow, as well as a very wide component within a small region of the radio continuum shell. The 1720 MHz OH masers are found close to the peak emission in both spectral components. Reach & Rho (1999) argue that the the wide emission lines are from a shock that is only partially dissociative. The 3C 391 SNR is similar to the SNR IC 443 in that

parts of the remnant shell are dominated by ionic shocks and parts are dominated by molecular shocks. The NIR and MIR observations of Reach et al. (2002) have separated the molecular and ionic shocks in the SNR 3C 391. The ionic shocks, traced by [Fe II], [Ne II] and [Ne III], show a filamentary structure and follow the radio continuum shell. Observations show that the ionic shocks and are due to shocks propagating into moderate density gas (of the order $10^2 - 10^3$ cm^{-3}) where the pre-shock material is traced by CO $J = 1 - 0$ emission. The molecular shocks are due to shocks propagating into higher density material and the cooling in such shocks is dominated by H_2 emission. Tracers of the molecular shocks for this SNR include a 1720 MHz OH maser, H_2O and OH FIR emission, and wide CO and CS millimeter lines (Reach et al. 2002).

Kes 78 Koralesky et al. (1998) detected a single maser spot along the eastern edge of the SNR Kes 78 as traced by the radio continuum emission. No 1665 or 1667 MHz OH emission was found at the location of the maser. No follow-up observations have been made.

W44 Early single dish observations (Goss 1968; Goss & Robinson 1968; Turner 1969; Robinson et al. 1970) discovered bright, narrow 1720 MHz OH emission lines toward the SNR W44, together with broad OH absorption features at 1612, 1665 and 1667 MHz. The earliest evidence of the SNR W44 interacting with a molecular cloud came from the ^{12}CO $J = 1 - 0$ and ^{13}CO $J = 1 - 0$ observations of Wootten (1981) who detected an increase in the CO line widths, column density and temperature near the eastern edge of the remnant. Wootten (1981) observed a velocity gradient in the CO lines and interpreted it as being

the result of a massive shell expanding toward the observer. This broad line width and expanding shell was also observed by Slysh et al. (1980) in their observations of the H_2CO absorption. These early measurements by (Wootten 1981) and Seta et al. (1998) showed the likelihood of a C-type shock. DeNoyer (1983) could not find evidence for abundance enhancements of molecular species (e.g. CS, HCN or HCO^+). However, further evidence of the SNR W44 interacting with a molecular cloud came with the detection of [O I] (an important coolant in shocked molecular gas), where the [O I] is brightest along the eastern edge of the SNR and peaks at the location of the 1720 MHz OH masers (Reach & Rho 1996). Maciejewski et al. (1996) summarizes the earlier observations towards the SNR W44 at all wavelengths. Claussen et al. (1997) detected a large number of 1720 MHz OH masers all lying along a line traced by the radio continuum edge. The masers are detected in several regions with the largest concentration of masers located at the interaction site of SNR with the densest part of the molecular cloud (Wootten 1981). These masers show a low spread in maser velocities (typically less than a few km s^{-1}) about a mean velocity that agrees well with the systemic velocity of the SNR (Claussen et al. 1997). Maps made in the ^{12}CO $J = 3-2$ line reveal that the masers are near, but not coincident with, the CO peaks. Broad CO lines, indicative of shocked gas, occur near the radio continuum ridges, and narrow lines are found away from the ridges (Frail & Mitchell 1998). High resolution millimeter (CO, CS and HCO^+) and NIR (H_2 2.12 μm and Fe II fine structure lines) observations by (Reach et al. 2005) reveal extensive shocked molecular gas in the SNRs W28 and W44 as is discussed for the SNR W28 (Reach et al. 2005).

W51C The 1720 MHz OH line was first detected by Frail et al. (1996) towards the SNR W51C, and follow-up interferometric observations established the existence of masers but associated them with the H II region W51B. Koo & Moon (1997a) detected H I gas in an arc-like structure along the radio continuum shell of the SNR which is superimposed on W51B, and Koo & Moon (1997b) detected broad line CO and HCO^+ emission lines coincident with the H I and concluded that the shock is dissociative with the CO reforming behind the shock front. These detections led Green et al. (1997) to reconsider the identification of the detected 1720 MHz OH masers with the H II region. The two masers appear to lie behind the leading edge of the radio continuum emission from the SNR and interior to the H I arc and just above the CO peak emission (Green et al. 1997). The maser velocities are close to that of the systemic velocity (Koo & Moon 1997a) of the SNR and are in good agreement with the velocity of the H I , CO and HCO^+ gaseous arc produced by the shock (Green et al. 1997). Based on the location and the velocity agreement of the masers with the SNR W51C it has been interpreted that the masers originate in the post-shock gas behind the expanding shock of the SNR W51C (Green et al. 1997).

IC 443 Early observations by DeNoyer (1979a) detected 1720 MHz OH emission as bright narrow lines together with broad 1612, 1665 and 1667 MHz OH absorption features toward the SNR IC 443. Since DeNoyer (1979b) first found shock excited line emission from OH, IC 443 has become a rich target of molecular line observations, including H_2, CO, HCO^+, HCN CN, SiO, CS, SO, H_2CO and C_2H (see Chevalier (1999) for a list of references) as well as ionized gas, including X-rays, optical, IR, radio continuum and H I line emission (see van Dishoeck

et al. (1993) for a list of references). Studies of H I and dust carried out by Braun & Strom (1986b) revealed swept-out cavities, shock-heated dust and accelerated H I gas. Claussen et al. (1997) detected six 1720 MHz OH masers toward the SNR IC 443 that show a low spread in maser velocities (typically less than a few km s^{-1}) about a mean velocity that agrees well with the systemic velocity of the SNR. IC 443 belongs to the group of SNRs in which one of the masers seems to be displaced from what seems to be the most obvious location for an interaction (Claussen et al. 1997). The shocked molecular gas is revealed by broad, asymmetric profiles first observed for CO and OH (DeNoyer 1979a). DeNoyer (1979a) also found clear evidence for an interaction of the SNR with molecular gas, based on the disturbed CO emission. The relative intensities of the H_2 $1-0$ $S(1)$ and $1-0$ $S(0)$ and $2-1$ $S(1)$ lines at 2.12μm were measured by Burton et al. (1988) and found to be shock excited. The shocked molecular H_2 gas was observed along the radio continuum ridge defining the interaction (Burton et al. 1988). The ridge of the H_2 emission shows bright spots which are density enhancements in the molecular cloud. The morphology of the H_2 $1-0$ $S(1)$ line emission is similar to that of the millimeter emission from CO, HCO^+, HCN and the 21 cm emission from atomic hydrogen (Braun & Strom 1986b). The distribution of the [O I] 63.18μm fine-structure line emission appears to be similar to the H_2 $1-0$ $S(1)$ line emission, and the peak [O I] line flux occurs at the same position as the H_2 emission peak (Burton et al. 1990). Some evidence exists for shock chemistry processing (i.e. depletions or enhancements of the abundances of various molecules relative to their interstellar values) but not always in accordance with existing shock models (White et al.

1987). The SNR is impacting dense molecular gas on the south which is dominated by H_2 line emission (with a clumped knotty structure) and no detection of atomic lines (Cesarsky et al. 1999), consistent with a pure C-type shock, with a low shock velocity of 30 km s^{-1} and a dense medium with 10^4 cm^{-3}. Lower density material to the northeast shows mostly [Fe II] line emission in the NIR, with strong [O I] and other ionic lines in the MIR and FIR, consistent with a J-type shock with a shock velocity of 100 km s^{-1} and a pre-shock density of the order of 10^2 cm^{-3} (Reach et al. 2002). IC 443 cannot be modelled by a single shock, but rather requires a mixture of both C- and J-type shocks, but at any given place in the remnant only a single type of shock is evident (Burton et al. 1990; Wang & Scoville 1992; Rho et al. 2001).

CTB 33 Frail et al. (1996) detected three 1720 MHz OH masers toward the SNR CTB 33 and one of the masers is coincident with the maximum of the radio continuum emission. Frail et al. (1996) suggested that CTB 33 consists of an unrelated H II region along the line of sight and a SNR located near the maximum in the radio continuum emission. From their observations of ^{12}CO $J = 1 - 0$ and ^{12}CO $J = 2 - 1$, Corbel et al. (1999) found a giant molecular cloud whose velocity is in excellent agreement with one of the masers. The other masers are believed to be associated with the H II region (Sarma et al. 1997; Brogan et al. 2000).

Kes 41 Koralesky et al. (1998) detected a single 1720 MHz OH maser lying toward the distorted radio continuum shell of the SNR Kes 41. No follow-up observations have been made.

G346.6–0.2 Radio continuum emission at 843 MHz shows a clear flattening along the northwestern side of the 346.6–0.2 SNR, indicative of an

interaction of the SNR with the surrounding medium (Dubner et al. 1993). Koralesky et al. (1998) detected five 1720 MHz OH masers along the southern edge of the radio continuum emission with maser velocities within a few km s^{-1} of each other. They detected no 1665 or 1667 MHz OH emission at the position of the 1720 MHz OH masers. No follow-up observations have been made.

CTB 37A The SNR CTB 37A contains two distinct sets of masers which differs both spatially and in velocity (Frail et al. 1996; Brogan et al. 2000). It was proposed by Kassim, Baum & Weiler (1991) that the SNR CTB 37A is in fact two SNRs, designated G348.5+0.1 and G345.5–0.0, overlapping in projection. The ^{12}CO $J = 1 - 0$ observations made by (Reynoso & Magnum 2000) support this interpretation showing two distinct sets of CO clouds that are coincident both spatially and kinematically with the two sets of 1720 MHz OH masers. Frail et al. (1996) detected 1720 MHz OH masers along the radio continuum edge of the SNR CTB 37A and all but two of the masers have velocities close to the upper limits from the H I absorption measurements (Caswell et al. 1975) towards G348.5+0.1 (Frail et al. 1996). The other two masers are at the location where the two remnants overlap and are believed to be associated with the G348.5–0.0 remnant Reynoso & Magnum (2000). Apart from the presence of 1720 MHz OH masers, there are no indications of shocked gas from line broadenings and the there is no correspondence between the CO morphology and this of the radio continuum emission (Reynoso & Magnum 2000). However, a fraction of the CO gas positionally follows some of the masers and extends over the area enclosed by the radio continuum emission.

G349.7+0.2 Frail et al. (1996) detected bright 1720 MHz OH masers along the radio continuum ridge of the SNR G349.7+0.2 and a few weaker masers near the center of the remnant along a radio continuum knot. They noted a small dispersion in the velocities of the masers at different positions in the remnant. The CO observations of Reynoso & Magnum (2000) show that the masers are positionally close to, but not coincident with, the observed ^{12}CO $J = 1-0$ peaks and all the masers are located around the only CO feature detected towards the remnant (see Figure 4.2). The velocities of the masers are in good agreement with the CO velocity with a correlation better than 2 km s^{-1}. The masers, CO emission, shock excited H_2 emission and the maximum OH absorption all overlie one another (Lazendic et al. 2002) as shown in Figure 4.3. The molecular line profiles from observations of ^{12}CO, ^{13}CO, CS and HCO^+ indicate the presence of a C-type shock (Lazendic et al. 2002).

G357.7–0.1 Frail et al. (1996) detected a single 1720 MHz OH maser feature toward the western edge of the Tornado nebula (G357.7–0.1) with a velocity consistent with that of the systemic velocity of the SNR as measured from the 21 cm absorption (Radhakrishnan et al. 1972). Yusef-Zadeh et al. (1999) detected extended 1720 MHz OH emission surrounding the compact maser spot. For large scale maser sources the acceleration is unlikely to be perpendicular throughout a large region of the cloud, resulting in the observed velocity difference between the compact and extended sources. Lazendic et al. (2004) detected 2.12 μm H_2 $1-0$ $S(1)$ line emission which is spatially coincident with the extended 1720 MHz OH emission. The velocity of the maser differs significantly from that of the mean velocity of the H_2 emission and it is suggested that this occurs because masers are only seen at loca-

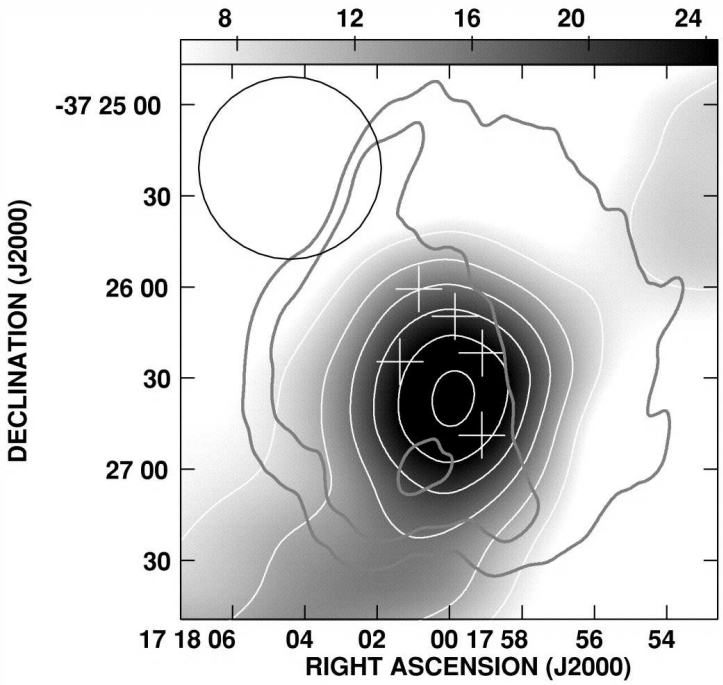

Figure 4.2: SNR G349.7+0.2. CO emission in gray scale and white contours. The crosses represents the positions of the 1720 MHz OH masers. A few radio continuum contours in gray are included to represent the SNR. (From: Reynoso & Magnum (2000))

tions where the shock is propagating perpendicular to the line-of-sight, whereas the H_2 emission is seen from any location within the shocked gas (Lazendic et al. 2004). There is a good correlation between the H_2 and radio continuum maxima and both the H_2 and the radio continuum emission show a filamentary structure (Lazendic et al. 2004). Lazendic et al. (2004) also detected millimeter lines from ^{12}CO and ^{13}CO at the velocity of the maser. The peak in the CO emission aligns well with an indentation seen in the radio continuum emission and the H_2 and 1720 MHz OH maser seen at that location.

G357.7+0.3 The SNR G357.7+0.3 (Square Nebula) has a highly distorted

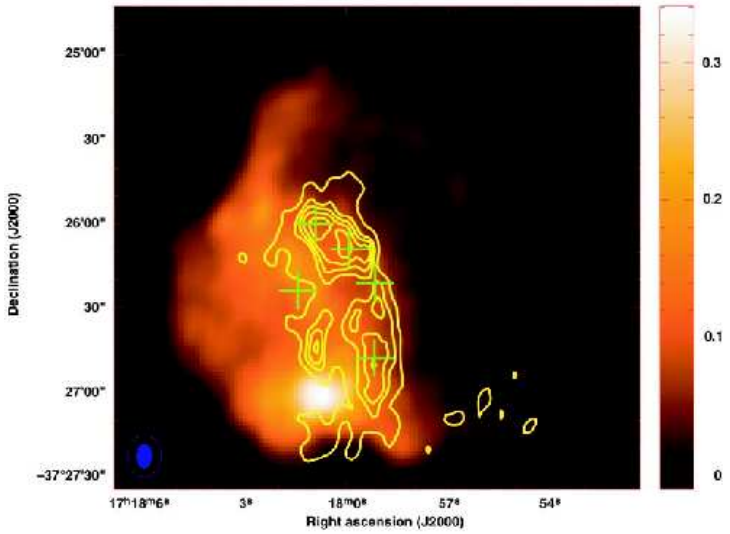

Figure 4.3: SNR G349.7+0.2. OH absorption contours against the 18 cm radio continuum emission (color). Crosses indicate the positions of 1720 MHz OH masers (From: Frail et al. (1996))

appearance with a square-shaped morphology and this may be a signature of the interaction of this SNR with a molecular cloud (Gray 1994; Yusef-Zadeh et al. 1999). Yusef-Zadeh et al. (1999) detected 1720 MHz OH masers as well as extended 1720 MHz OH emission toward the SNR G357.7+0.3. The kinematics and the location of the compact masers and the extended emission suggests that they are located at the boundary between a molecular cloud and the radio continuum shell of the SNR (Yusef-Zadeh et al. 1999). The extended 1720 MHz OH emission surrounds the compact maser spots in the remnant and closely mimics the shape of the radio continuum structure (Yusef-Zadeh et al. 1999). No molecular observations of the surrounding ambient gas have been made.

G359.1–0.5 Yusef-Zadeh et al. (1995) detected 1720 MHz OH masers toward the G359.1–0.5 SNR surrounded by extended, bright 1720 MHz

OH emission. This remnant is a classic example of a SNR where several of the masers lie around the edge of the radio continuum shell (Yusef-Zadeh et al. 1995). The ^{12}CO $J = 1 - 0$ emission appears strongest at the position of the masers, but there is a striking contrast between the velocities of the maser spots and that of the CO emission by more than 50 km s^{-1}. Currently no definitive evidence exists to associate the CO gas with the SNR and Yusef-Zadeh et al. (1999) suggested future observations to search for low velocity molecular gas associated with the SNR as well as a search for 1665 and 1667 MHz OH absorption to confirm the association between the masers and the SNR. Lazendic et al. (2002) detected an elongated bar of H_2 emission aligned with the edge of the remnant. The 1720 MHz OH masers are located near the center of this H_2 emission (Lazendic et al. 2002).

N49 (LMC) Brogan et al. (2004) detected two 1720 MHz OH masers just west of the center of the SNR N49 in the LMC. Several CO observations have shown the presence of molecular gas in the vicinity of the SNR (Cohen et al. 1988; Banas et al. 1997; Mizuno, Yamaguchi, Mizuno, Rubio, Abe, Saito, Onishi, Yonekura, Yamaguchi, Ogawa & Fukui 2001). The velocity of the CO $J = 2 - 1$ emission (Banas et al. 1997) is in reasonable agreement with one of the masers. The detection of faint, diffuse NIR emission (that originates from warm dust and possibly hydrogen recombination lines that has been heated and ionized by the shock) provides further evidence of an interaction (Brogan et al. 2004). The brightest radio continuum emission is coincident with the brightest CO emission and the peak NIR emission, but one of the masers lies well away from the radio continuum, CO emission and NIR peaks (Brogan et al. 2004). N49 is a member of a group of SNRs

(16.7+0.1, 3C 391 and IC 443) where the masers are displaced from what seems to be the most obvious location of an interaction.

4.4.4 Summary

Observations generally show a close agreement in both the position and velocity of the 1720 MHz OH masers and the SNRs in which they occur, as predicted by the model. Most observations show that the difference in maser velocities between maser spots in a particular remnant is small even when they are distributed around a substantial fraction of the shell. Although deviations from the model are observed toward some of these SNRs, in most cases the maser velocities are close to the line-of-sight velocity component of the unshocked cloud complex, and the shock fronts at those locations are traveling perpendicular to the line-of-sight. With few exceptions, the masers are preferentially located near to the edge of the remnant as traced by the radio continuum emission and the peak of the CO emission. The masers are not located at random with respect to the molecular gas but are found near the peaks of the CO $J = 3 - 2$ emission. The masers are close to but not coincident with the CO emission peaks.

The detection of 1720 MHz OH masers towards a selected number of SNRs has been shown to be a powerful probe of the conditions existing in the post-shocked gas of these SNR-molecular cloud interactions. The presence of these masers makes it possible to determine systemic velocities of the SNRs, and in turn, distances and linear sizes for the shells, which is a major contribution to understanding SNR evolution. Green et al. (1997) states that refined theoretical models may in future predict accurate physical parameters in the

post-shock gas directly from the masers. The Zeeman effect has made it possible to measure the magnetic fields associated with these sources. The magnetic field strengths can be used together with molecular data to study the physics of shocks in more detail. SNRs interacting with molecular clouds allow astronomers to study shock physics, and to compare the shocks in SNRs with shocks associated with other astrophysical objects. The next chapter will look in more detail at the shocks associated with the outflows from young protostellar objects. These shocks are compared to the shocks found in SNRs with 1720 MHz OH masers to determine if it is possible that the shocks in star-forming regions have conditions that could support 1720 MHz OH masers.

Chapter 5

Herbig Haro Objects

Because star formation occurs in regions that are deeply embedded within dusty molecular clouds that obscure optical and sometimes even IR observations, the earliest stages of star formation are among the least understood phases in the evolution of stars. In the few instances where they are not heavily obscured the jets ejected from protostars can be seen as nebulous regions where they plow into the surrounding gas. These shock excited regions known as HH objects can be used to study the properties of outflows from newly-formed stars which, in turn, hold essential clues to the birth and early evolution of these protostars.

It has been shown that 1720 MHz OH masers are signposts of C-type shocks in SNRs. The interaction of SNRs with molecular clouds are not the only locations in the Universe where C-type shocks occur. For many HH objects it has been found that the interface formed by the interaction between the outflow and the ambient medium results in the formation of a J-type shock, but on the wings of the shock conditions exist that show signatures of C-type

shocks. Because of the tight constraints under which 1720 MHz OH masers form, the detection of these masers toward HH objects would greatly advance our knowledge of the conditions existing in these objects.

In this chapter I present a review of the literature on the physical and spectroscopic properties of HH objects. Bow shock models of HH objects have been very successful in explaining many of the observed features in these objects. I will explore the results from these models to see if conditions can exist in the C-type shocks of HH objects to support 1720 MHz OH masers.

5.1 Definition and Identification of HH Objects

HH objects are the optical manifestations of the outflow activity of newly-formed stars as ejected material interacts with the ambient medium or with previous ejections. They are nebulous regions of shocked gas and dust with characteristic low-excitation emission lines in the optical spectral range that set them apart from H II regions. The emission lines have been successfully modelled as emission resulting from the recombination of ions and electrons in the cooling gas behind radiative shocks (Schwartz 1978). Burnham (1890, 1894) noted the first example of what is now known as an HH object. The discovery of HH objects was made independently by the American George Herbig (1950, 1951) and the Mexican Guilermo Haro (1952, 1953) towards the Orion nebula. Ambartsumian (1954) subsequently coined the term HH objects for these tiny nebulae. The early development of the field was discussed in a review by Schwartz (1983), and papers presented at the first

symposium devoted to HH objects (e.g. Böhm 1983). One of the key advancements in the study of HH objects was the recognition that some HH objects may take the form of highly collimated jets (e.g. Dopita, Schwartz & Evans 1982; Mundt & Fried 1983). In the latest census about 600 objects are catalogued (Reipurth 1999a), with new objects being discovered regularly.

The spectral lines that are most prominent in HH spectra include Hα λ6563 and the low excitation forbidden lines [O I] $\lambda\lambda 6300, 6363$, [N II] $\lambda\lambda 6548, 6584$ and [S II] $\lambda\lambda 6717, 6731$. The surest way to identify HH objects in star-forming regions is to take a spectrum. However, a simpler technique to search for HH objects is to use CCD imaging with filters selected to transmit the characteristic HH lines (Yan et al. 1998; Zhao, Wang, Yang, Wang, Deng & Chen 1999). An automated scheme to reduce the CCD images taken from large-scale surveys of HH objects has been developed by Deng et al. (2001). A series of surveys for HH objects using this scheme has proved to be efficient and produces results that are uniform and complete. Although it is the characteristic optical emission from HH objects that set them apart from photo-ionized regions, they have now been detected over a wavelength range from the radio to UV regime.

Guidelines have been set up to decide whether or not a specific object should be included in the catalogue of HH objects (Reipurth 1999b). Only those sources in which the outflow extends for more than an arcsecond from the driving source are included in the catalogue. Objects with characteristic HH emission lines but no appreciable extent have been excluded. Many objects have been found to have optical lines as well as strong IR lines from H_2 and [Fe II], with the optical and IR emissions showing similar morphologies. Some objects have been detected only in the IR, but much work needs to be

done on the IR properties of HH flows before these objects can be included in Reipurt's catalogue. In the first edition of the catalogue two objects, HH121 and HH211, were included because they showed strong morphological support for classification as HH flows. Since then, however, no purely IR emitting objects have been included in the catalogue. Kinematically and morphologically shock regions found in association with evolved stars do not appear to differ much from HH objects, but because the shocks appear in highly processed material, spectroscopically they are rather different. HH objects are strictly a star-formation phenomena.

5.2 Physical Properties of HH Flows

5.2.1 Morphology of HH Objects

HH objects have sizes ranging between about 20 and 30 arcseconds, and they are frequently found to occur in pairs or as strings of objects (Reipurth & Bally 2001). Depending on observational sensitivity and intrinsic properties, HH objects can be divided morphologically into either extended, nebulous objects, or point-like, compact objects (Deng et al. 2001). HH objects are associated with outflows from newborn stars, some of which are highly collimated bipolar jets. The most famous images of HH objects show well-collimated jets ending in bright, symmetric bow shocks, but such fine morphologies are limited to only a few cases (Reipurth & Bally 2001). HH47 and HH1 are good examples of sources with a well developed jet-bow shock structure (see Figures 5.1 and 5.2). However, most HH objects have chaotic, non-descriptive morphologies such as that shown in Figure 5.2) (Raga 2005).

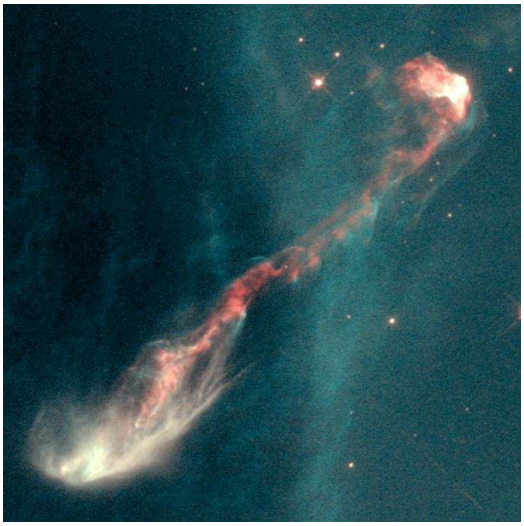

Figure 5.1: A color composite picture of the HH47 bipolar complex as derived from HST WFPC2 images, in which red indicates [S II] emisison and green indicates Hα emission. HH47 is an example of a well collimated jet ending in bright bow shocks. (Credit: J. Morse/STScI, and NASA 1995)

The diverse morphologies displayed by HH objects are the result of several factors: the different environments in which they occur, the chaotic nature of their shocks, differing extinction towards the sources, and the evolutionary stage of the outflow (Reipurth & Bally 2001).

5.2.2 Working Surface

With velocities of 10 – 100 times the ambient sound speed, the jets of HH objects have high Mach numbers, which results in a number of shocks being formed when the jets interact with the surrounding material (Raga 2005). When an HH jet interacts with the surrounding material a two-shock structure is formed called a working surface. The working surface consists of a forward or ambient shock, and a reverse shock or Mach disk. The for-

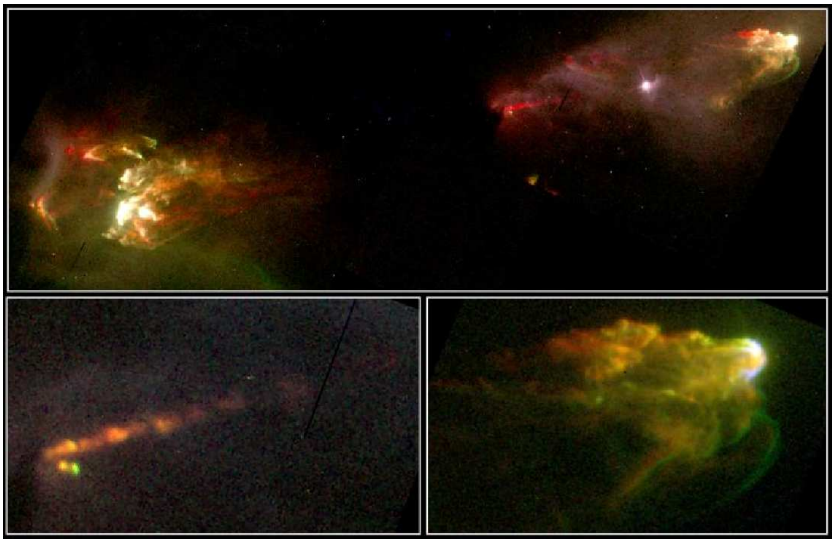

Figure 5.2: Top panel: A color composite picture of the HH1/2 bipolar complex as derived from HST WFPC2 images, in which red indicates [S II] emission and green indicates Hα emission. HH2 is seen at the bottom left of the image and shows a chaotic structure, while the well defined HH1 bow shock is seen at the top right of the image.
Bottom panel: (*Left*) An enlargement of the well-collimated HH1 jet taken from the picture in the top panel; (*Right*) An enlargement of the HH1 bow shock taken from the picture in the top panel. (Credit: J. Hester/STScI, and NASA 1995)

ward shock accelerates the material with which it collides to the propagation speed of the working surface. The reverse shock is induced on the jet by the surrounding material and decelerates the supersonic flow to the speed of the working surface. The most violent interaction occurs at the terminal working surface, where the front of the HH jet slams directly into the undisturbed ambient medium. It has been shown that milder collisions can occur within outflows whose ejection velocity varies with time, such that fast moving material overtakes slower material ejected at an earlier epoch (Raga et al. 1990). The shocked regions of gas formed in these collisions are called internal working surfaces.

5.2.3 HH Jets

In most cases, protostars and the outflows associated with them, are deeply embedded in the clouds from which they were born. When the overlying extinction is low enough to permit optical observations, some HH objects take the form of highly collimated jets, often with two oppositely directed outflow lobes. The HH47 jet, shown in Figure 5.1, is an example of a highly collimated jet with the distinction of having been the first HH jet to be identified (Dopita et al. 1982). Unlike most HH jets that suffer significant extinction near their driving sources, the HH34 jet can be traced all the way to its source (Ray et al. 1996). All jets have knotty substructures; in ground-based images these jets appear as linear or mildly wiggling chains of compact emission knots sometimes connected by fainter emission and ending in many cases in extended bow shaped objects. The HH111 jet shown in Figure 5.3 is a textbook idealization of what a jet should look like (Reipurth et al. 1997, 1999). The HH111 jet has been the subject of extensive observations and studies and has become a popular platform against which theoreticians test their models. The jets of HH1, HH34 and HH111 are very similar to one another in being examples of rather straight, knotty jets that extend radially away from the central star. Only about 10% of known HH objects show such organized structure (Raga 2005). HH objects are variable as was documented by Herbig (1957, 1958, 1968, 1973); on a timescale of years individual knots can systematically brighten or fade, and new knots can appear as shown in Figure 5.4 for the HH111 jet.

In many cases HH jets have been observed to be bipolar, and in some instances quadrupolar outflows are observed. Several explanations have been proposed to explain these four-lobed systems. For example, a binary star

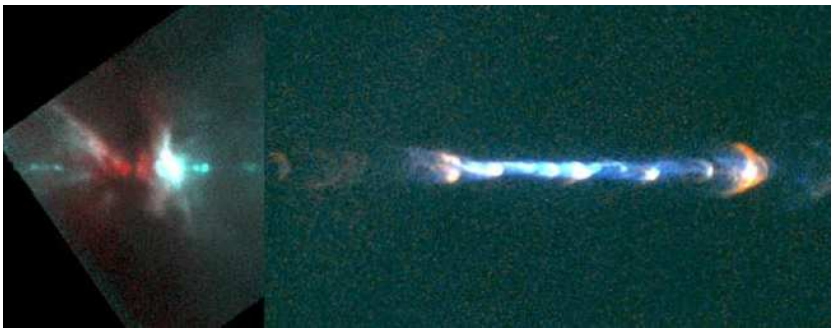

Figure 5.3: A mosaic of optical HST WFPC2 and IR HST NICMOS images of the visible HH111 jet and bow shock, and its highly obscured IR source region. (Credit: B. Reipurth/STScI, and NASA 2000)

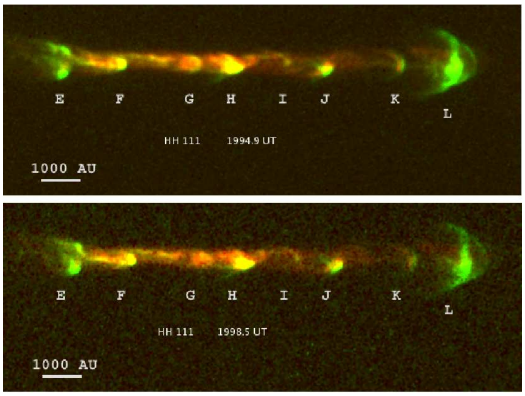

Figure 5.4: HST images of the HH111 jet showing the variability of the knots over a time span of 4 years. (From: Hartigan et al. (2000))

system each driving outflows, or the close superposition in the sky of two independent outflows driven by separate stars (see Rodríguez (1997) and references therein for a list of all the proposed explanations). In some HH objects only the blueshifted lobe is observed; the lobe moving away from the observer is hidden from view as it penetrates deep into the thick, dusty clouds surrounding its protostellar driving source (Raga 2005). In many cases the lobes observed from the same protostar appear to be asymmetrical due to uneven obscuration. However, there are some cases in which the asymme-

tries occur because the jet flows are intrinsically asymmetrical, or because of differences in the ambient medium into which the jets flow (Mundt, Brugel & Bührke 1987; Hirth, Mundt & Solf 1994; Reipurth et al. 1998).

HH jets have opening angles of the order of a few degrees, and length to width ratios that vary from poorly collimated jets with a ratio of 5, to highly collimated jets with ratios exceeding 100. It should be noted, however, that the widths for only a few HH jets are well known; for example, the HH34 jet has a width of 0.7 arcseconds (Raga, Mundt & Ray 1991) and the HH111 jet has a width of 0.8 arcseconds (Reipurth et al. 1997). The knots in jets have typical sizes between 0.6 and 0.8 arcseconds with separations between the knots of several arcseconds (Reipurth et al. 1997).

The electron densities in HH jets can be determined using the [S II] λ6717/λ6731 line flux ratio. Electron densities vary significantly, with $n_e \sim 10$ cm^{-3} for the faintest objects, and $n_e > 10^5$ cm^{-3} for the brightest objects. Values of n_e between a few 100 and a few 1000 cm^{-3} are typical (Reipurth & Bally 2001; Reipurth & Raga 1999). When changing systematically along the jet, the electron density often decreases, which, in the simplest interpretation, suggests diverging flows (Mundt et al. 1987). Ionization fractions range from less than 1% to nearly fully ionized, with typical values around a few percent for most HH objects (Reipurth & Bally 2001). Jets are normally prominent in CCD images obtained through a [S II] filter, and much weaker in images taken through an Hα filter (Reipurth & Raga 1999).

The proper motions of multiple HH objects have been determined (Heathcote & Reipurth 1992; Eislöffel & Mundt 1992, 1994; Eislöffel, Mundt & Böhm 1994). The tangential velocities of the jets are around 100 – 200 km s^{-1} for low-excitation sources, and up to 500 km s^{-1} for high excitation sources (e.g.

HH111 Reipurth, Raga & Heathcote 1992). The tangential velocities tend to decrease with increasing distance from the flow axes. The radial velocities of the jets are measured using long-slit spectroscopy (Meaburn & Dyson 1987; Mundt et al. 1987; Bührke, Mundt & Ray 1988; Reipurth 1989a,b; Mundt et al. 1990; Hartigan, Raymond & Meaburn 1990; Morse et al. 1993; Reipurth et al. 1997) and the bulk radial velocities are typically around 100 – 200 km s^{-1}. Internal velocity dispersions are often seen, but are usually small compared to the bulk flow velocity. When an ordered motion is found, the radial velocity decreases as one moves away from the source. In the case of HH83 a major increase in radial velocity is measured (Reipurth 1989b).

The knotty substructure and low excitation spectra of HH jets introduces a difficult problem: the low excitation spectra characteristic of HH jets indicate shock velocities of at most a few tens of km s^{-1}, which is in contrast to their high space motions of several hundreds of km s^{-1} (Reipurth & Bally 2001). The steady jet models of Falle, Innes & Wilson (1987) were the first simulations of radiative HH jets, and they included concrete predictions of emission line maps. However, with the discovery of proper motions in the knots of many HH jets, this model was replaced by time-dependant models. A number of methods have since been proposed to explain the emission of HH jets, but most of these methods have never been developed to the extent of actually predicting the observational characteristics of these flows (see Reipurth & Raga (1999)), and references therein).

The only models that have been developed in substantial detail so far are the "Internal working surface model" and the "Kelvin Helmholtz instability model". The "Kelvin Helmholtz instability model" associates the knots with Kelvin-Helmholtz (K-H) instabilities in the jet beam boundary. Except for

the work of the Torino group (Micono et al. 1998), who have calculated emission line intensity maps from models of K-H instabilities at the jet beam boundary, all of the HH jet models with predictions of observable quantities are working surface models (see Reipurth & Raga (1999) for a full list of references on the analytical and numerical studies of this model with specific application to HH jets). The internal working surface model interprets the knots as internal working surfaces, indicating that the flow velocity is variable (Raga et al. 1990). This is best understood in terms of episodic activity of the driving source, where fast moving fluid elements interact with slower elements ejected at earlier times. These two models predict different internal structures for the knots but can only be distinguished on high resolution images (such as from Hubble Space Telescope (HST)).

Raga & Noriega-Crespo (1998) used analytical considerations to derive parameters for a multi-mode variability that could explain observed proper motions of the knots in the HH34 jet. Numerical models have been computed from these derived parameters (Raga & Noriega-Crespo 1998). Picking three modes of appropriate periods and amplitudes, one can compute models in which the predicted intensity maps have morphologies and kinematical properties that strongly resemble the knots along the HH 34 jet as shown in Figure 5.5. Raga, Beck & Riera (2004) made detailed comparisons between predicted and observed emission line maps, ratios and profiles from various papers for a number of HH objects (e.g. HH32, HH34, HH110, HH444, HH505, HH777). Their paper is dedicated to models that predict jet structures as a result of a time variability in the outflow velocity of the jet. They conclude that it appears that at least some of the structures in HH jets might indeed correspond to working surfaces. However, they did not explore structures that are not working surfaces, or whether such structures

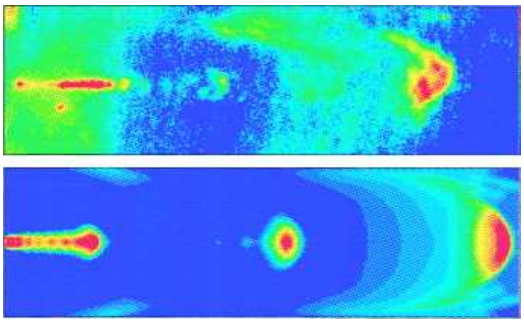

Figure 5.5: Top panel: HST image of the HH34 jet in lines of singly ionized sulfur, [S II] $\lambda\lambda 6717, 6731$. The source of the jet is the compact knot to the left of the image.
Bottom panel: The corresponding intensity map predicted from a numerical model of a jet with variable ejection velocity and three sinusoidal modes of different periods and amplitude (From: Raga & Noriega-Crespo (1998))

are due to K-H instabilities. It appears that the knots in HH jets may also arise due to the time variability in the ejection direction of HH jets, which can cause the jet to impact material that surrounds the jet axis. For example, the knots in the HH34, HH47 and HH111 jets appear to arise from two dominant processes — changes in the velocity and variations in the ejection angle (Reipurth et al. 1997).

Most low mass stars are born in dense clusters that include one or more massive OB star. These stars are sources of intense UV radiation. The jets ejected from low mass protostars that occur in such clusters may be partly or fully ionized by such a radiation field. These jets, called irradiated jets, become visible by the radiation fields of massive OB stars rather than by the shocks within the jet. Several irradiated jets have been discovered so far (Reipurth et al. 1998; Bally, O'Dell & McCaughrean 2000; Bally & Reipurt 2001), for example HH444, HH502, HH503 and HH506. Because their immediate surroundings are destroyed by the nearby OB stars, the extinction is

low and many of the driving sources of these irradiated jets become visible (HH399 (Rosado, Estaban, Leflock, Cernicharo & Garcia 1999) is an exception). Almost all irradiated jets are one sided or nearly one sided. A great advantage offered by irradiated jets is that their physical properties can be determined by methods developed for the analysis of ionized nebula rather than using the less accurate model dependant assumptions made about the nature of the shocks (Bally & Reipurt 2002).

5.2.4 Timescales and Sizes of Outflows

Giant HH Flows

Because of the field size of the first generation of CCD detectors, the dimensions of all HH jets have been assumed to be around a few arcminutes, corresponding to lengths of about 0.3 pc. Bally & Devine (1994) observed the HH34 complex with a new wide field CCD imager, which revealed faint emission features connecting the HH34 complex with other flows, previously believed to be independent (Reipurth 1989b). The entire HH34 giant flow has a projected length of 2.8 pc and the system contains HH34, HH40, HH34N, HH85, HH86, HH87, HH126 and HH173 all lying along a single well-defined axis. A systematic survey for giant flows was conducted after this initial discovery, resulting in the identification of several such giant HH flows, some of which are over 12 pc long (Reipurth 1989b; Ogura 1995; Reipurth, Bally & Devine 1997; Reipurth, Devine & Bally 1998). Many well known HH jets (such as HH1/2 and HH111) form only a part of such giant flows. The HH1/2 jets were believed to have a total length of only 0.4 pc until the discovery of HH401 and HH402, which are two large, bow-shaped emission

nebulae symmetrically located around the HH1/2 flow forming a giant flow with a projected length of 5.9 pc (Ogura 1995). HH111, HH113 and HH311 are the three major components of a 7.7 pc long giant flow (Reipurth et al. 1997). Dynamical ages for the outer most components of these giant flows range from 10^4 to 10^5 years, which is about an order of magnitude larger than was previously estimated. Since the longer timescales are comparable to the timescales of accretion and mass loss of protostars, giant HH flows can provide fossil records of the evolution and outflow activity of protostars (Reipurth & Bally 2001).

Almost all giant HH flows with well developed jets have multiple working surfaces along their outflow axes. From currently available data it appears that the physical sizes of the knots increase and the knots adopt increasingly chaotic shapes with increasing distance from the source (e.g. HH1/2, HH34 and HH111), while the proper motions and radial velocities systematically decrease (Reipurth et al. 1997). The knot separation also increases with increasing distance from the source. If they lie within 0.1 pc of their source, the internal working surfaces of individual cooling zones can overlap one another to form a nearly continuous jet, whereas the gaps between the outer most shocks can become as large as $\sim$ 10 arcminutes. The increasing gap size with distance from the source implies that large variations in the outflow speed occur over time intervals of centuries to millenia, while small velocity variations occur over years to decades (Bally & Reipurt 2002). Because of their large sizes, many giant HH flows break out of the clouds in which they originate and into the surrounding ISM (Reipurth et al. 1997). Many giant HH flows do not have a linear structure. The S-shaped point symmetry of the flow found in HH315 (Reipurth et al. 1997) for example could be caused by precessing or wandering of the outflow axis. HH 366 has a C-shaped

symmetry (Bally, Devine & Alten 1996), indicating either flow deflection by a wind, or motion of the source through the surrounding cloud.

When stars are born in dense clusters it can be difficult to associate individual HH objects with a specific source. Although most giant HH flows are found in isolated star-forming regions, there are cases where multiple outflows overlap in the plane of the sky, creating a lot of confusion. It is for this reason that many HH objects have not been linked to specific flows or sources (e.g. NGC1333 Bally, Devine & Reipurt (1996); L1448 and L1455 Bally et al. (1997)).

Microjets

Some T Tauri stars show high-velocity forbidden emission lines characteristic of HH objects. These lines are often blueshifted, indicative of a bipolar outflow whose receding lobe is obscured (Edwards et al. 1994; Hartigan, Edwards & Ghandour 1995). Long-slit spectroscopy of these T Tauri stars shows HH flows of just a few arcseconds in length (Solf 1997). These small HH flows are called microjets. HH158 is an example of a well-observed microjet ejected from the visible T Tauri star DG Tau. The jet contains several small knots and can be traced out to a distance of about 1.5 pc from its source (Mundt et al. 1987).

5.2.5 Driving Sources

The protostellar driving sources of HH flows can have so little extinction along the line of sight that they are optically detected (Reipurth & Bally

2001, e.g. T Tau, DG Tau, HL Tau,). However, in most cases these driving sources are deeply embedded in large amounts of circumstellar material and emit almost all their flux at FIR wavelengths (Cohen & Schwartz 1987). While less obscured sources can emit large portions of their luminosity at NIR wavelengths (Molinari, Liseau & Lorenzetti 1993), some sources are so deeply embedded that they are not even directly detected in the IR. The luminosity of the protostar is the one value that can be estimated for all HH sources detected in the optical or IR. Studies from the two largest collections of HH source luminosities found that the distribution of these luminosities is a broad-peaked function with a median value around 11 $L_{\odot}$ (Cohen 1990; Reipurth, Chini, Krügel, Kreysa & Sievers 1993).

Low-mass protostellar evolution is classified into Class 0, I, II and III phases (Bachiller 1996). The most powerful outflows from protostars occur during the Class 0 phase, but most of these outflows are too obscured to produce spectacular HH objects (e.g. HH211 McCaugrean, Rayner & Zinnecker (1994) and HH212 Zinnecker, McCaugrean & Rayner (1998)). By the time protostellar sources enter the Class II phase of evolution, the accretion and outflow activity have declined. By then, many of the oldest ejecta have already punched out of their parent cores into regions of low obscuration. Therefore, it is during this phase that the most spectacular HH objects can be seen (Bally & Reipurt 2002). Accretion and outflow activity decrease even more during the Class II and III T Tauri phases of protostellar evolution. There is growing evidence that outflow activity and the production of HH objects can carry on for some time. The timescales involved, luminosities and amount of accretion during each phase of protostellar evolution are listed in Table 5.1.

It is tempting to think that the invisible, deeply embedded protostellar

Class	Timescale (yr)	L_{mech}/L_{bol}[a]	Accretion, M ($M_\odot$ yr^{-1})
0	$\sim 10^4$	can exceed 0.1	can exceed 10^{-5}
I	$\sim 10^5$	< 0.001 - 0.01	$\sim 10^{-7}$
II and III[b]	–	several 10^6	$\sim 10^{-9}$

[a]The mechanical luminosity of the outflow divided by the bolometric luminosity of the source

[b]It should be noted that the values given for these phases only represent the levels at which outflows and HH production persist in some objects.

Table 5.1: Properties during the phases of protostellar evolution

sources correspond to an early evolutionary stage and the optically visible protostars to a later stage in the evolution of the young star. It is also often assumed that microjets represent the final stage of protostellar evolution because of their small size and association with visible T Tauri stars. However, because the visibility of a protostar depends on the nature of its surroundings and possibly also on the orientation of the system with respect to the plane of the sky, such an evolutionary sequence is not credible. Due to the episodic nature of HH flows, it is difficult to use them as an indicator of the evolutionary stage of the driving source (Reipurth & Bally 2001).

In those cases where both lobes of an HH flow are observable, the distribution of the knots are often symmetric. This indicates that the activity of the driving source is the dominant factor in the production of the knots, as opposed to the interaction of the outflow with the surrounding medium (Gredel & Reipurth 1994; Zinnecker et al. 1998). Such remarkable symmetry is often also displayed between large bow shocks of many bipolar outflows, such as HH47, HH34 and HH355 (Graham & Elias 1983; Bührke et al. 1988; Reipurth et al. 1997). It is such considerations that led to the suggestion that these large bow shocks are associated with FU Orionis (FUor) eruptions (Dopita 1978; Reipurth 1989a).

FUor eruptions have been successfully modelled as accretion events in circumstellar disks (see Reipurth & Bally (2001) and references therein for a detailed description of the properties and origin of FUors). The chances of identifying FUors increases with increasing source luminosity (Reipurth & Aspin 1997). From statistical arguments it appears that FUors are repetitive events (Herbig 1977; Hartmann & Kenyon 1985). The frequency of FUor outbursts are not well known, but it appears that they decay from a high accretion state to a low accretion stage on a timescale of roughly a century. The typical time intervals between the appearance of large bow shocks in HH flows is of the order of 500 – 1000 years, which implies that at any given time an HH source is more likely to be in a low accreting T Tauri stage, and that giant working surfaces may be emitted only during a certain phase of protostellar evolution. Most HH sources for which optical and/or IR spectra are available are indeed T Tauri stars. Reipurth (2000) found that a large number of giant HH flow sources are binary or higher multiple sources, and suggests a link between giant flows and multiplicity.

Although most HH flows are ejected from low-mass protostars, a few outflows from high-mass protostars have been found (e.g. Axon & Taylor 1984; Reipurth & Graham 1988; Poetzel, Mundt & Ray 1992; Ogura & Walsh 1992). In most cases high-mass protostars produce relatively poorly collimated outflows as compared with low-mass protostars (Reipurth & Bally 2001). HH80/81 is an example of a high-mass star ejecting highly collimated bipolar jets (Martí, Rodríguez & Reipurth 1995). The spatial extents, masses and luminosities of outflows scale roughly with source luminosity, but there is no clear dependence of flow speed on source luminosity (Reipurth & Bally 2001). In the case of HH80/81 the outflow appears to be similar to those from low-mass protostars, apart from being much larger and, in this particu-

lar case, also much faster. HH80/81 are the intrinsically brightest known HH objects. It should be noted that the mechanisms responsible for the ejection and collimation of outflows from high-luminosity stars may differ from those in low-luminosity stars (Reipurth & Bally 2001, and references therein). HH flows have also been found to be associated with a few intermediate-mass Herbig Ae/Be stars such as MWC 1080 (Poetzel et al. 1992).

5.3 HH Objects at Different Wavelengths

HH objects are the optical manifestations of outflows from protostars. Apart from the extensive optical observations of these outflows, they have also been observed in other wavelength regimes, ranging from radio to the UV. Other manifestations of outflows from protostars include shock-excited H_2 and [Fe II] line emission, outflow lobes detected in the millimeter-wavelength transitions of molecules such as CO, radio continuum jets, and masers.

5.3.1 Optical Spectra

In HH objects the allowed and forbidden emission from neutral atoms such as [O I], O I , [C I] and [N I], and the emission from ions of low ionization energy such as Ca II , [Ca II], [Fe II], Mg II and [S II], are much stronger than observed in H II regions. Even though HH objects are identified by their characteristic optical emission lines, the line ratios can vary significantly from one object to the next. HH objects have subsequently been classified according to their level of excitation into high-, intermediate- and low-excitation objects (Böhm 1983; Raga, Böhm & Cantó 1996). HH1 is a prototypical high-excitation

object (Brugel, Böhm & Mannery 1981a; Solf, Böhm & Raga 1988), and HH7 is a prototypical low-excitation object (Böhm, Brugel & Mannery 1980; Böhm, Brugel & Olmsted 1983). The line ratios of most HH objects lie within the limits given for these two objects. Because HH objects often suffer from high extinction, the interpretation of these line ratios depend on a proper correction for reddening (see Solf et al. (1988) for a discussion of de-reddening methods). HH objects are primarily emission line sources, but they do also have very weak continua (Böhm, Schwartz & Siegmund 1974; Brugel, Böhm & Mannery 1981b; Solf et al. 1988; Hartigan et al. 1999). A few HH objects show a red continuum as a result of the reflected light from the protostar, but the majority of continua are blue and rise in the UV. Collisionally enhanced two-photon decay in neutral atomic hydrogen can usually account for the observed blue continuum (Dopita, Binette & Schwartz 1982). Both the emission line and the continuum spectra have been modeled with reasonable success in terms of the excitation produced by the passage of shocks through the gas with velocities ranging from 20 – 200 km s^{-1} (with the lower velocities corresponding to low excitation objects and the higher velocities to high excitation objects) (Raga 2005).

5.3.2 UV Observations

UV observations of HH objects have produced detections in both emission lines and continua (Ortolani & D'Odorico 1980; Böhm, Böhm-Vitense & Brugel 1981). In the case of high-excitation objects, more energy may be emitted in the UV than in the optical (mainly through the lines of [C IV] $\lambda\lambda 1548, 1551$ and [C III] $\lambda\lambda 1907, 1909$) (e.g. Böhm et al. 1987)). It is believed that enhanced two-photon decay can also account for the UV continua in

HH objects, and at the shortest wavelengths fluorescent H_2 emission may contribute (Böhm et al. 1987).

5.3.3 IR and Millimeter Wavelength Tracers

NIR observations of HH objects show that most of the spectra are dominated by emission lines from the low-lying vibrational levels in the electronic ground-state of H_2. The strongest line of H_2 is the $1-0$ $S(1)$ line at 2.122 μm which was first detected by Beckwith et al. (1978). Bright H_2 emission has been observed from bow shocks at terminal working surfaces, at the internal working surfaces in outflows, and as fainter emission along the outflow (Eislöffel 1997). Low-excitation HH objects tend to be brighter in these NIR lines (Wilking et al. 1990); see, for example, HH91, HH43 and HH205 – 210 (Gredel & Reipurth 1994; Schwartz et al. 1988; Allen & Burton 1993). However, this is not always the case, mainly because many HH objects have broken out of their parent molecular clouds into the ISM and can then move through material that is mostly atomic. The HH 34 jet is an example of an extremely low-excitation object that emits hardly any H_2 (e.g. Stanke, McCaughrean & Zinnecker 1998). It is now widely recognized, as originally discussed by Elias (1980), that the NIR emission lines of H_2 are collisionally excited in slow non-dissociative shocks, and are the main cooling mechanism when HH jets move through molecular material (Gredel 1994; Smith, Khanzadyan & Davis 2003). HH objects also emit several strong emission lines of [Fe II] in the NIR wavelength region (e.g. Gredel 1994). The [Fe II] NIR emission is believed to arise in fast, dissociative shocks (e.g. Gredel 1994; Smith et al. 2003). Therefore, codes for modelling shocks should take into account both atomic and molecular processes.

The study of outflows from protostars initially started with observations of CO (e.g. Bally & Lada 1983; Lada 1985; Bachiller 1996). These molecular outflows are generally seen in the millimeter-wavelength transitions of CO. Only about 30% of outflows from protostars show both HH outflows and molecular outflows, which may be due largely to the fact that the optically detected HH flows are visible from nearby protostars in regions of low obscuration (Reipurth & Bally 2001). The distribution of the molecular emission is similar to that of the associated HH flows in having two lobes, one blueshifted and one redshifted. The mean velocity of a molecular outflow is in general lower than that of the associated HH flow (Raga 2005). Molecular outflow lobes can be classified roughly into the "classical" (first detected) low-velocity CO lobes with $v < 30$ km s^{-1} (Bally & Lada 1983; Lada 1985), and the extremely high-velocity CO components with $v \approx 100$ km s^{-1} (Lizano, Heiles, Rodríguez, Koo, Shu, Hasegawa, Hayashi & Mirabel 1988; Koo 1989).

The classical CO lobes tend to be poorly collimated and frequently exhibit shell-like or limb-brightened morphologies. They dominate the CO emission associated with more mature outflows. The high-velocity components have dynamical properties and morphologies which are very similar to the ones of HH jets. They are highly collimated and often peak in well-defined clumps that tend to be equally spaced along the flow axis. These clumps coincide with HH objects and with the H_2 vibrational emission knots. The low velocity CO components appear to be more prominent near these clumps (André et al. 1990; Bachiller et al. 1990; Bachiller, Martin-Pintado & Fuente 1991; Bachiller & Cernicharo 1991; Richer, Hills & Padman 1992). Figure 5.6 shows the high velocity and low velocity CO outflow lobes associated with HH211. IR observations show that the lobes terminate in molecular hydrogen shocks.

The optical emission lines and the NIR lines of H_2 require temperatures of at least several thousand degrees to excite them, and hence this emission traces the regions where shocks are currently taking place. On the other hand, the millimeter-wavelength transitions of CO are excited in cool gas at temperatures of only a few Kelvins at the densities typically found in molecular clouds or outflow lobes (Eislöffel 1997). In most cases, the CO emission peaks just upstream of the bright H_2 knots (Eislöffel 1997). These observations suggest a "unified model" in which the CO flows consists of ambient gas that has been entrained by the highly-collimated HH jets (Rodríguez 1989). Molecular outflows consist mainly of swept-up ambient material (Arce & Goodmann 2002), although the molecular emission might be indicating that the gas associated with the HH flow is at least partially molecular (Bachiller 1996).

Giant HH flows have also been observed at IR- and millimeter wavelengths (some giant HH flows were first recognized by their CO emission). High velocity CO emission is associated with most giant HH flows (Bence, Richer & Padman 1996), and the NIR lines of H_2 are often used to trace obscured parts of giant flows (Stanke et al. 1998). In most giant HH flows the optical emission is an order of magnitude larger than the CO outflow, as can be seen in HH1/2, HH34 and HH111 (Chernin & Masson 1995; Cernicharo & Reipurth 1996), but in a few cases, for example HH366 (Yu, Billawala & Bally 1999), the CO emission extends beyond the optical emission. The extent of the CO lobes depend on whether the ambient medium through which the flow moves is mainly molecular. Observations of giant HH flows provide support for the "unified model" in which the bipolar jets from protostars power the lower velocity lobes traced by CO emission (Arce & Hector 2002).

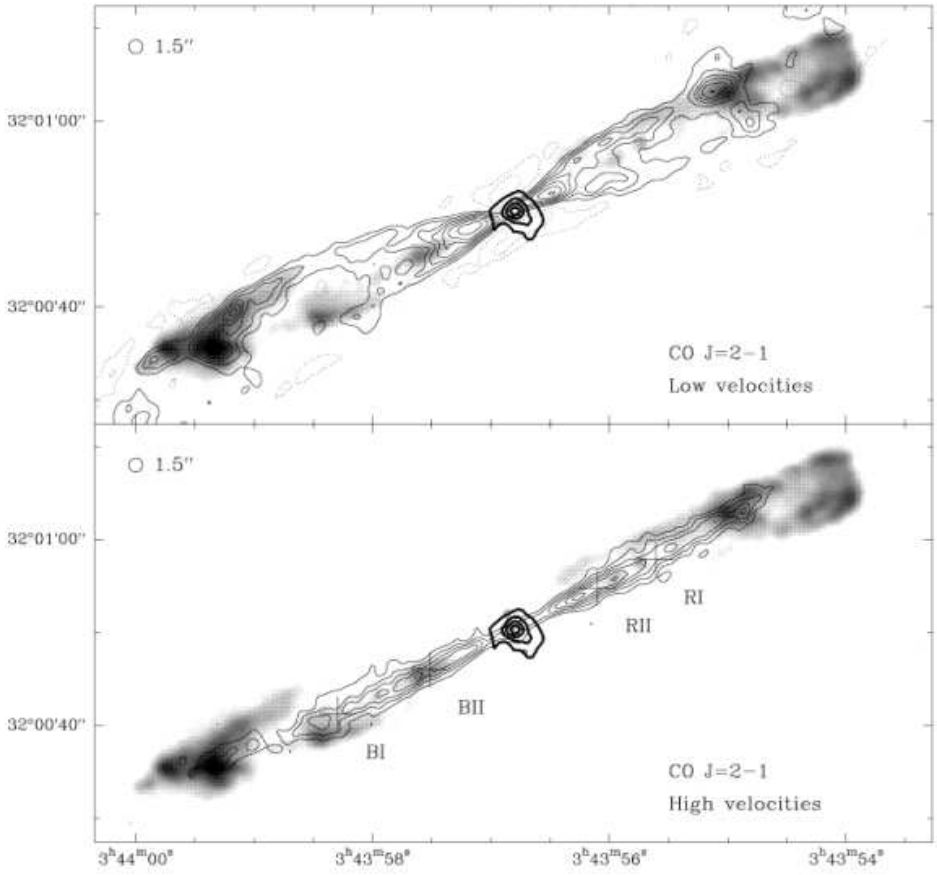

Figure 5.6: CO high- and low-velocity outflows surrounding the HH211 jet. The CO $J = 2 - 1$ outflow lobes (thin contours) and the 230 GHz continuum emission surrounding the driving source (thick contours) superimposed on the H_2 $1 - 0$ $S(1)$ emission (grey scale) (From: Gueth & Guilloteau (1999))

5.3.4 Thermal Radio Jets, X-rays and Masers

Centimeter radio continuum emission has been detected in only a few HH objects (Pravdo et al. 1985; Rodríguez & Reipurth 1989; Yusef-Zadeh 1990; Anglada et al. 1992). However, high angular resolution observations of bright HH sources (such as HH1 and HH111) have revealed the presence of small and weak collimated radio jets elongated along the outflow axis of the HH

jets (Rodríguez, Ho, Torrelles, Curiel & Cantó 1990; Rodríguez & Reipurth 1994; Anglada 1996; Rodríguez 1997; Rodriguez et al. 2000). The emission produced by these radio jets is due to free-free radiation from the (partially) ionized outflows, and therefore they are known as thermal radio jets.

The first X-ray detections of HH objects came from the relatively recent Chandra observations of HH 2 (Pravdo et al. 1985), and the XMM-Newton observations of HH154 (Favato et al. 2002). The presence of X-rays in HH objects opens up the possibility of detecting fast, non-radiative shocks that have not been detected before and that could be associated with the outflows.

H_2O masers can arise in the shocked gas associated with the outflows from protostars and therefore they can provide important information about these outflows. The HH212 jet is an example of an outflow that shows a number of H_2O masers lying along the jet axis (Claussen et al. 1998).

5.4 Modelling of HH Shocks

This section gives a brief overview of the mechanisms and models developed over the years to explain the observed emission lines of HH objects. Jet-driven bow shocks have been extremely successful in explaining the optical properties of HH flows. At present, bow shocks also appear to be the most popular mechanism for the modelling of molecular shocks. One of the main aims of this section is to show that these bow shocks have C-type characteristics over at least part of their extent. As discussed earlier, C-type shocks are a necessary requirement for the production of 1720 MHz OH masers in SNRs.

5.4.1 Development of HH Shock Models

Currently, the observed line spectra of HH objects are interpreted as being due to the excitation of gas by passing shock waves. A range of mechanisms have been proposed to explain the shock waves responsible for the optical emission of HH objects: The "Shocked Cloudlet" scenario has a wind from the protostar impacting on and shocking a denser cloud in the ambient medium (Schwartz 1978); the "Interstellar Bullet" scenario interprets HH objects as fast moving, dense cloudlets that plow through a more or less stationary ambient medium (Norman & Silk 1979); the "spherical explosion" model (Böhm 1978), and the "cavity/ wind focusing" scenario (Cantó 1980; Köngl 1982) have an expanding wind interacting with the walls of the cavity produced by the wind. The more recent models are based on the "Jet/Working Surface" scenario in which HH emission is a result of the shock produced at the head, or working surface, of a collimated, high velocity jet (Dopita et al. 1982). Many, but not all, HH objects appear to be modelled best as jets.

After the initial models of Schwartz (1978), plane parallel shock wave models were developed to predict the flux ratios of lines emitted by HH objects. These include the predictions of the atomic and ionic line fluxes from stationary shock models (Dopita 1978; Raymond 1979; Shull & McKee 1979; Dopita et al. 1982; Binette, Dopita & Tuohy 1985; Hartigan, Raymond & Hartmann 1987; Hartigan, Morse & Raymond 1994, 1995) and from time-dependant shock models (Innes, Giddings & Falle 1987a,b,c; Gaetz, Edgar & Chevalier 1988; Gaetz 1990). The radio free-free continuum of such shocks was modelled by Curiel, Cantó & Rodríguez (1987); Ghavamian & Hartigan (1998).

Plane parallel shock models cannot simultaneously explain the presence of low excitation lines such as [O I] and [S II], and highly ionized species such as [O III] and [C IV] that have been observed in HH objects. The "Shocked Cloudlet", "Interstellar Bullet" and the "Jet/Working surface" models all predict that at least part of the emission is formed in a bow shock. A bow shock produces a range of velocities, as only the component of the flow velocity perpendicular to the bow shock is thermalized (see § 5.4.2); high velocities at the apex of the bow produce high excitation lines while lower excitation lines are produced as the velocity decreases along the bow wings where the shocks become more oblique. The first bow shock models ("1.5 Dimensional Bow Shock") were composed of the superposition of oblique plane shocks (Hartmann & Raymond 1984). Excellent fits between the spectra and the predicted emission line ratios, line profiles, spatially resolved line profiles and narrow-band images have been achieved for many flows (Choe, Böhm & Solf 1985; Raga & Böhm 1985, 1986; Raga 1986; Raga, Böhm & Solf 1986; Hartigan et al. 1987; Hartmann, Raymond & Meaburn 1990; Noriega-Crespo, Böhm & Raga 1989, 1990; Morse et al. 1994; Indebetouw & Noriega-Crespo 1995).

However, it was realized several years ago, that the "1.5 Dimensional Bow Shock" models are not sufficient to model spatially resolved observations from HST of HH objects (Raga & Binette 1991). The "1.5 Dimensional Bow Shock" models were followed by two-dimensional axisymmetric bow shock models (Raga & Böhm 1987; Raga et al. 1986; Raga, Mellema & Lundqvist 1997; Cantó & Raga 1998), two-dimensional asymmetric bow shock models (Henney 1996), and hydrodynamic simulations of complete working surfaces consisting of the bow shock and the Mach disk of jets (Blondin, Königl & Fryxell 1989; Stone & Norman 1993; de Gouveia dal Pino & Benz 1993;

Raga 1995). The modelling of internal shocks (knots) along the jet beam were discussed in § 5.2.2. Unlike the earlier models, many of the more recent numerical simulations refer to completely theoretical problems (instabilities in the jet/beam environment, the effect of time variabilities of the ejection, the importance of magnetic fields) and they are not directly orientated to obtain concrete predictions of the observational characteristics of HH objects.

Several models have been proposed to explain the mechanism by which ambient gas is entrained and accelerated to produce molecular outflows. The most popular entrainment models can be separated into three broad classes, namely: the wide-angled-wind model (e.g. Matzner & Mckee 1999; Lee et al. 2001); the turbulent jet entrainment model (e.g. Cantó & Raga 1991; Stahler 1994; Lizano & Giovanardi 1995); and the jet-driven bow shock model. Currently, bow shocks are the most popular mechanism for modelling molecular shocks (e.g. Raga & Cabrit 1993; Masson & Chernin 1993; Zhang & Zheng 1997; Smith, Suttner & Yorke 1997; Lee et al. 2001) and efforts have been made to simulate jet bow shocks with conditions more appropriate for molecular outflows. J-type (jump) and C-type (continuous) molecular shocks (Draine 1980) have been used to explain the IR line spectra of HH objects (Hollenbach 1997). The H_2 emission occurs mainly in the low velocity wings of bow shocks where models indicate C-type shocks are responsible for the emission and acceleration of H_2 (e.g. Fernandes 2000; Froebrich, Smith & Eislöffel 2003; Smith et al. 2003; McCoey et al. 2004; O'Connell et al. 2005). J-type shocks have been shown to dissociate H_2 molecules at speeds greater than 24 km s^{-1} (Kwan 1977), although in a few cases the observed H_2 emission has been modelled successfully by slow, non-dissociative J-type shocks (Gredel 1994; O'Connell et al. 2004). The high excitation NIR emission of [Fe II] is usually located near the apex of the bow where the maximum com-

ponent of the velocity normal to the shock front occurs. The NIR [Fe II] emission can be best modelled by fast (40 – 60 km s^{-1}), dissociative J-type shocks (Khanzadyan et al. 2004). The rotational lines of OH, SiO and CO, and the fine-structure lines of [O I], [S III], [Ne II] and [S I] can also be excited by fast, dissociative J-type shocks (e.g. Hollenbach 1997; Haas, Hollenbach & Erickson 1991).

5.4.2 Bow Shocks

The working surface of an outflow consists of an ambient/forward shock and a reverse shock or Mach disk (see § 5.2.2). The forward shock often takes the form of a bow-shaped structure pointing away from the protostar. Figure 5.7 shows a 2-dimensional schematic of the structure of a bow shock. Between the forward and the reverse shock is a shell or layer of dense gas. This high pressure gas is ejected sideways out of the jet beam and forms another working surface as it interacts with the undisturbed ambient medium. The ejected gas interacts with the ambient medium through a broader shock surface that surrounds the head of the jet in a shell-like envelope that forms the bow wings. A straight forward prediction of bow shock models is that the strongest shock is experienced at the apex of the bow where the shock is normal, and weakens as one moves away from the narrow apex to the broader wings where the surface becomes more oblique and the net forward velocity decreases. This scenario leads to a range of excitation conditions that are indeed observed in the most symmetric bow shocks where high excitation lines dominate around the apex and lower excitation lines are strong along the wings. The shock speed v_s is determined locally as the component of the bow speed transverse to the surface element, i.e. $v_s = v_\perp = v_{bow} \sin \alpha$.

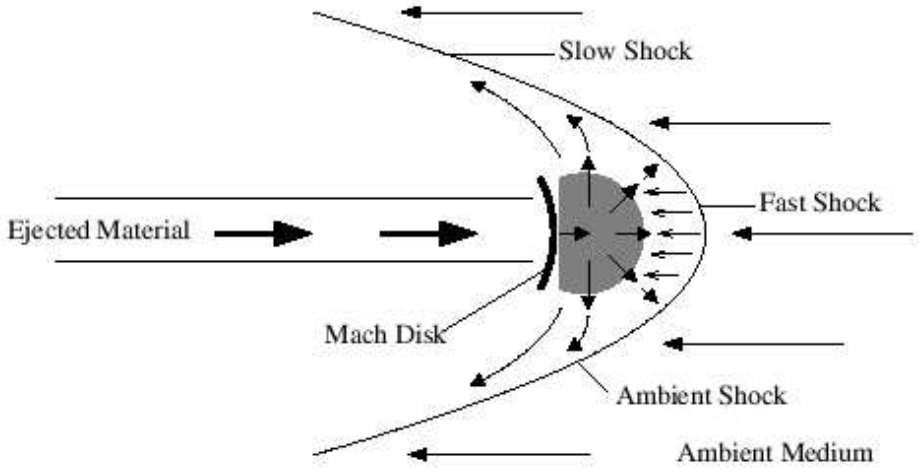

Figure 5.7: Schematic of the structure of a bow shock. In the rest frame of the bow shock, high speed material entering from the left is decelerated at the Mach disk. The ambient medium is decelerated and forms a second shock front at the leading cap. Between these two shocks material is compressed and ejected sideways, shocking the ambient gas to form bow wings (From: O'Connell (2005))

HH 34 resembles best the ideal bow shock, and most of the internal working surfaces in the HH 34 jet also have bow shapes extending across the entire width of the jet (Reipurth et al. 1997).

5.4.3 The CBOW Model and the HH 7 Bow Shock

HH7–11 is an extensively investigated HH outflow, with the low-excitation object HH7 forming the leading working surface of the jet. HH7 is an example of a bow shock where the observed emission in the wings can be explained by a non-dissociative C-type shock. Smith et al. (2003) revised the CBOW model (Smith & Brand 1990; Smith, Brand & Moorhouse 1991; Smith 1991a) for magnetohydrodynamic bow shocks to interpret various observational data

sets (e.g. Smith 1991b; Davis & Smith 1996; Eislöffel et al. 1996; Froebrich, Smith & Eislöffel 2002; Smith et al. 2003) of HH7. The CBOW model describes a bow shock with a paraboloidal geometry and is split into two regions: the J-type cap, described by a dissociative, strong J-type shock (responsible for the atomic emission); the H_2 emitting tail described by a C-type shock. The dissociation speed, v_{diss}, is the shock speed along the bow at which the transition from a C-type shock to a dissociative J-type shock occurs. For the CBOW model the shock speed exceeds the dissociation speed, thus creating a J-type cap. Steady state equations are applied and each element of the bow surface is treated as a distinct planar shock wave.

The main features of the observed spatial distribution of the $1-0$ $S(1)$ and the $2-1$ $S(1)$ emission lines of H_2 can be reproduced by the CBOW model in which the bow shock is a paraboloid (shape (s) = 2) inclined at 30° to the line of sight with a shock speed of $v_s = 55$ km s^{-1}. The model requires a pre-shock density of 8×10^3 cm^{-3} with an H_2/H number ratio of 0.25 and a magnetic field $B = 0.97 \times 10^{-4}$ G, giving an Alvén speed of 2 km s^{-1}. Figure 5.8 displays the observed emission from the H_2 $1-0$ $S(1)$ and $2-1$ $S(1)$ transitions as well as the the $2-1S(1)$ image from Smith et al. (2003) from the best fit of their CBOW model. The H_2 emission arises from the bow wings and shows a similar distribution in the $1-0$ $S(1)$ and $2-1$ $S(1)$ transitions. The model provides a good fit but it was expected that the $2-1$ $S(1)$ emission would be located nearer to the apex where the hotter gas is present. However, these distributions only appear similar as a result of the projection of the jet (the small angle to the line of sight). Because the axis where the molecules are dissociated (in the J-type cap) lie projected onto the bow, this projection of the jet explains the observed hole in the H_2 emission.

A J-type model, JBOW (Smith 1994), was also revised by Smith et al. (2003) to interpret the observed H_2 emission lines in HH7. In the case of the JBOW model the observed H_2 emission in the bow wings is described by slow non-dissociative J-type shocks. Smith et al. (2003) were unable to find a JBOW model fully consistent with the observed HH7 bow, which suggests that a C-type and not a J-type shock best describe the H_2 emission.

The observed $\lambda 1.644 \mu$m line of [Fe II] (see Figure 5.9) shows a very different spatial distribution than that of the H_2 emission in HH7 (Smith et al. 2003). The [Fe II] emission is mainly associated with the Mach disk, with only weak emission coming from the bow cap. Although [Fe II] emission is associated with jets rather than bows (Lorenzetti et al. 2002), [Fe II] can be detected from bow caps (Davis et al. 1999), consistent with predictions from fast (> 60 km s^{-1}), dissociative J-type shocks (Hollenbach & Mckee 1989a). The detection of optical [S II] lines are predicted to remain strong for J-type shocks with lower shock speeds, thus implying weaker shocks. Smith et al. (2003) concludes from the distribution of the [Fe II] emission that the jet is terminated by a Mach disk with slightly higher shock speed than the average shock speed across the apex.

5.4.4 Summary

Modelling of 1720 MHz OH maser emitting SNRs shows tight constraints on the temperature, density and OH column density of the regions surrounding the masers. The production of these masers also requires that the shock be of C-type. These constraints are discussed in detail in § 3.2. Observations of the regions surrounding the masers in these SNRs show that the current model

predictions are in good agreement with observational results as discussed in § 4.1. C-type shocks are strong sources of emission in the $1-0$ $S(1)$ line of H_2 at 2.12 μm and many observations show the 1720 MHz OH masers in SNRs overlying the peak emission of H_2 at 2.12 μm (see § 4.4.3).

NIR observations have revealed shock excited H_2 at 2.12 μm toward many HH objects. Models indicate that the interface formed by the interaction between the HH objects and the ISM in many cases results in the formation of a J-type shock at the apex, but on the wings of the shock conditions exists that show signatures of C-type shocks. Bow shocks predictions of the NIR emission show that the strongest shock is experienced at the apex of the bow and is responsible for the NIR [Fe II] emission produced by fast dissociative J-type shocks. The shock weakens as one moves away from the apex to the broader wings where C-type shocks are responsible for the NIR emission of H_2 (see § 5.4.1).

The detection of H_2 emission and the indication of C-type shocks in HH objects are however not convincing evidence that 1720 MHz OH masers can be produced behind the shock fronts of HH objects as in SNRs. Unfortunately, detailed magneto-hydrodynamic modelling of bow shocks has only been done for a few HH objects. Even though these models can make predictions of the physical properties of these shocks, the parameter space in which these shocks can occur is extensive, and there are insufficient observations at present to constrain the parameter space. The velocity and excitation temperature both decrease as one moves away from the apex of a bow shock into the wings, so a wide range of conditions is possible along the shock.

HH 7 is the best and most extensive studied HH object. § 5.4.3 discusses the modelling of HH 7 bow shock, and give the properties of the physical

conditions of the shock region. The magnetic field ($B = 0.97 \times 10^{-4}$ G), pre-shock density (8×10^3 cm^{-3}), shock velocity ($v_s = 55$ km s^{-1}) and also the fact that the model requires C-type shocks on the wings of the bow shock are in agreement with the constraints required by the SNR model for the production of 1720 MHz OH masers. It should be noted that the value of v_s is the velocity at the apex and will decrease as one moves away from the apex along the bow wings.

If 1720 MHz OH masers can be found behind the C-type shocks of these HH objects they would provide one of the best methods to constrain the physical parameters of these shock regions. The next chapter describes the observing procedure and the results of the initial survey to search for 1720 MHz OH masers toward HH objects, using single dish radio telescopes.

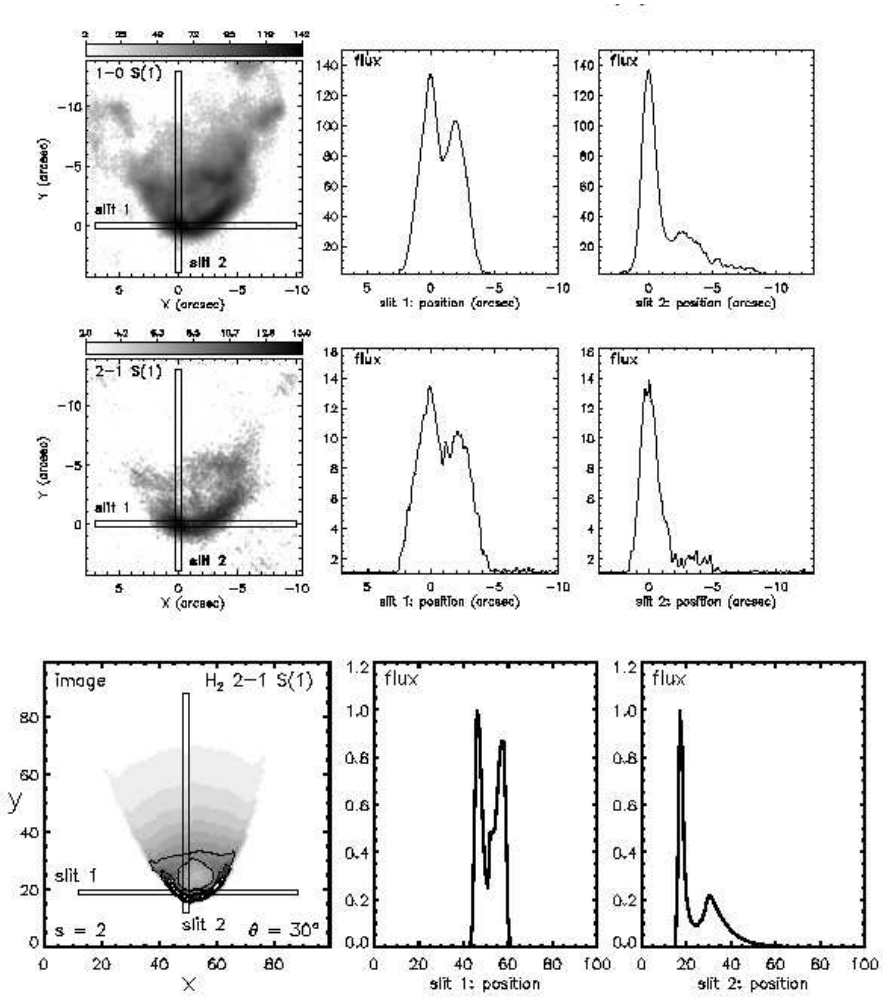

Figure 5.8: Top panel: (*left panel*): The H_2 $2-1$ $S(1)$ emission taken with the IRCAM 3. The grey scale bar indicates the calibrated flux level in 10^{-19} W m^{-2} arcsec^{-2}. (*middel panel*): The declination flux cross-cut in the H_2 $2-1$ $S(1)$ line fluxes, measured along slits of width 0.54 arcseconds. (*right panel*): The same cross-cut for the right ascension slits.
Bottom panel: The $2-1$ $S(1)$ image and intensity profiles for the standard HH7 CBOW model (From: Smith et al. (2003))

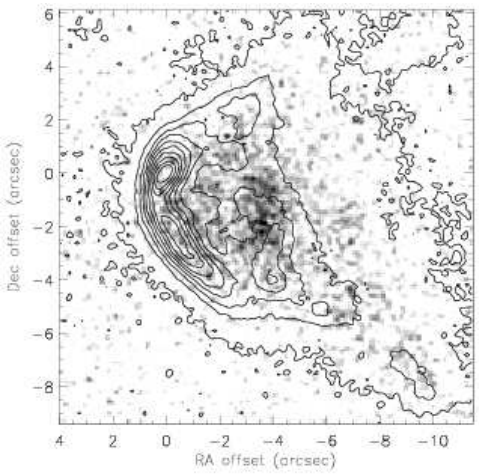

Figure 5.9: HH7 in the [Fe II] line (grey scale) overlaid with H_2 $1-0$ $S(1)$ line contours (From: Smith et al. (2003))

Chapter 6

OH Observations Towards HH Objects

Both models and observations have shown that 1720 MHz OH masers are collisionally excited behind the shock fronts of a number of SNRs. It has been suggested that these masers can become important indicators of the location of SNR-molecular cloud interactions, and they could be a powerful probe of C-type shocks. Because of the narrow range of conditions required to produce these masers, their presence can reveal many of the physical properties of the surrounding gas. HH outflows and their associated molecular outflows also interact with the surrounding medium producing shock-excited emission nebula. Observations and models of HH objects indicate the presence of C-type shocks, and physical and spectroscopic properties of these regions often show remarkable similarity to those observed in maser emitting SNRs. These similarities initiated a survey for 1720 MHz OH masers toward a selected number of HH objects using single dish radio telescopes. The source selection

criteria, the observing procedures, data analysis and preliminary results of these observations are described in this chapter.

6.1 HH Candidates

454 HH objects are currently catalogued in Reipurth's "A General Catalogue of Herbig Haro Objects 2nd Edition" (Reipurth 1999b). We selected a sample of HH objects from Reipurth's catalogue to search for 1720 MHz OH emission. Although many more HH objects have been discovered since the publication of Reipurth's catalogue in 1999, the objects in the catalogue are those objects that were discovered first, mainly because they are the strongest and thus easiest to pick up, and therefore they should be the largest, closest and brightest HH objects. The distribution of the HH objects from Reipurth's catalogue are shown in right ascension (RA) and declination (DEC) in Figure 6.1. Shock-excited masers are not as intense as those in H II regions, and therefore a survey with high sensitivity is required. Not only are the largest single dish telescopes located in the northern hemisphere, but most arrays of radio telescopes are north of the equator. Hence, if follow up observations need to be done, the sources must be able to be seen with these arrays such as the Very Large Array (VLA) and Multi-Element Radio-Linked Interferometer (MERLIN). Also, only a small number of HH objects have been discovered in the southern hemisphere (see Figure 6.1), probably because of fewer observations to search for HH objects towards the southern skies. Based on the SNR statistics, only 10% of SNRs searched showed 1720 MHz OH masers. If the same statistics apply to HH objects, a large number of sources need to be surveyed to find at least a few detections of maser

emission.

We have restricted our initial survey to those HH objects located in the northern hemisphere. The nearest HH objects in Reipurth's catalogue were considered as primary targets but some more distant objects were also included to fill in the observations. Most objects are within a distance of 900 pc; HH290 and HH291 are at a distance of 1500 pc, HH281, HH282, HH283 and HH284 are at 1800 pc, and HH163 is at a distance of 2200 pc. Candidate objects (shown in color in Figure 6.1) were selected at random from this sample of HH objects. However, some sources have been included because a case has been made in the literature that C-type shocks are present (HH2, HH7, HH211, HH240, HH241). We have also included those sources for which extensive observations have been done which includes the following: HH1/2, HH7–11, HH24, HH34, HH119, HH150, HH154, HH155, HH158, HH167, HH168, HH240, HH294 and HH303.

6.2 Observations

Existing surveys (Haynes & Caswell 1977; Turner 1979) show spatially extended 1720 MHz OH emission, and Turner (1982) has shown that this emission is an excellent tracer of the spiral arm structure of the Galaxy. These surveys were made at relatively low resolution so it is not clear whether they indicate stimulated emission from a maser process, or whether they show the distribution of an extended thermal component of the ISM with a slightly elevated temperature. This unrelated extended emission will confuse identifications in our search for compact maser emission towards HH objects. For this reason our survey is composed of two parts. First, we identify line emis-

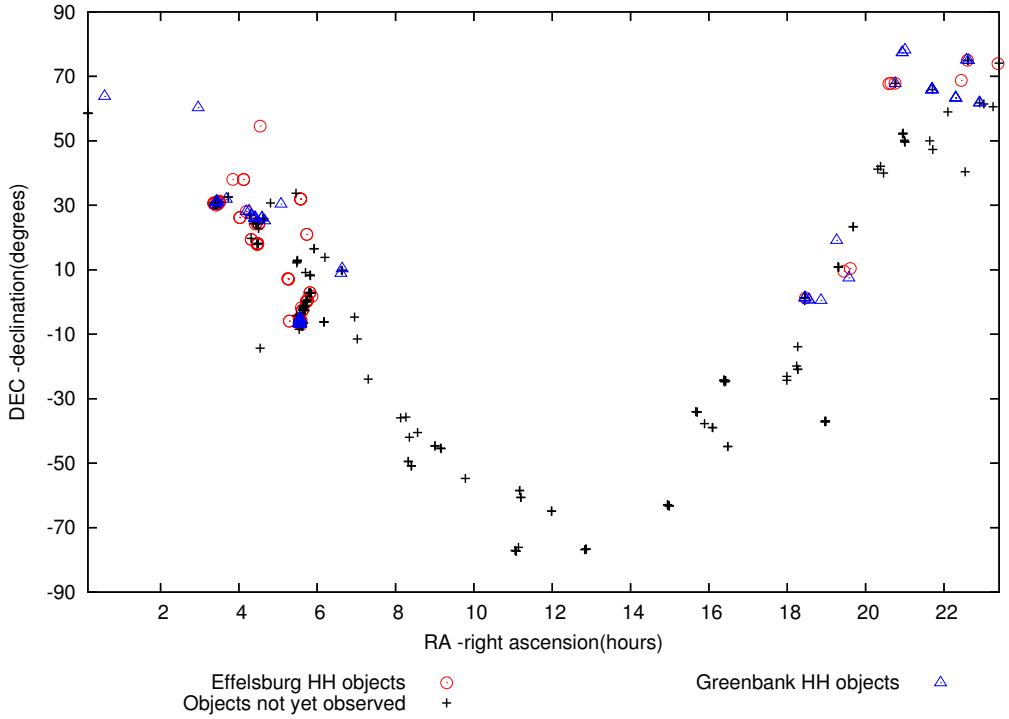

Figure 6.1: HH objects from Reipurth's catalogue plotted as functions of their RA and DEC.

sion towards HH objects doing single dish observations. The most efficient way to search a large number of sources for a particular astrophysical feature is to make the first observations with a single-dish telescope of moderate resolution and high sensitivity. The flexibility and speed with which many sources can be measured has allowed us to cover the majority of our sources in a relatively short period. In the second part of our survey those sources with positive detections from our single dish observations will be re-observed with interferometers to confirm the presence of maser emission. Interferometers like the VLA are not sensitive to spatially extended emission, only the compact (maser) emission. This procedure was used and established with great success in the surveys for 1720 MHz OH masers towards SNRs as discussed

in § 3.1.

Some of our sources have been observed in both the 1720 MHz and 1665/1667 MHz OH transition. If the 1720 MHz OH line is detected in emission, together with the 1667 MHz line in absorption, this would be a clear indication of a non-thermal process taking place, suggesting maser emission. Extended, weak 1720 MHz OH line emission with narrow line widths have been discovered towards SNRs and are believed to be produced by weak amplification in the OH behind a face-on shock as opposed to the edge-on geometry required by maser spots (Yusef-Zadeh et al. 2003). Follow-up observations with large interferometers will be required to distinguish between this non-thermal extended 1720 MHz OH emission and the presence of maser spots.

6.2.1 The Greenbank 100m Survey

Observing time was applied for at the Greenbank telescope (GBT) to search for 1720 MHz OH emission towards HH objects. Time for the observations was granted to Smits and de Witt and has been listed under code # GBT05A-021. The observations were made with the NRAO[1] 100m telescope in Green Bank, West Virginia on 4 February and 7 February 2005. The OH main line at 1667.35903 MHz and the OH satellite line at 1720.52998 MHz were observed using the 1.15 – 1.73 GHz L-band receiver in both hands of circular polarization and using frequency switching. A configuration with a total bandwidth of 12.5 MHz in the 9 level mode, and 16384 spectral channels was used, centered on 0 km s^{-1}, with respect to the local standard of rest (LSR). The total velocity coverage was $\pm$1090 km s^{-1} and the velocity resolution per

[1]The National Radio Astronomy Observatory is a facility of the National Science Foundation operated under cooperative agreement by Associated Universities, Inc.

channel was 0.13 km s^{-1}. The beam width of the telescope is 7.2′, and often more than one HH object fell within the beam. A total of 50 observations (see Figure 6.1) were made using an integration time of 15 minutes per pointing. The GBT data have not yet been analyzed, but the data will be reduced using the dish tool for Single Dish Radio Astronomy in the AIPS++ package.

Table 6.1: The name, position in J2000.0 coordinates, region and distance of the HH objects searched using the Greenbank telescope. The objects are listed in order of increasing RA.

Object	**RA (J2000)** dd mm ss.s	**Dec (J2000)** dd mm ss.s	**Region**	**Distance** pc
HH288	00 37 13.56	+64 04 15.1	Cassiopeia	2000
HH163	03 01 32.70	+60 29 12.0	IC 1848A	2200
HH279	03 27 18.64	+30 17 15.7	Perseus	300
HH14	03 28 49.60	+31 01 15.5	NGC 1333	220
HH12	03 28 57.71	+31 20 10.1	NGC 1333	220
HH15	03 28 58.86	+31 08 02.0	NGC 1333	220
HH7	03 29 08.03	+31 15 28.5	NGC 1333	220
HH5	03 29 20.30	+31 12 51.8	NGC 1333	220
HH18	03 29 26.40	+31 07 38.4	NGC 1333	220
HH211	03 43 56.29	+32 00 54.3	IC 348	300
HH156	04 08 51.52	+28 20 28.2	CoKu Tau-1	140
HH220	04 14 16.89	+28 10 59.2	CW Tau jet	140
HH157	04 22 00.88	+26 57 37.7	Haro 6-5B jet	140
HH159	04 27 02.03	+26 05 41.6	DG Tau B jet	140

Continued on next page

continued from previous page

Object	RA (J2000) dd mm ss.s	Dec (J2000) dd mm ss.s	Region	Distance pc
HH31	04 28 18.37	+26 17 40.5	B218	140
HH230	04 38 28.57	+26 10 50.3	DO Tau jet	140
HH231	04 42 37.64	+25 15 38.3	DP Tau jet	140
HH229	05 07 49.51	+30 24 07.0	RW Aur jet	140
HH83	05 33 31.55	−06 29 38.2	L1641	470
HH84	05 34 11.37	−06 34 00.1	L1641	470
HH209	05 35 13.87	−05 21 46.6	M42	470
HH33	05 35 17.88	−06 17 41.9	L1641	470
HH34	05 35 29.90	−06 27 00.8	L1641	470
HH86/HH327	05 36 00.0	−06 36 00.0	L1641	470
HH41/HH128	05 36 05.23	−05 03 44.2	L1641	470
HH3/HH35	05 36 17.10	−06 42 27.7	L1641	470
HH144	05 36 21.22	−06 46 07.5	L1641	470
HH39	06 39 05.82	+08 51 26.7	R Mon	800
HH124	06 41 02.66	+10 15 05.4	NGC 2264	800
HH106	18 29 18.71	+01 14 17.3	Serpens	310
HH107	18 29 47.99	+01 25 55.5	Serpens	310
HH108	18 35 36.12	−00 35 09.5	Serpens	310
HH172	18 54 05.84	+00 32 41.0	Aquila	500
HH223	19 17 57.41	+19 11 52.9	L723	300
HH119	19 36 51.47	+07 34 10.2	B335	250
HH215	20 45 53.81	+67 57 39.0	L1158	500
HH200	20 55 09.24	+77 31 20.2	L1228	300
HH198	20 59 09.72	+78 22 48.0	Cepheus	300

Continued on next page

continued from previous page				
Object	**RA (J2000)** dd mm ss.s	**Dec (J2000)** dd mm ss.s	**Region**	**Distance** pc
HH232	21 42 26.81	+66 04 27.7	NGC 7129	1000
HH238	21 42 40.25	+66 05 41.2	NGC 7129	1000
HH167	21 43 06.61	+66 06 54.3	NGC 7129	1000
HH234	21 43 29.70	+66 08 38.3	NGC 7129	1000
HH252	22 19 37.77	+63 32 38.2	S 140	900
HH149	22 35 24.24	+75 17 05.9	L 1251	300
HH189	22 38 39.92	+75 10 41.0	L 1251	300
HH168	22 56 03.54	+62 02 01.3	Cep A	700
HH174	22 56 58.53	+62 01 42.4	Cep A	700

6.2.2 The Effelsberg 100m Survey

Observing time was applied for at the Effelsberg telescope to search for 1720 MHz OH emission towards HH objects. Time for the observations was granted to Smits and de Witt and has been listed under code # 96-04. The observations were made with the Effelsberg 100m telescope in Effelsberg, Bonn from 28 February to 2 March, and also on 5 and 20 May, 2005. The OH satellite line at 1720.52998 MHz was observed using the 1.3 – 1.7 GHz receiver in both hands of circular polarization and using frequency switching. A configuration with a total bandwidth of 1.56 MHz and 1024 spectral channels was used, and the spectra were centered on $v = 0.0$ km s^{-1} with respect to the LSR. The total velocity resolution per channel was ± 0.53 km s^{-1} and the total velocity coverage was ± 136 km s^{-1}, which gives a velocity coverage of ± 84 km s^{-1} after folding the spectra. The beam width of the

telescope was 7′, resulting in many of the observations having more than one object per pointing. All the data were reduced using CLASS (Continuum and Line Analysis Suite of Software) which is part of the GILDASS package. Integration times varied from 10 to 15 minutes per pointing, yielding typical rms noise levels in the final spectra of 70 mJy. A total of 62 sources were observed (see Table 6.2.2), which included one of the detections made at Greenbank (HH220).

Table 6.2: The name, position in J2000.0 coordinates, region and distance of the HH objects searched using the Effelsberg telescope. The objects are listed in order of increasing RA.

Object	**RA (J2000)** dd mm ss.s	**Dec (J2000)** dd mm ss.s	**Region**	**Distance** pc
HH268	03 24 22.05	+30 48 10.7	L1448	300
HH193	03 24 52.74	+30 54 55.0	L1448	300
HH194	03 24 58.60	+30 47 41.6	L1448	300
HH197	03 25 36.82	+30 45 02.5	L1448	300
HH279	03 27 18.64	+30 17 15.7	Perseus	300
HH318	03 27 44.62	+30 14 17.2	L1445	300
HH16	03 29 08.20	+31 09 10.5	NGC1333	220
HH17	03 29 20.32	+31 18 34.8	NGC1333	220
HH372	03 30 45.95	+30 29 25.8	Barn 1	220
HH429	03 31 48.11	+31 09 59.3	Barn 1	220
HH430	03 32 27.79	+31 24 39.0	Barn 1	220
HH356	03 33 06.00	+31 26 43.8	Barn 1	220

Continued on next page

continued from previous page

Object	RA (J2000) dd mm ss.s	Dec (J2000) dd mm ss.s	Region	Distance pc
HH431	03 33 15.04	+31 09 08.2	Barn 1	220
HH433	03 33 49.52	+31 04 57.2	Barn 1	220
HH366	03 46 59.10	+32 45 20.3	B5	350
HH462	03 54 05.01	+38 10 35.5	Perseus	350
HH362	04 04 23.00	+26 20 41.3	L1489	140
HH464	04 10 42.43	+38 07 38.5	L1473	350
HH410	04 28 11.8	+24 18 13	Tau	140
HH414	04 29 30.30	+24 39 53.7	Tau	140
HH412/13	04 29 50.4	+24 37 41	Tau	140
HH411	04 30 16.90	+24 42 42.5	Tau	140
HH257	04 31 00.72	+18 00 42.3	L1551	140
HH466	04 33 35.41	+24 21 32.1	B 18	140
HH378	04 36 40.86	+54 38 11.6	Cam	???
HH386	04 51 47.34	+30 47 14.6	Aur	140
HH328	05 17 55.46	+07 15 55.8	L1589	470
HH329	05 18 40.52	+07 08 17.5	L1589	470
HH240/1	05 19 49.5	−05 52 03.3	Ori	470
HH295	05 34 36.92	−05 04 16.9	OMC-3	470
HH407	05 35 17.24	−05 59 38.8	L1641	470
HH294	05 35 23.1	−05 03 58.	OMC-3	470
HH203/4	05 35 22.4	−05 25 06.2	M42	470
HH173	05 35 34.78	−06 33 01.1	L1641	470
HH330	05 35 42.01	−05 04 42.6	L1641	470
HH316	05 35 54.73	−06 04 53.5	L1641	470

Continued on next page

continued from previous page

Object	RA (J2000) dd mm ss.s	Dec (J2000) dd mm ss.s	Region	Distance pc
HH308	05 36 01.12	−06 00 25.0	L1641	470
HH309	05 36 03.13	−05 49 47.1	L1641	470
HH306	05 36 08.05	−06 08 46.5	L1641	470
HH296	05 36 11.59	−06 17 22.8	L1641	470
HH1	05 36 20.34	−06 45 08.4	L1641	470
HH298	05 36 21.70	−06 21 51.5	L1641	470
HH146	05 36 22.58	−06 48 21.6	L1641	470
HH2	05 36 25.50	−06 47 15.8	L1641	470
HH302	05 36 48.32	−06 20 38.4	L1641	470
HH402	05 37 17.54	−07 00 39.6	L1641	470
HH405	05 37 24.74	−05 43 36.0	L1641	470
HH406	05 37 38.83	−05 39 22.1	L1641	470
HH283	05 37 50.03	+31 59 54.9	AFGL5157	1800
HH289	05 38 10.19	−01 44 14.2	Ori I-2	470
HH43	05 38 10.76	−07 09 23.4	L1641	470
HH449	05 38 42.79	−07 12 43.8	L1641	470
HH469	05 39 19.02	−07 26 27.4	L1641	470
HH470D	05 39 24.7	−07 28 28	L1641	470
HH444	05 39 39.78	−02 31 21.7	σOri	470
HH447	05 40 08.84	−02 33 32.8	σOri	470
HH247	05 41 31.95	−02 17 25.8	NGC2023	470
HH24	05 46 09.62	−00 09 55.9	NGC2068	470
HH22/23	05 46 13.	−00 05 30	NGC2068	470
HH291	05 47 02.21	+20 59 51.2	CB 34	1500

Continued on next page

continued from previous page

Object	RA (J2000) dd mm ss.s	Dec (J2000) dd mm ss.s	Region	Distance pc
HH471/2/3/4	05 47 35	+00 38 47	L1630	470
HH476	18 28 59.48	+00 29 12.9	Ser	310
HH106	18 29 18.71	+01 14 17.3	Ser	310
HH460	18 29 38.63	+01 18 23.8	Ser	310
HH107	18 29 47.99	+01 25 55.5	Ser	310
HH458	18 29 58.02	+01 13 43.2	Ser	310
HH455	18 30 22.77	+01 16 19.0	Ser	310
HH108	18 35 36.12	−00 35 09.5	Ser	310
HH250	19 21 13.62	+10 52 31.0	Aql	300
HH387	19 38 57.31	+10 30 16.7	Aql	300
HH376	20 36 02.27	+67 54 28.1	L1152	500
HH375	20 39 10.17	+68 01 19.7	L1157	440
HH315	20 45 33.96	+68 03 24.9	Cep	500
HH198	20 59 09.72	+78 22 48.0	Cep	300
HH380	20 59 11.49	+52 34 14.8	Cyg	???
HH389	21 01 09.17	+50 21 45.8	Cyg	???
HH421	21 01 55.06	+49 51 37.1	Cyg	550
HH363	22 28 00.62	+69 01 00.4	L1221	200
HH149	22 35 24.24	+75 17 05.9	L1251	300
HH373	22 36 59.95	+75 15 16.4	L1251	300
HH374	22 37 39.11	+75 07 31.4	L1251	300
HH358	23 24 38.97	+74 12 35.7	L1262	180

The number of individual HH objects observed exceeds the total number of actual observations due to the fact that often more than one HH object fell within the beam. The coordinates for each observation as listed in Tables 6.1 and 6.2.2 corresponds to the coordinates of the HH object on which the telescope beam was centered. In those cases where more than one HH object is listed, the coordinates given correspond to the central position between those HH objects. If the reader wishes to obtain all the HH objects that fell within the beam during a particular observation, they are referred to the Astronomy software package "Cartes Du Ciel" (Chevalley 2001) which can be downloaded from the Internet. An external catalogue for HH objects can be downloaded from the interned (Reipurth 1999a) and needs to be copied into the software package (/cat/externes) and activated. When the "eyepiece" is activated and set to $7'$ it can be centered on any HH object and all the HH objects within the beam will be shown.

6.3 Results and Discussion

Spectra from the Effelsberg telescope have been fitted with polynomial baselines which have been subtracted and then the spectra were folded. Where lines are present in the spectra, Gaussian profiles have been fitted in a least squares sense and the Gaussians subtracted from the data. The fitted Gaussians left no significant residuals above the noise. Calibration of the Effelsberg data is not yet completed so the spectra are still in units of system temperature (T_A). These observations led to the detection of 10 sources of emission, 11 sources of absorption, and 5 sources with P-Cygni profiles. This left 34 non-detections in the 1720 MHz OH transition. The parameters of

the Gaussian profiles fitted to the data are listed in Table 6.3

Table 6.3: The name and line profile of the HH objects observed with the Effelsberg telescope together with the position, width and intensity parameters of the Gaussian profiles fitted to the Effelsberg data. The numbers in brackets are the errors in the fits.

Object	**Line Profile**[a]	**Position** v_0 (km s^{-1})	**Width** Δv (km s^{-1})	**Intensity** Amplitude (T_A)
HH184	E	17.06 (0.14)	1.7 (0.3)	0.079
HH220	E	7.08 (0.05)	0.94 (0.10)	0.14
HH247	E	28.17 (0.13)	1.9 (0.3)	0.082
HH250	E	-10.20 (0.07)	1.23 (0.15)	0.11
HH380	E	-18.74 (0.10)	2.84 (0.23)	0.103
HH389	E	-16.8 (0.3)	3.4 (0.8)	0.052
HH412/13	E	16.9 (0.16)	1.3 (0.3)	0.052
HH414	E	17.29 (0.14)	1.25 (0.3)	0.073
HH421/424	E	-17.28 (0.19)	3.8 (0.7)	0.069
HH431/432	E	13.58 (0.12)	1.32 (0.25)	0.097
HH296/7/9/3	P	29.3 (0.0)	1.9 (0.3)	0.057
		26.5 (0.0)	2.57 (0.23)	-0.12
HH298	P	29.23 (0.10)	1.3 (0.3)	0.096
		26.32 (0.13)	2.6 (0.3)	-0.103
HH407	P	28.9 (0.3)	2.0 (0.6)	0.073
		25.78 (0.20)	3.2 (0.5)	-0.146

Continued on next page

[a]E = emission; A = absorption; P = P-Cygni profile

continued from previous page				
Object	**Line Profile**	**Position**	**Width**	**Intensity**
		v_0 (km s−1	δv (km s^{-1})	Amplitude ($_A$)
HH469/470	P	26.34 (0.19)	1.7 (0.5)	0.074
		23.69 (0.13)	2.9 (0.3)	-0.176
HH476	P	-6.85 (0.14)	1.7 (0.4)	-0.071
		-11.12 (0.23)	3.8 (0.5)	0.067
HH38/43	A	24.20 (0.05)	1.69 (0.14)	-0.209
HH301/302	A	26.45 (0.10)	2.74 (0.20)	-0.158
HH306	A	26.35 (0.14)	2.7 (0.3)	-0.097
HH308	A	26.71 (0.10)	2.14 (0.23)	-0.118
HH316	A	25.74 (0.09)	2.88 (0.20)	-0.129
HH330	A	28.78 (0.5)	5.0 (1.0)	-0.042
HH402	A	24.66 (0.10)	1.27 (0.23)	-0.103
HH406	A	23.70 (0.17)	1.7 (0.5)	-0.072
HH449	A	24.11 (0.09)	2.60 (0.20)	-0.137
HH458	A	-8.19 (0.25)	2.5 (0.5)	-0.054
HH460/477	A	-7.37 (0.17)	2.9 (0.3)	-0.07

The spectrum of HH220 has the narrowest of the emission lines and is currently the best candidate for possible maser emission (see Figure 6.3). Observations toward HH220 were also made with the Greenbank telescope in the 1720 MHz OH transition as well as in the 1665 and 1667 MHz OH transitions. If there is absorption at 1667 MHz for this source, then it will be a strong candidate for maser emission. Further confirmation of possible maser emission will come from future follow-up observations with arrays. Observations toward HH389 show the 1720 MHz OH transition in emission. The

spectrum has a broad line which looks like it could be made of more than one line (see Figure 6.3). The residuals indicate that one Gaussian is sufficient to fit the data, but this could be a signal to noise (S/N) problem. More data would be needed to check up on this. Figure 6.3 shows the absorption spectrum of the 1720 MHz OH line observed towards HH38 and Figure 6.3 shows the P-Cygni profile of the spectra observed towards HH298.

Most of the emission lines have line widths of ≤ 2 km s_1 (see Table 6.3) and these line widths are consistent with those measured for the 1720 MHz OH masers detected in SNRs (see § 3.1). The line widths of the emission profiles lie between $\sim 1 - 3$ km s^{-1}, which fall within the line widths measured for the extended, weak 1720 MHz OH line emission detected toward some of the maser emitting SNRs (see § 4.1). The maser model developed for SNRs (see § 3.3.2) requires that the masers lie be in that part of the shock that is perpendicular to the line of sight to achieve maximum gain, and hence have velocities close to the systemic velocity. Similar conditions should apply to masers that form in HH objects, and therefore the most likely candidates to find maser spots in are those with jets projected in the plane of the sky, and these masers would have velocities close to the systemic velocity of the region. However, it is believed that the extended, weak OH line emission are low gain masers or weak amplification in the OH behind a face-on shock and that the detection of these extended features are, even without the presence of the compact features are also indicative of an interaction. The sources with positive detections will be re-observed using arrays to confirm possible maser emission. Where possible the velocity of these masers will be compared to other measurements of the systemic velocity from the literature to determine whether they are physically related to the observed HH objects or not.

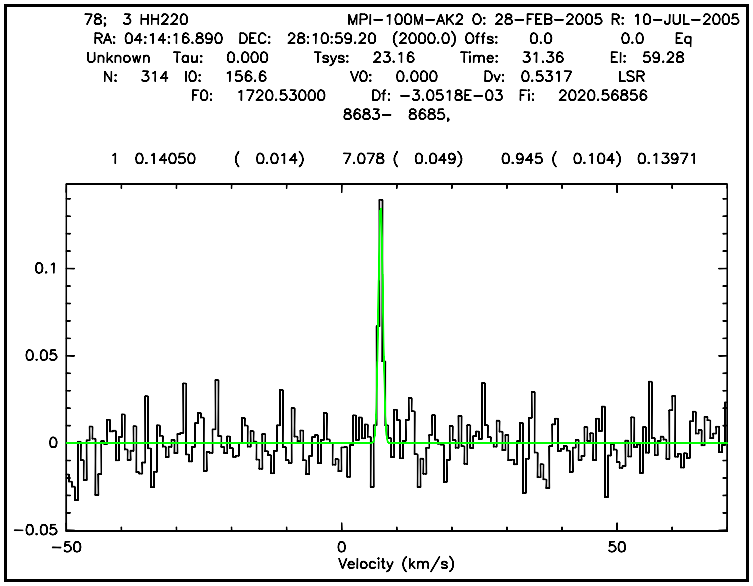

Figure 6.2: 1720 MHz OH emission spectrum of HH220

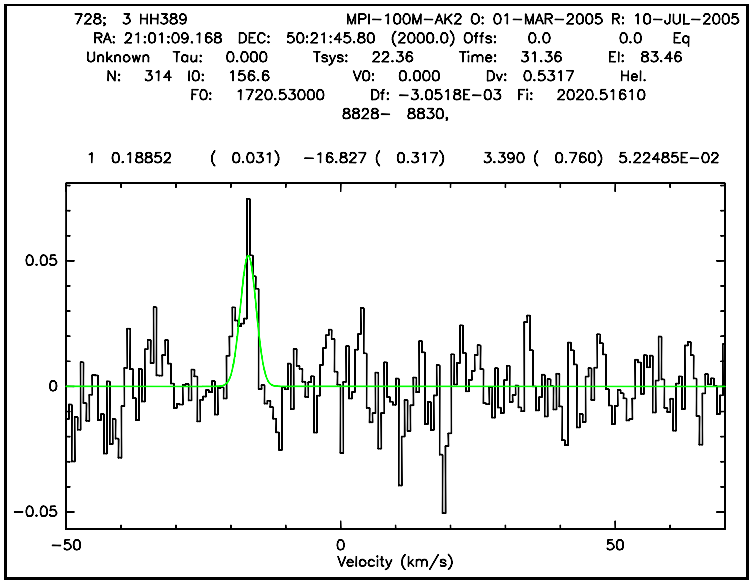

Figure 6.3: 1720 MHz OH emission spectrum of HH389

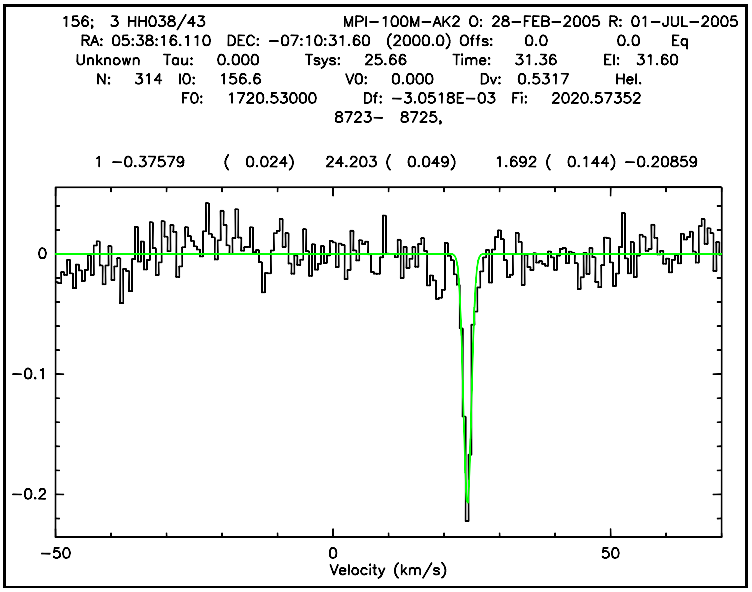

Figure 6.4: 1720 MHz OH absorption spectrum of HH38

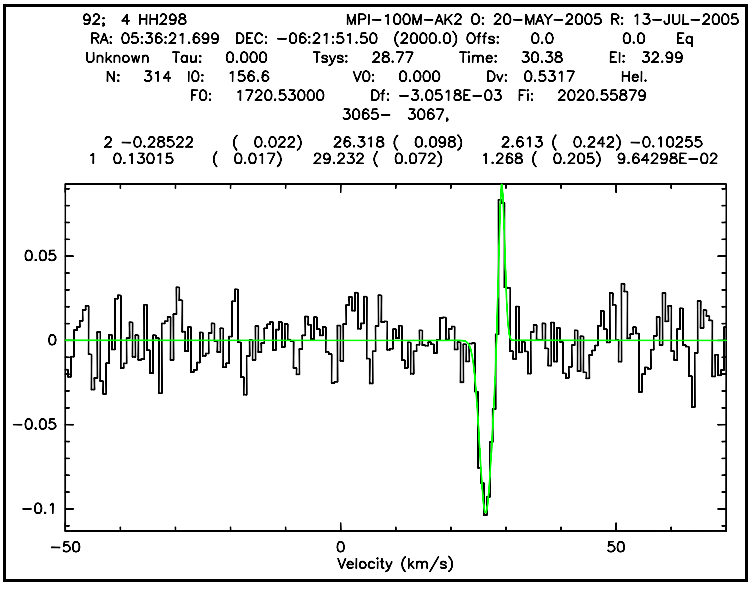

Figure 6.5: 1720 MHz OH P-Cygni profile of HH298

Chapter 7

Conclusions and Future Prospects

7.0.1 Conclusions

Star birth is associated with the ejection of collimated, high velocity jets of gas that flows into the surrounding ISM. When a massive star comes to the end of its life it erupts in a violent explosion called a supernova in which hot gas expands into the ISM. Both the outflow from a protostar and the blast wave from a supernova explosion sweeps up interstellar material as it moves through space and forms a shock front at the interface between itself and the ISM. Molecular cloud material is disturbed by these shocks and the excitation of the gas results in detectable emission. Shock excited 1720 MHz OH masers have been detected in SNRs and are produced under very tight constraints of the physical conditions, specifically the presence of a C-type shock. The aim of this study was to determine whether the conditions behind

the shocks of HH objects can be suitable to produce 1720 MHz OH masers. A literature study was done on both SNRs and HH objects in order to gain familiarity with both fields of research and to enable the comparison of the physical and spectroscopic properties of these shock regions. Observations were also carried out to search for 1720 MHz OH emission toward a selected number of HH objects. The main conclusions of the literature survey and the observational work are discussed below.

Conclusions of the Literature Study

The discovery of characteristics, observational data and modelling for both maser emitting SNRs and HH objects was obtained from the literature. Even though the origin and characteristics of SNRs and HH outflows are quite different, they both interact with the ISM and produce shock regions that often show very similar properties.

- 1720 MHz OH masers can only form behind C-type shocks and it has been shown for many HH objects that C-type shocks are present.
- Many of the maser emitting SNRs can only be explained by the presence of both J- and C-type shocks and modelling of some HH objects show a bow shaped structure with a J-type shock at the apex and C-type shocks in the wings.
- Similar spectra are observed for both SNRs and HH objects. The dissociative J-type shocks are traced by atomic lines of [Fe II] and [S II] for example, while molecular C-type shocks are traced by NIR lines of H_2 and the millimeter-wavelength transitions of CO.
- Radio continuum emission traces the shell of the shock front in SNRs, and radio continuum emission is detected towards some

HH objects. Both SNRs and HH objects show X-ray emission.

- Both SNRs and HH objects have been observed to interact with dense molecular clouds, which is a requirement for the production of 1720 MHz OH masers.
- Magnetic fields play an important role in the shock physics of both the SNRs and HH objects. The magnetic field strength found for HH7 is in the range of magnetic field strengths found for maser emitting SNRs.
- The maser model developed for SNRs requires that the velocity vector of the shock be perpendicular to the line of sight, as detectable masers would only be in that part of the shock that is perpendicular to the line of sight. In general, 1720 MHz OH masers in SNRs are observed on the edge of the shock front tangent to our line-of-sight, but there are a few exceptions. Similar conditions should apply to masers that form in HH objects, and therefore the most likely candidates to find maser spots in are those with jets projected in the plane of the sky.
- The shocks in HH objects have a wide range of physical conditions, and hence it is possible that some of these objects could support shock-excited 1720 MHz OH masers.

Conclusions of Observations

A number of HH objects were observed using single dish radio telescopes as an initial search for 1720 MHz OH masers towards HH objects.

- Data obtained from observations with the GBT have not yet been analyzed.

- Data reduction of the Effelsberg telescope observations show emission lines in 10 out of the 62 observations made.
- The sources with positive detections show line widths comparable to those observed in SNRs
- HH220 is the best candidate for possible maser emission as it shows the narrowest emission line.
- 11 sources showing absorption and 5 sources showing P-Cygni profiles were detected with the Effelsberg telescope.

7.0.2 Future Prospects

The main goal of this work was to determine whether conditions can exist in HH objects to support the production of 1720 MHz OH masers, and to search a selected sample of HH objects for possible 1720 MHz OH emission. Future work include the following:

- Complete the analysis of all observations
- If any sources are found to have 1720 MHz OH emission lines and 1667 absorption lines, they would be strong candidates for maser emission and follow-up observations with arrays.
- Based on the SNR statistics, only 10% of SNRs searched showed 1720 MHz OH masers. If the same statistics apply to HH objects, a large number of sources need to be surveyed to find at least a few detections of maser emission. Very few southern hemisphere HH objects have been looked at and in future the Parkes single dish radio telescope in Australia could be used for

an initial survey to search for 1720 MHz OH emission towards southern hemisphere HH objects. When the Karoo Array Telescope (KAT) comes online follow-up observations of the southern hemisphere sources could continue.

- Observations of those HH objects showing emission, absorption and P-Cygni profiles will be obtained for southern hemisphere HH objects with the Fabry Perot Spectroscope of the South African Large Telescope (SALT) to study these HH objects in the optical and NIR.
- The Atacama Large Millimeter Array (ALMA) will allow millimeter-wave observations of southern hemisphere HH objects which will give molecular observations of density and temperature.
- Future studies and modelling will be concerned with understanding why OH is detected in some HH objects and not in others, where the OH is located in relation to the shocks and what the chemistry is by which the OH forms.

References

Aharonian F. A., 2004, NATURE, 432, 75

Allen D. A., Burton M. G., 1993, Nature, 363, 54

Ambartsumian V. A., 1954, Comm. Byurakan Obs. No. 13

André P., Martin-Pintado J., Despois D., Montmerle T., 1990, A&A, 236, 180

Anglada G., 1996, in , ASO Conf. Ser. 93, Radio Emission from the Stars and the Sun. San Francisco: ASP, p. 3

Anglada G., Rodríguez L. F., Cantó J., Estalella R., Torrelles J. M., 1992, ApJ, 395, 494

Arce H. G., Goodmann A. A., 2002, ApJ, 575, 928

Arce H. G., Hector G., 2002, PhD thesis, Harvard University

Arikawa Y., Tatematsu K., Sekimoto Y., Takahashi T., 1999, PASJ, 51, L7

Arthur S. J., Falle S. A. E. G., 1991, MNRAS, 251, 93

Axon D. J., Taylor K., 1984, MNRAS, 207, 241

Bachiller R., 1996, ARA&A, 34, 111

Bachiller R., Cernicharo J., 1991, A&A, 239, 276

Bachiller R., Martin-Pintado J., Fuente A., 1991, A&A, 243, L21

Bachiller R., Martin-Pintado J., Tafalla M., Cernicharo J., Lazareff B., 1990, A&A, 231, 174

Bally J., Devine D., 1994, ApJ, 428, L65

Bally J., Devine D., Alten V., 1996, ApJ, 473, 921

Bally J., Devine D., Alten V., Sutheland R. S., 1997, ApJ, 478, 603

Bally J., Devine D., Reipurt B., 1996, ApJ., 473, L49

Bally J., Lada C. J., 1983, ApJ, 265, 824

Bally J., O'Dell C. R., McCaughrean M. J., 2000, AJ, 119, 2919

Bally J., Reipurt B., 2001, ApJ, 546, 299

Bally J., Reipurt B., 2002, RevMexAA (Serie de Conferencias), 13, 1

Banas K. R., Hughes J. P., Bronfman L., Nyman L. A., 1997, ApJ, 480, 607

Beckwith S., Gatley I., Matthews K., Neugebauer G., 1978, ApJ, 223, L41

Bell A. R., 1978a, MNRAS, 182, 147

Bell A. R., 1978b, MNRAS, 182, 443

Bence S. J., Richer J. S., Padman R., 1996, MNRAS, 279, 866

Binette L., Dopita M. A., Tuohy I. R., 1985, ApJ, 297, 476

Blondin J. M., Königl A., Fryxell B. A., 1989, ApJ, 337, L37

Böhm K. H., 1978, A&A, 64, 115

Böhm K. H., 1983, Rev. Mex. Astron. Astrofis., 7, 55

Böhm K. H., Böhm-Vitense E., Brugel E. W., 1981, ApJ, 245, L113

Böhm K. H., Brugel E. W., Mannery E., 1980, ApJ, 235, L137

Böhm K. H., Brugel E. W., Olmsted E., 1983, A&A, 125, 23

Böhm K. H., Bührke T., Raga A. C., Brugel E. W., Witt A. N., Mundt R., 1987, ApJ, 316, 349

Böhm K. H., Schwartz R. D., Siegmund W. A., 1974, ApJ, 193, 353

Braun R., Strom R. G., 1986a, A&AS, 63, 345

Braun R., Strom R. G., 1986b, A&A, 164, 193

Brogan C. L., Frail D. A., Goss W. M., Troland T. H., 2000, ApJ, 537, 875

Brogan C. L., Goss W. M., Lazendic J. S., Green A. J., 2004, AJ, 128, 700

Brugel E. W., Böhm K. H., Mannery E., 1981a, ApJS, 47, 117

Brugel E. W., Böhm K. H., Mannery E., 1981b, ApJS, 243, 874

Bührke T., Mundt R., Ray T. P., 1988, A&A, 200, 99

Burnham S. W., 1890, MNRAS, 51, 94

Burnham S. W., 1894, Pub. Lick Obs., 2, 175

Burton M. G., Geballe T. R., Brand P. W. J. L., Webster A. S., 1988, MNRAS, 231, 617

Burton M. G., Hollenbach D. J., Haas M. R., Erickson E. F., 1990, ApJ, 355, 197

Cantó J., 1980, A&A, 86, 327

Cantó J., Raga A. C., 1991, ApJ, 372, 646

Cantó J., Raga A. C., 1998, MNRAS, 297, 383

Caswell J. L., Murray J. D., Roger R. S., Cole D. J., Cooke D. J., 1975, A&A, 45, 239

Cernicharo J., Reipurth B., 1996, ApJ, 460, L57

Cesarsky D., Cox P., Pineau des Forts G., van Dishoeck E. F., Boulanger F., Wright C. M., 1999, A&A, 348, 945

Chernin L. M., Masson C. R., 1995, ApJ, 443, 181

Chevalier R. A., 1982, ApJ, 258, 790

Chevalier R. A., 1999, ApJ, 511, 798

Chevalley P., 2001, Software Package: Cartes Du Ciel, http://www.stargazing.net/atropc/download.html

Choe S. U., Böhm K. H., Solf J., 1985, ApJ, 288, 338

Claussen M. J., Frail D. A., Goss W. M., Gaume R. A., 1997, ApJ, 489, 143

Claussen M. J., Goss W. M., Frail D. A., Desai K., 1999, ApJ, 522, 349

Claussen M. J., Goss W. M., Frail D. A., Seta M., 1999, ApJ, 117, 1387

Claussen M. J., Marvel K. B., Wootten A. Wilking B. A., 1998, ApJ, 507, L79

Cohen M., 1990, ApJ, 354, 701

Cohen M., Schwartz R. D., 1987, ApJ, 316, 311

Cohen R., Dame T. M., Garay G., Montani J., Rubio M., Thaddeus P., 1988, ApJ, 331, l95

Corbel S., Chapuis C., Dame T., Durouchoux P., 1999, ApJ, 526, L29

Cowsik R., Sarkar S., 1984, MNRAS, 207, 745

Cox D. P., Shelton R. L., Maciejewski W., Smith R., Plewa T., A. P., Rzyczka M., 1999, ApJ, 524, 179

Curiel S., Cantó J., Rodríguez L. F., 1987, RMxAA, 14, 595

Davis C. J., Smith M., 1996, A&A, 309, 929

Davis C. J., Smith M., Eislöffel J., Davies J. K., 1999, MNRAS, 308, 539

de Gouveia dal Pino E. M., Benz W., 1993, ApJ, 410, 686

Deng L., Yang J., Zheng Z., Jiang Z., 2001, Publications of the Astronomical Society of the Pacific, 113, 463

DeNoyer L. K., 1979a, ApJ, 232, L165

DeNoyer L. K., 1979b, ApJ, 228, L41

DeNoyer L. K., 1983, ApJ, 264, 141

Dickel J. R., van Breugel W. J. M., Strom R. G., 1991, AJ, 101, 2151

Dickman R. L., Snell R. L., Ziurys L. M.and Huang Y. L., 1992, ApJ, 400, 203

Dopita M. A., 1978, ApJS, 37, 117

Dopita M. A., Binette L., Schwartz R. D., 1982, ApJ, 261, 183

Dopita M. A., Schwartz R. D., Evans I., 1982, ApJ, 263, L73

Draine B. T., 1980, ApJ, 241, 1021

Draine B. T., Roberge W. G., 1982, ApJ, 259, L91

Draine B. T., Roberge W. G., Dalgarno A., 1983, ApJ, 264, 485

Dubner G. M., Moffett D. A., Goss W. M., Winkler P. F., 1993, AJ, 105, 2251

Edwards S., Hartigan P., Ghandour L., Andrulis C., 1994, AJ, 108, 1056

Eislöffel J., 1997, in , IAU Symp. 182, Herbig-Haro Flows and the Birth of Low Mass Stars. Dordrecht: Kluwer, p. 93

Eislöffel J., Mundt R., 1992, A&A, 263, 292

Eislöffel J., Mundt R., 1994, A&A, 284, 530

Eislöffel J., Mundt R., Böhm K. H., 1994, AJ, 108, 1042

Eislöffel J., Smith M. D., Davis C., Ray T., 1996, AJ, 112, 2086

Elias J. H., 1980, ApJ, 241, 728

Elitzur M., 1976, ApJ, 203, 124

Elitzur M., de Jong T., 1978, A&A, 67, 323

Falle S. A. E. G., Innes D. E., Wilson M. J., 1987, MNRAS, 225, 741

Favato F., Fridlund C. V. M., Micela G., Sciortino S., Kaas A. A., 2002, A&A, 386, 204

Fernandes A. J. L., 2000, MNRAS, 315, 657

Frail D. A., Goss W. M., Reynoso E. M., Giacani E. B., Green A. J., Otrupcek R., 1996, AJ, 111, 1651

Frail D. A., Goss W. M., Slysh V. I., 1994, ApJ, 424, L111

Frail D. A., Kassim N. E., Cornwell T. J., Goss W. M., 1995, ApJL, 454, L129

Frail D. A., Mitchell G. F., 1998, ApJ, 508, 690

Froebrich D., Smith M. D., Eislöffel J., 2002, A&A, 385, 239

Froebrich D., Smith M. D., Eislöffel J., 2003, AP&SS, 287, 217

Gaetz T. J., 1990, ApJ, 353, 357

Gaetz T. J., Edgar R. J., Chevalier R. A., 1988, ApJ, 329, 927

Gaume R. A., Mutel R. L., 1987, ApJS, 65, 193

Ghavamian P., Hartigan P., 1998, ApJ, 501, 687

Goss W. M., 1968, ApJS, 15, 131

Goss W. M., Robinson B. J., 1968, Astrophysics Lett., 2, 81

Graham J. A., Elias J. H., 1983, ApJ, 272, 615

Gray A. D., 1994, MNRAS, 270, 835

Gredel R., 1994, A&A, 292, 580

Gredel R., Reipurth B., 1994, A&A, 289, L19

Green A. J., 2002, in , IAU Symp. 206, Cosmic MASERs: From Protostars to Blackholes. Astronomical Society of the Pacific, p. 204

Green A. J., Frail D. A., Goss W. M., Otrupcek R., 1997, AJ, 114, 2058

Green A. J., Frail D. A., Goss W. M., Yusef-Zadeh F., Roberts D. A., 1996, ASP Conf. Ser. 102, The Galactic Center, p. 93

Green D. A., 2001, A Catalogue of Galactic Supernova Remnants (2001 December version), Mullard Radio Astronomy Observatory, Cavendish Laboratory, Cambridge, UK, (available on the world wide web at http://www.mrao.cam.ac.uk/surveys/snrs/)

Gueth F., Guilloteau S., 1999, A&A, 343, 517

Gull S. F., 1973, MNRAS, 161, 47

Haas M. R., Hollenbach D. J., Erickson E. F., 1991, ApJ, 374, 555

Habing H. J., Olnon F. M., Winnberg A., Matthews H. E., Baud B., 1983, Astr. Ap., 128, 230

Haro G., 1952, ApJ, 115, 572

Haro G., 1953, ApJ, 117, 73

Harrus I. M., Hughes J. P., 1996, ApJ, 464, L161

Hartigan P., Edwards S., Ghandour L., 1995, ApJ, 452, 736

Hartigan P., Morse J., Raymond J. C., 1994, ApJ, 436, 125

Hartigan P., Morse J., Raymond J. C., 1995, ApJ., 444, 943

Hartigan P., Morse J. A., Tumlinson J., Raymond J., Heathcote S., 1999, ApJ., 512, 901

Hartigan P., Raymond J., Hartmann L., 1987, ApJ., 316, 323

Hartigan P., Raymond J., Meaburn J., 1990, ApJ., 362, 624

Hartigan P., Reipurth B., Morse J., Heathcote S., Bally J., 2000, AAS., 197, 1007

Hartmann L., Kenyon S. J., 1985, ApJ, 299, 462

Hartmann L., Raymond J., 1984, ApJ, 276, 560

Hartmann L., Raymond J., Meaburn J., 1990, ApJ, 362, 624

Hartquist T. W., Menten K. M., Lepp S., Dalgarno A., 1995, MNRAS, 272, 184

Hartquist T. W., Stenberg A., 1991, MNRAS, 248, 48

Haynes R., Caswell J., 1977, MNRAS, 178, 219

Heathcote S., Reipurth B., 1992, AJ, 104, 2193

Henney W. J., 1996, RMxAA, 32, 3

Herbig G. H., 1950, ApJ, 111, 11

Herbig G. H., 1951, ApJ, 113, 697

Herbig G. H., 1957, in Herbig G. H., ed., , IAU Symp. 3. Cambridge Univ. Press

Herbig G. H., 1958, in O'Connell D. J. K., ed., , Stellar Populations. Vatican Observatory

Herbig G. H., 1968, IAU Coll., Non-Periodic Phenomena in Variable Stars, eds. L. Detre, and Reidel

Herbig G. H., 1973, Inf. Bull. Var. Stars. 832

Herbig G. H., 1977, ApJ, 217, 693

Hirth G. A., Mundt R., Solf J., 1994, ApJ., 427, L99

Ho P. T. P., Ho L. C., Szczepaniski J. C., Jackson J. M., Armstrong J. T., Barrett A. H., 1991, Nature, 350, 309

Hoffman I. M., Goss W. M., Brogan C. L., Claussen M. J., 2005, ApJ, 257, 273

Hoffman I. M., Goss W. M., Brogan C. L., Claussen M. J., Richards A. M. S., 2003, ApJ, 583, 272

Hollenbach D., 1997, in Reipurt B., Bertout C., eds, , IAU Symp. 182, Herbig Haro Flows and the Birth of Low Mass Stars. Dordrecht:Kluwer, p. 181

Hollenbach D., Mckee C. F., 1989a, ApJ, 342, 306

Hollenbach D. J., Mckee C. F., 1989b, ApJ, 342, 306

Humphreys E. M. L., 1999, PhD thesis, University of Bristol.

Hwang U., Hughes J. P., Petre R., 1998, ApJ, 497, 833

Indebetouw R., Noriega-Crespo A., 1995, AJ, 109, 752

Innes D. E., Giddings J. R., Falle S. A. G. E., 1987a, MNRAS, 224, 179

Innes D. E., Giddings J. R., Falle S. A. G. E., 1987b, MNRAS, 226, 67

Innes D. E., Giddings J. R., Falle S. A. G. E., 1987c, MNRAS, 227, 1021

Jun B., Norman M. L., 1996, ApJ, 472, 245

Kassim N. E., Baum S. A., Weiler K. W., 1991, ApJ, 374, 212

Kaufman M. J., Neufeld D. A., 1996, ApJ, 456, 611

Keohane J. W., Rudnick L., Anderson M. C., 1996, ApJ, 466, 309

Khanzadyan T., Smith M. D., Davis C. J., Stanke T., 2004, A&A, 418, 163

Klein R. I., Mckee C. F., Colella P., 1994, ApJ, 420, 213

Köngl A., 1982, ApJ, 261, 115

Koo B. C., 1989, ApJ, 337, 318

Koo B. C., Moon D. S., 1997a, ApJ, 475, 194

Koo B. C., Moon D. S., 1997b, ApJ, 485, 263

Koralesky B., Frail D. A., Goss W. M., Claussen M. J., Green A. J., 1998, AJ, 116, 1323

Kwan J., 1977, ApJ, 216, 713

Lada C. J., 1985, ARA&A, 23, 267

Lasenby J., Yusef-Zadeh F., Lasenby A. N., 1989, in Morris M., ed., , IAU Symp. 136, The Center of the Galaxy. Dordrecht: Kluwer, p. 365

Lazendic J. S., Wardle M., Burton M. G., Yusef-Zadeh F., Green A. J., Whiteoak J. B., 2004, MNRAS, 354, 393

Lazendic J. S., Wardle M., Burton M. G., Yusef-Zadeh F., Whiteoak J. B., Green A. J., Ashley M. C. B., 2002, MNRAS, 331, 537

Lazio T. J. W., Cordes J. M., 1998a, ApJS, 115, 225

Lazio T. J. W., Cordes J. M., 1998b, ApJ, 497, 238

Lee C. F., Stone J. M., Ostriker E. C., Mundy L. G., 2001, ApJ, 557, 429

Lizano S., Giovanardi C., 1995, ApJ, 447, 742

Lizano S., Heiles C., Rodríguez L. F., Koo B. C., Shu F. H., Hasegawa T., Hayashi S., Mirabel I. F., 1988, ApJ, 67, 283

Lockett P., Gauthier E., Elitzur M., 1999, ApJ, 511, 235

Lorenzetti D., Giannini T., Vitali F., Massi F., Nisini B., 2002, ApJ, 564, 839

Loushin R. S., 1989, PhD thesis, Univ. Illinois

McCaugrean M. J., Rayner J. T., Zinnecker H., 1994, ApJ, 436, L189

McCoey C., Giannini T., Flower D. R., Caratti o Garatti A.and Ogura K., Walsh J., 2004, MNRAS, 353, 813

Maciejewski W., Murphy E. M., Lockman F. J., Savage B. D., 1996, ApJ, 469, 238

Martí J., Rodríguez L. F., Reipurth B., 1995, ApJ, 449, 184

Masheder M. R. W., Field D., Gray M. D., Migenes V., Cohen R. J., Booth R. S., 1994, A&A, 281, 871

Masson C. R., Chernin L. M., 1993, ApJ, 414, 230

Matzner C. D., Mckee C. F., 1999, ApJ, 526, L109

Meaburn J., Dyson J. E., 1987, MNRAS, 225, 863

Mezger P. G., Duschl W. J., Zylka R., 1996, A&ARJ, 7, 289

Mezger P. G., Zylka R., Salter C. J., Wink J. E., Chini R., Kreysa E., Tuffs R., 1989, A&A, 209, 337

Micono M., Massaglia S., Bodo G., Rossi P., Ferrari A., 1998, A&A, 333, 1001

Milne D. K., 1990, in , IAU Symp. 140, Galactic and Intergalactic Magnetic Fields. Dordrecht: Kluwer, p. 67

Mizuno N., Yamaguchi R., Mizuno A., Rubio M., Abe R., Saito H., Onishi T., Yonekura Y., Yamaguchi N., Ogawa H., Fukui Y., 2001, PASJ, 53, 971

Molinari S., Liseau R., Lorenzetti D., 1993, A&AS, 101, 59

Morse J., Heathcote S., Hartigan P., Cecil G., 1993, AJ, 106, 1139

Morse J. A., Hartigan P., Heathcote S., Raymond J. C., Cecil G., 1994, ApJ, 425, 738

Mundt R., Brugel E. W., Bührke T., 1987, ApJ, 319, 275

Mundt R., Fried J. W., 1983, ApJ, 274, L83

Mundt R., Ray T. P., Bührke T., Raga A. C., Solf J., 1990, A&A, 232, 37

Noriega-Crespo A., Böhm K. H., Raga A. C., 1989, AJ, 98, 1388

Noriega-Crespo A., Böhm K. H., Raga A. C., 1990, AJ, 99, 1918

Norman C., Silk J., 1979, ApJ, 228, 197

O'Connell B., Smith M. D., Davis C. J.and Hodapp K. W., Khanzadyan T., Ray T., 2004, A&A, 419, 9750

O'Connell B., Smith M. D., Froebrich D., Davis C. J.and Eislffel J., 2005, A&A, 431, 2230

O'Connell B. F., 2005, PhD thesis, Trinity College, Dublin

Offer A. R., van Hemert M. C., van Dishoeck E. F., 1994, J. Chem. Phys., 100, 362

Ogura K., 1995, ApJ, 450, L23

Ogura K., Walsh J., 1992, ApJ, 400, 248

Ortolani S., D'Odorico S., 1980, A&A, 83, L8

Pastchenko M. I., Slysh V. I., 1974, A&A, 35, 153

Pavlakis K. G., Kylafis N. D., 1996, ApJ, 467, 300

Poetzel R., Mundt R., Ray T. P., 1992, A&A, 262, 229

Pravdo S. H., Rodríguez L. F., Curiel S., Cantó J., Torrelles J. M., 1985, ApJ, 293, L35

Predehl P., Schmitt J. H. M., 1995, A&A, 293, 889

Radford H. E., 1961, Phys. Rev, 122, 114

Radhakrishnan V., Goss W. M., Murray J. D., Brooks J. W., 1972, ApJS, 24, 49

Raga A. C., 1986, AJ, 92, 637

Raga A. C., 1995, RMxAASC, 1, 103

Raga A. C., 2005, in Murdin P., ed., , Encyclopedia of Astronomy and Astrophysics. Institute of Physics Publishing

Raga A. C., Beck T., Riera A., 2004, Astrophysics and Space Science, 293, 27

Raga A. C., Binette L., 1991, RMxAA, 22, 265

Raga A. C., Böhm K. H., 1985, ApJS, 58, 201

Raga A. C., Böhm K. H., 1986, ApJ, 308, 829

Raga A. C., Böhm K. H., 1987, ApJ, 323, 193

Raga A. C., Böhm K. H., Cantó J., 1996, RMxAA, 32, 161

Raga A. C., Böhm K. H., Solf J., 1986, AJ, 92, 119

Raga A. C., Cabrit S., 1993, A&A, 278, 267

Raga A. C., Cantó J., Binette L., Calvet N., 1990, ApJ, 364, 601

Raga A. C., Mellema G., Lundqvist P., 1997, ApJS, 109, 517

Raga A. C., Mundt R., Ray T. P., 1991, A&A, 252, 733

Raga A. C., Noriega-Crespo A., 1998, AJ, 116, 2943

Ray T. P., Mundt R., Dyson J. E., Falle S. A. E. G., Raga A. C., 1996, ApJ, 468, L103

Raymond J. C., 1979, ApJS, 39, 1

Reach W. T.and Rho J., Jarrett T. H., Lagage P., 2002, ApJ, 564, 302

Reach W. T., Rho J., 1998, ApJ, 507, L93

Reach W. T., Rho J., 1999, ApJ, 511, 836

Reach W. T., Rho J., Jarrett T. H., 2005, ApJ, 618, 297

Reach W. T., Rho J. H., 1996, A&A, 315, L277

Reid M. J., Moran J. M., 1988, in , Galactic and Extragalactic Radio Astronomy. New York: Springer, p. 225

Reid M. J., Siverstein E. M., 1990, ApJ, 361, 483

Reipurth B., 1989a, Nature, 340, 42

Reipurth B., 1989b, A&A, 220, 249

Reipurth B., 1999a, A General Catalogue of Herbig Haro Objects.(available from the world wide web at http://www.stargazing.net/atropc/external.html)

Reipurth B., 1999b, A General Catalogue of Herbig Haro Objects 2. Edition, (available on the world wide web at http://www.casa.colorado.edu/hhcat)

Reipurth B., 2000, AJ, 120, 3177

Reipurth B., Aspin C., 1997, AJ., 114, 2700

Reipurth B., Bally J., 2001, ARA&A, 39, 403

Reipurth B., Bally J., Devine D., 1997, AJ, 114, 2708

Reipurth B., Bally J.and Fessen R., Devine D., 1998, Nature, 396, 343

Reipurth B., Chini R., Krügel E., Kreysa E., Sievers A., 1993, A&A, 273, 221

Reipurth B., Devine D., Bally J., 1998, AJ, 116, 1396

Reipurth B., Graham J. A., 1988, A&A, 202, 219

Reipurth B., Hartigan P., Heathcote S., Morse J., Bally J., 1997, AJ, 114, 757

Reipurth B., Raga A. C., 1999, in , The Origin of Stars and Planetary Systems. Dordrecht, Ger.:Kluwer, p. 267

Reipurth B., Raga A. C., Heathcote S., 1992, A&A, 392, 145

Reipurth B., Yu K. C., Rodrígues L., Heathcote S., Bally J., 1999, A&A, 352, L86

Reynolds S. P., 1996, ApJ, 459, L13

Reynolds S. P., Chevalier R. A., 1984, ApJ, 278, 630

Reynolds S. P., Moffett D. A., 1993, AJ, 105, 2226

Reynoso E. M., Magnum J. G., 2000, ApJ, 545, 874

Rho J., Jarrett T., Cutri R., Reach W. T., 2001, ApJ, 547, 885

Rho J., Petre R., 1998, ApJ, 503, L167

Richer J. S., Hills R. E., Padman R., 1992, MNRAS, 254, 525

Robinson B. J., Goss W. M., Manchester R. N., 1970, Australian J. Phys., 23, 363

Rodríguez L. F., 1989, RMxAA, 18, 45

Rodríguez L. F., 1997, in , IAU Symp. 182, Herbig-Haro Flows and the Birth of Low Mass Stars. Dordrecht: Kluwer, p. 83

Rodriguez L. F., Delgado-Arellano V. G., Gómez Y., Reipurth B., Torrelles J., 2000, AJ, 119, 882

Rodríguez L. F., Ho P. T. P., Torrelles J. M., Curiel S., Cantó J., 1990, ApJ, 352, 645

Rodríguez L. F., Reipurth B., 1989, RMxAA, 17, 59

Rodríguez L. F., Reipurth B., 1994, A&A, 281, 882

Rosado M., Estaban C., Leflock B., Cernicharo J., Garcia R. J., 1999, AJ, 118, 2962

Sarma A. P., Goss W. M., Green A. J., Frail D. A., 1997, ApJ, 483, 335

Schwartz R. D., 1975, ApJ, 195, 631

Schwartz R. D., 1978, ApJ, 223, 884

Schwartz R. D., 1983, ARA&A, 21, 209

Schwartz R. D., Williams P. M., Cohen M., Jennings D. G., 1988, ApJ, 334, L99

Serabyn E., Lacy J. H., Achtermann J. M., 1992, ApJ, 395, 166

Seta M., Hasegawa T., Dame T. M., Sakamoto S., Oka T., Handa T., Hayashi M., Morino J., Sorai K., Usuda K. S., 1998, ApJ, 505, 286

Seward F. D., 1985, Comments Astrophys. XI, 1, 15

Shull J. M., McKee C. F., 1979, ApJ, 227, 131

Slysh V. I., Wilson T. L., T. P., Henkel C., 1980, in Andrew B. H., ed., , IAU Symp. 87, Interstellar molecules. Dordrecht:Reidel, p. 473

Smith M. D., 1991a, MNRAS, 252, 378

Smith M. D., 1991b, MNRAS, 253, 175

Smith M. D., 1993, ApJ, 406, 520

Smith M. D., 1994, MNRAS, 266, 238

Smith M. D., Brand P. W. J. L., 1990, MNRAS, 245, 108

Smith M. D., Brand P. W. J. L., Moorhouse A., 1991, MNRAS, 248, 451

Smith M. D., Khanzadyan T., Davis C. J., 2003, MNRAS, 524, 536

Smith M. D., Suttner G., Yorke H. W., 1997, A&A, 323, 223

Solf J., 1997, in , IAU Symp. 182, Herbig Haro Flows and the Birth of Low Mass Stars. Dortrecht:Kluwer, p. 63

Solf J., Böhm K. H., Raga A. C., 1988, ApJ, 334, 229

Stahler S. W., 1994, ApJ, 422, 616

Stanke T., McCaughrean M. J., Zinnecker H., 1998, A&A, 332, 307

Stone J. M., Norman M. L., 1993, ApJ, 413, 198

Tatematsu K., Fukui Y., Iwata T., Seward F. D., Nakano M., 1990, ApJ, 351, 157

Tenorio-Tagle G., Bodenheimer P., Yorke H. W., 1985, A&A, 145, 70

Troland T. H., Heiles C., 1982, ApJ, 260, L19

Turner B., 1979, A&AS, 37, 1

Turner B. E., 1969, ApJ, 157, 103

Turner B. E., 1982, ApJ, 255, L33

Turner B. E., Chan K. W., Green S., Lubowich D. A., 1992, ApJ, 399, 114

van Dishoeck E. F., Jansen D. J., Phillips T. G., 1993, A&A, 279, 541

Wang Z., Scoville N. Z., 1992, ApJ, 386, 158

Wardle M., 1999, ApJ, 525, L101

Wardle M., Yusef-Zadeh F., Geballe T. R., 1999, in , ASP Conference Series, 186, The Central Parsecs of the Galaxy,. Astronomical Society of the Pacific, p. 432

Weaver H., Williams D., Dieter M., Lum W., 1965, Nature, 208, 29

Weinreib S., Barrett A., Meeks M., Henry J., 1963, Nature, 208, 29

White G. J., Rainey R., Hayashi S. S., Kaifu N., 1987, A&A, 173, 337

Wilking B. A., Schwartz R. D., Mundy L. D., Schultz A. S. B., 1990, AJ, 99, 344

Wootten A., 1977, ApJ, 216, 440

Wootten A., 1981, ApJ, 245, 105

Wright M. M., 2001, PhD thesis, University of Bristol.

Yan J., Wang H., Wang M., Deng L., Yang J., Chen J., 1998, AJ, 116, 2438

Yu K. C., Billawala Y., Bally J., 1999, AJ, 118, 2940

Yusef-Zadeh F., 1990, ApJ, 361, L19

Yusef-Zadeh F., Goss W. M., Roberts D. A., Robinson B., Frail D. A., 1999, ApJ, 527, 172

Yusef-Zadeh F., Roberts D. A., Goss W. M., Frail D. A., Green A. J., 1996, ApJ, 466, L25

Yusef-Zadeh F., Roberts D. A., Goss W. M., Frail D. A., Green A. J., 1999, ApJ, 512, 230

Yusef-Zadeh F., Uchida K. I., Roberts D., 1995, Science, 270, 1801

Yusef-Zadeh F., Wardle M., Rho J., Sakano M., 2003, ApJ, 585, 319

Yusef-Zadeh F., Wardle M., Roberts D. A., 2003, ApJ, 583, 267

Zhang Q., Zheng X., 1997, ApJ, 474, 719

Zhao B., Wang M., Yang J., Wang H., Deng L., Chen J., 1999, AJ, 118, 1347

Zinnecker H., McCaugrean M. J., Rayner J. T., 1998, Nature, 394, 862

Zylka R., Mezger P. G., Wink J. E., 1990, A&A, 234, 133